

Poincaré Analysis of Non-linear Electromagnetic Modes in Electron-Positron Plasmas

V. Saxena and I. Kourakis

Centre for Plasma Physics, School of Mathematics and Physics,
Queen's University Belfast BT7 1NN, Northern Ireland, UK

Email : v.saxena@qub.ac.uk

Abstract : We present an investigation of coupled nonlinear electromagnetic modes in an electron-positron plasma by using the well established technique of Poincaré surface of section plots. A variety of nonlinear solutions corresponding to interesting coupled electrostatic-electromagnetic modes sustainable in electron-positron plasmas is shown on the Poincaré section. A special class of localized solitary wave solution is identified along a separatrix curve and its importance in the context of electromagnetic wave propagation in an electron-positron plasma is discussed.

Keywords : Poincaré section, solitary, electron-positron plasma

1. Introduction

The method of Poincaré surface of section (SOS) plots has been very useful in analysing higher dimensional non-linear dynamical systems [1]. For a given n -dimensional continuous dynamical system, the corresponding Poincaré SOS plot represents an equivalent discrete dynamical system with $(n-1)$ dimensions and thus facilitates the analysis of possible periodic, quasi-periodic and chaotic modes, the original system can sustain. As non-linearity in plasmas is inherent they provide a perfect paradigm to study various non-linear processes ranging from coherent solitary waves to chaos and turbulence. In this respect, the subject of intense laser plasma interactions has ever received a great deal of attention. There has recently been a resurgence in this research area after the efficient production of very intense laser pulses ($I \geq 10^{18} \text{ W/cm}^2$) has become a reality [2]. Laser pulses with such high intensities are called relativistically intense as the associated transverse electric fields are strong enough to drive the electrons to relativistic speeds. From theoretical point of view, these high intensity laser plasma interactions provide a favourable environment for a whole range of non-linear processes. Among them the formation of electromagnetic



solitary wave is a topic of much fundamental interest particularly in theoretical plasma physics. There have been several theoretical investigations addressing the existence and stability of coupled electromagnetic solitary waves in plasmas [3].

On the other hand, the electron-positron plasmas are thought to be a constituent of various astrophysical environments e.g. in pulsar magnetospheres, in bi-polar flows in active galactic nuclei (AGN) and at the centre of our galaxy and are believed to be the first state of matter in the early stage of universe [4,5]. The coupling of electromagnetic waves to electron-positron plasmas is therefore an active area of theoretical research and has been addressed in few earlier works [5]. We present here a detailed Poincaré section based analysis of a class of possible coupled non-linear electromagnetic modes in an un-magnetized electron positron plasma with a particular emphasis on the coupled solitary waves solutions. This work is an extension of earlier works by Saxena et al. [7] and O. B. Shiryayev [6]. We adopt the same formalism as used by Kaw et al. [8] for an electron plasma with ions forming a neutralizing background.

2. Mathematical Model

The coupling of a relativistically intense electromagnetic wave with an electron-positron plasma is described by the following set of coupled fluid-Maxwell equations.

$$A_{xx} - A_{tt} = \left(\frac{n_e}{\gamma_e} + \frac{n_p}{\gamma_p} \right) A \quad (1)$$

$$\phi_{xx} = n_e - n_p \quad (2)$$

$$(p_{e,p})_t = (\phi - \gamma_{e,p})_x \quad (3)$$

$$(n_{e,p})_t + \left(\frac{n_{e,p} p_{e,p}}{\gamma_{e,p}} \right)_x = 0. \quad (4)$$

Here indices e and p stand for electron and positron species respectively, A , Φ , $n_{e/p}$, and $p_{e/p}$ respectively represent the electromagnetic vector potential, electrostatic potential, the electron/positron density and electron/positron longitudinal momentum. $\gamma_{e,p}$ Is the relativistic factor given by,

$$\gamma_{e,p} = \sqrt{1 + |A|^2 + p_{e,p}^2} \quad (5)$$

By performing a co-ordinate transformation defined as $\xi = x - \beta t$ where $\beta = v_{ph} / c$ is the normalized phase velocity, one obtains following set of coupled non-linear ordinary differential equations.

$$(\beta^2 - 1)a_{\xi\xi} + \left(\frac{\beta}{\sqrt{(\beta^2 - 1)(1 + a^2) + (1 + \phi)^2}} + \frac{\beta}{\sqrt{(\beta^2 - 1)(1 + a^2) + (1 - \phi)^2}} \right) a = 0 \quad (6)$$

and

$$\phi_{\xi\xi} + \frac{1}{(\beta^2 - 1)} \left(\frac{\beta(1 + \phi)}{\sqrt{(\beta^2 - 1)(1 + a^2) + (1 + \phi)^2}} + \frac{\beta(1 - \phi)}{\sqrt{(\beta^2 - 1)(1 + a^2) + (1 - \phi)^2}} \right) = 0 \quad (7)$$

Now making a change of variable defined by

$$(\beta^2 - 1)^{1/2} a = X$$

$$1 + \phi = -Z$$

$$\frac{\xi}{(\beta^2 - 1)^{1/2}} = \xi'$$

we get following set of simplified equations,

$$\ddot{X} + \beta \left[\frac{1}{\sqrt{\beta^2 - 1 + X^2 + Z^2}} + \frac{1}{\sqrt{\beta^2 - 1 + X^2 + (Z + 2)^2}} \right] X = 0 \quad (8)$$

$$\ddot{Z} + \beta \left[\frac{Z}{\sqrt{\beta^2 - 1 + X^2 + Z^2}} + \frac{(Z + 2)}{\sqrt{\beta^2 - 1 + X^2 + (Z + 2)^2}} \right] = 0 \quad (9)$$

Above coupled equations (8) and (9) admit following constant of motion:

$$H = \frac{1}{2} \dot{X}^2 + \frac{1}{2} \dot{Z}^2 + \beta \left[\sqrt{\beta^2 - 1 + X^2 + Z^2} + \sqrt{\beta^2 - 1 + X^2 + (Z + 2)^2} \right] \quad (10)$$

This problem is similar to that of coupled oscillators in Hamiltonian mechanics with two degrees of freedom and we solve above set of equations (8-10) using Runge-Kutta 4th order integration method to obtain coupled non-linear solutions.

3. Non-linear Solutions on Poincare Surface of Section

We consider the case of $\beta > 1$ and show the possible solutions on a Poincaré SOS plot defined by $X = 0, \dot{X} > 0$. We have investigated two interesting regimes $\beta - 1 \ll 1$ and $\beta - 1 \leq 1$. The results are shown in Fig.1 and Fig.2 respectively. It is worth noting that in the regime of phase velocities close to the speed of light, there exist a more varied class of solutions. The Poincaré plot in Fig.1 is obtained for $\beta = 1.001; H = 10$. The densely filled curves correspond to quasi periodic solutions with the ratio of the frequencies of two oscillators being a prime number. The centres of the left and right halves of the Poincaré plot represent the fixed points of zero measure and correspond to periodic orbits. The interesting island curves correspond to amplitude modulated quasi periodic modes whereas centres of these islands represent the fixed points of higher orders and correspond to periodic waves with an integer ratio of the two oscillator's frequencies. We note that the separatrix curve is not quite periodic and therefore indicates a possibility of slightly chaotic solutions.

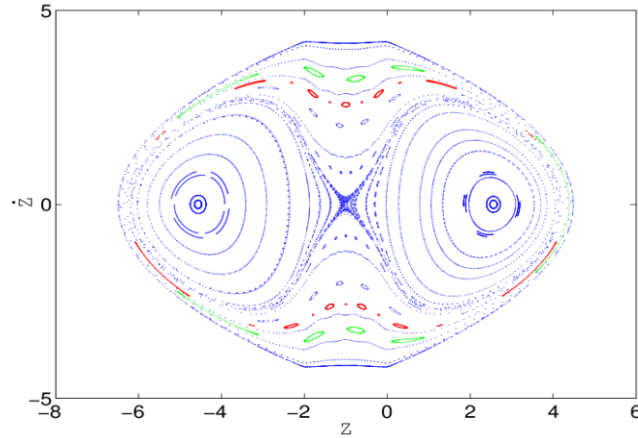
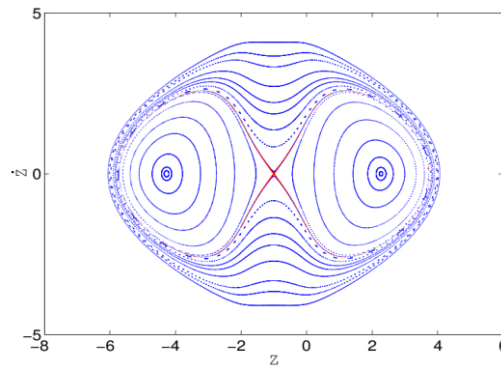


Fig.1 : Poincaré section plot for parameters $\beta=1.001, H=10$.


 Fig.2 : Poincaré section plot for parameters $\beta=1.1$, $H=10$.

Now in the regime of $\beta-1 \leq 1$, we choose the parameters to be $\beta = 1.1; H = 10$. The Poincaré surface of section plot for this case is shown in Fig.2. In this case we observe that the small island curves cease to exist. Moreover, there exists a sharp separatrix curve. This separatrix curve corresponds to localized solitary wave solutions. We show this particular solution in Fig.3.

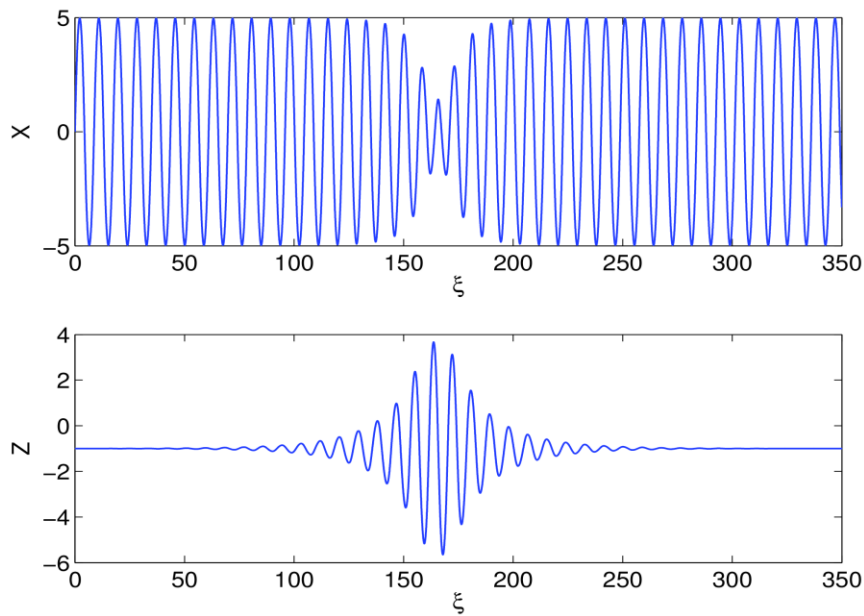


Fig.3 : Solitary solution corresponding to the separatrix curve in Fig.2.

4. Conclusions

To conclude, we have presented a class of coupled non-linear electromagnetic solutions for electromagnetic wave propagation in an electron-positron plasma by using Poincaré surface of section technique. A special class of solitary wave solutions has been identified along the separatrix curve in a parameter regime with phase velocities exceeding the speed of light by $\sim 10\%$ or more. These solitary modes play an important role in the energy localization in laser plasma interactions and therefore their stability needs to be understood which is an open area of research.

5. Acknowledgements

The authors gratefully acknowledge funding from the UK EPSRC (Engineering and Physical Science Research Council) via grant EP/I031766/1 and also (IK) via grant EP/D06337X/1. The figures are reproduced from *Europhysics Letters*, 100 15002 (2012) (doi: 10.1209/0295-5075/100/15002).

References

1. H. Poincaré 1892 *Les methods nouvelles de la mecanique celeste* (Paris: Gauthier-Villars)
2. G. Mourou and D. Umstadter, Phys. Fluids B, vol.4, 2315 (1992).
3. V. Saxena et al., Phys. Plasmas, vol. 14, 072307 (2007) *and references therein*.
4. F.C. Michel, Rev Mod. Phys., vol. 54,1 (1982).
5. M.C. Begelman et al., Rev. Mod. Phys., vol 56, 255 (1984).
6. O.B. Shiryayev, phys. Plasmas, vol 13, 112304 (2006) *and references therein*.
7. V. Saxena, A. Sen, and P. Kaw, Phys. Rev. E, vol 80, 016406 (2009).
8. P.K. Kaw, A. Sen, and E.J. Valeo, Physica D, vol 9, 96 (1983).

Rotations-Expansion-Reflections Chaotic Modelling with Singularities in Higher Dimensions

Bernd Binder

Quanics, Salem, Germany

E-mail: binder@quanics.com.

Abstract: Rotation – Expansion – Translation – Reflection chaotic models show despite of its simple generators complex structures that resemble in 2 dimensions - without referring to any material property - well known fluid/flux vortex flow patterns as recently shown by Skias. Here the model is generalized and extended to $n > 2$ dimensions with $N = n(n-1)/2$ rotational degrees of freedom and the maximum of $L = n(n-1)(n-2)/2$ singularity rotations on the sphere and hyper sphere with rotation matrix operations given by the orthogonal group $O(n)$, special orthogonal group $SO(n)$, or Lie spin group $Spin(n)$ with hierarchical relations. The radial distance to the singularities located on the rotation axes leads to the Skias power law rotation parameterized by a power exponent and rotation strength. Patterns often show characteristic flux lines emitted from a chaotic core near to a singularity. The non-commutative permutations of the non-abelian rotation group elements are relevant for encryption purposes.

Keywords: Chaotic modeling, Discrete map, Rotation-Translation, Rotation-Rotation, molecular interaction, v. Kármán Street, Dipole-dipole, Chaotic simulation, Chaotic encryption, Spin group.

1. Introduction

In quantum physics the spatial probability density and its symmetries are a basic concept to describe the evolution of observables obtained from stochastic (jump) processes in phase space. The Rotation – Expansion – Translation – Reflection pattern generation approach of Skias provides also for spatial density structures but from iterative difference equations generating more or less chaotic jumps [1, 2, 3]. The first results of Skias are very similar to v. Kármán Streets, see fig. 1, or even elliptic galaxies formations. Since a translation is a special case of a rotation with the rotation centre located at very large distances, applying subsequent rotations repeatedly around different rotation centres should also provide for interesting patterns, especially if the rotations are a function of a spatial distance with respect to one or more singularities, where rotations grow infinite due to a power law with negative exponent. We will focus in this paper onto the rotation-rotation chaotic phase jump processes on hyper-spherical loops with larger or smaller chaotic core regions, which depend on characteristic numbers and symmetries. Since the signal \mathbf{p}_i jumps in hyper



space or on hyper spheres, the resulting patterns could be relevant to physics and quantum spin groups in higher dimensions [4]. First we will introduce the rotation-translation approach in two dimensions (2-D) with one or more singularities and then replace the translation by another rotation and generalize to n dimensions on (hyper) spherical surfaces. After generating some new chaotic jump pattern by extending the Skiadas algorithm and relating it to proper physics attributes, some new input came from discussions during and shortly after the conference, especially from some authors of references [1]-[6].

2. The 3-D Expansion/Rotations/Translation Model

In 3-D Euclidian space we can map the Skiadas model onto the sphere with 2 or 3 rotations. A vector coordinate \mathbf{p}_t will describe the signal location at a time t and after one jump time interval τ at $\mathbf{p}_{t+\tau}$, where the signal starts at \mathbf{p}_0 . First we apply a expansion/reflection matrix \mathbf{E} , then apply $N=3$ different rotation in planes \mathbf{P}_i , $i=0,1,\dots,N-1$, each containing $l=0,1,\dots,m_i-1$ singularities $\mathbf{s}_{i,l}$ defining the rotation centre. At this location the axes $\mathbf{X}_{i,l}$ intersect \mathbf{P}_i orthogonally. The rotation angles $\mathcal{G}_{i,l}$ are given by the Skiadas power-law [1]

$$\mathcal{G}_{i,l} = 2\pi c_i \left(\frac{|\mathbf{v}|\tau}{|\mathbf{p}_t - \mathbf{s}_{i,l}|} \right)^2, \quad (1)$$

with distance between signal and singularity coordinates $|\mathbf{p}_t - \mathbf{s}_{i,l}|$, power exponent value usually in the range 1-3, and coupling constants c_i . We have chosen a form producing patterns linearly scaling with the jump distance $|\mathbf{v}|\tau$ while preserving shape. For one singularity per dimension $m_i=1$ the three rotations with angles \mathcal{G}_i are computed by the rotation matrices \mathbf{R}_i applied in a given permutation sequence. We take a proper coordinate system diagonalizing \mathbf{E} with pure diagonal expansion/reflection components $e_{ij}=0$ for $i \neq j$ and $|e_{xx}|=|e_{yy}|=|e_{zz}|>0$. For this case we will use the short notation $\mathbf{E}=\mathbf{E}\mathbf{D}(e_{xx},e_{yy},e_{zz})$, a negative sign shows a so-called reflection in the corresponding coordinate. These components and boundary conditions provide for the basic 3-D recurrent algorithm and difference equation as a simple extension to [1, 2, 3] generating one jump with distance $|\mathbf{v}|\tau$ after the interval τ . If we assume orthogonal rotation axes with rotation matrices \mathbf{R}_i elements of the $\text{SO}(3)$ rotation group, we have a common rotation centre located at \mathbf{r} as the intersection of the rotation axes with one singularity from every dimension ($m_i=1$) and orthogonal axes $\mathbf{X}_{0,0} \perp \mathbf{X}_{1,0} \perp \mathbf{X}_{2,0}$, where the chaotic map given by

$$\mathbf{p}_{t+\tau} = \mathbf{v}\tau + \mathbf{R}_2 \left[\mathbf{R}_1 \left[\mathbf{R}_0 \left[\mathbf{E}[\mathbf{p}_t - \mathbf{r}] \right] \right] \right] + \mathbf{r}. \quad (2)$$

To get pure rotations, the straight translation shift $|\mathbf{v}\tau|$ in eqs. (2) and (1) could be approximated by constant orbital rotations in one dimension with label j and $|\mathbf{r}_j|\mathcal{G}_j = 2\pi|\mathbf{v}\tau|$ leading to the Skiadas rotations coupling

$$\mathcal{G}_{i,l} = 2\pi c_i \left(\frac{|\mathbf{r}_j|\mathcal{G}_j}{2\pi|\mathbf{p}_t - \mathbf{s}_{i,l}|} \right)^{d_{i,l}}, \text{ in 3-D we usually take } d_j = 2, \quad (3)$$

where the coupling factor c_i can be varied in a wide range. Spin is given by an orbital rotation with label $i = j$ that has one singularity at the centre $\mathbf{s}_{j,0} = (0,0,0)$, where

$$\left(\frac{\mathcal{G}_j}{2\pi} \right)^{1-d_j} = c_j \frac{|\mathbf{r}_j|^{d_j}}{|\mathbf{p}_t|^{d_j}}, \text{ for } d_j = 1 \text{ simply } |\mathbf{p}_t| = c_j |\mathbf{r}_j|. \quad (4)$$

The iterative 3-D difference equation (2) for one start point or delta distribution $\mathbf{p}_0 = \mathbf{p}_{t=0}$ with 3 singularities and 3 orthogonal rotations is now

$$\mathbf{p}_{t+\tau} = \mathbf{R}_{\mathcal{G}_2} \left[\mathbf{R}_{\mathcal{G}_1} \left[\mathbf{R}_{\mathcal{G}_0} \left[\mathbf{E}[\mathbf{p}_t - \mathbf{r}] \right] \right] \right] + \mathbf{r}. \quad (5)$$

To obtain interesting patterns on the spherical surface we set $\mathbf{R}_{3,1} = \mathbf{R}_\theta$ as the constant longitude or orbital advance, and $\mathbf{R}_{1,2} = \mathbf{R}_\varphi$ for the altitude. Both rotations rotate around singularities given by

- $m_{3,1} = 1$, one longitude rotation $\mathbf{R}_{3,1} = \mathbf{R}_\theta$ rotating around $\mathbf{s}_{3,1,1} = (0,0,0)$ with power law exponent $d_{3,1,1} = 0$ and rotation/coupling strength $c_{3,1,1} = 2\pi j M^{-1}$,
- $m_{1,2} = 1$, one latitude rotation $\mathbf{R}_{1,2} = \mathbf{R}_\varphi$ rotating around $\mathbf{s}_{1,2,1} = (0,0,1)$ with power law exponent $d_{1,2,1} = 2$ and rotation/coupling strength $c_{1,2,1} = 2\pi k^{-2} M^{-2}$.

As an example, a two-angle rotation and signal position \mathbf{p}_t subject to rotation in 3-D spherical coordinates φ, ϕ and singularity rotations $\mathcal{G}_0 = \mathcal{G}$, $\mathcal{G}_1 = \theta$, is given by

$$\mathbf{p}_t(\varphi, \phi) = \begin{pmatrix} \sin \varphi \cos \phi \\ \cos \phi \\ \sin \varphi \sin \phi \end{pmatrix}, \mathbf{R}(\theta, \mathcal{G}) = \begin{pmatrix} \cos \mathcal{G} \cos \theta & -\sin \mathcal{G} \cos \theta & \sin \theta \\ \sin \mathcal{G} & \cos \mathcal{G} & 0 \\ -\cos \mathcal{G} \sin \theta & \sin \mathcal{G} \sin \theta & \cos \theta \end{pmatrix}.$$

With one singularity located at $\mathbf{s}_0 = (0,0,1)$ with $d = 2$ and one at the centre $\mathbf{s}_1 = (0,0,0)$ with $d = 0$ we get the two scalar rotations in spherical coordinates

$$\mathcal{G} = c \frac{\theta^2}{4\pi(1 - \sin \varphi \sin \theta)}, \quad \theta = \frac{2\pi j}{M}, \quad c = \frac{1}{j^2 k^2}. \quad (6)$$

3. Hyper-Sphere Expansion-Reflection-Rotations Map

The extension to the n -D signal map $\mathbf{p}_t \rightarrow \mathbf{p}_{t+\tau}$ with rotations embedded in n -D Euclidean space for $n \geq 3$ is straight forward. The matrix operations are based on the orthogonal group $O(n)$, or the Lie spin group $\text{Spin}(n)$ as the double cover of the special orthogonal group $\text{SO}(n)$ defining the $n \times n$ rotation matrices $\mathbf{R}_{a,b}$. The number of rotational degrees of freedom and number of orthogonal rotation planes $\mathbf{P}_{a,b}$ is

$$N(n) = \binom{n}{2} = \frac{n(n-1)}{2}, \quad N(n \geq 2) = 1, 3, 6, 10, 15, 21, 28, 36, 45, \dots \quad (7)$$

One plane can have orthogonal axes \mathbf{X}_l intersecting the plane at the singularity locations $\mathbf{s}_{a,b,l}$, l labels all orthogonal axes with $l \neq a, l \neq b$. We rotate on this plane if the rotation plane has at least one orthogonal intersection $m_{a,b} > 0$ at the singularity locations. The maximum number of singularities per dimension is $m_{a,b} = (n-2)$, if $m_{a,b} = 0$ there are no singularities and no rotations in $\mathbf{P}_{a,b}$. So the total number of possible orthogonal axis intersections for all planes and the maximum number of singularities is $L = (n-2)N = n(n-1)(n-2)/2$. There is a set of N orthogonal matrices $\mathbf{R}_{a,b}^T = \mathbf{R}_{b,a} = \mathbf{R}_{a,b}^{-1}$ with $\det \mathbf{R}_{a,b} = 1$ defining the special orthogonal group $\text{SO}(n)$ given according to [4] by

$$\mathbf{R}_{a,b}(\mathcal{G}_{a,b,l}) = \begin{bmatrix} r_{a,a} = \cos(\mathcal{G}_{a,b,l}) \\ r_{b,b} = \cos(\mathcal{G}_{a,b,l}) \\ r_{a,b} = -\sin(\mathcal{G}_{a,b,l}) \\ r_{b,a} = \sin(\mathcal{G}_{a,b,l}) \\ r_{j,j} = 1, j \neq a, j \neq b \\ r_{i,j} = 0, \text{ elsewhere} \end{bmatrix}, \quad (8)$$

with trace $n-2[1-\cos(\mathcal{G}_{a,b,l})]$ and angles $\mathcal{G}_{a,b,l}$, $l \neq a, l \neq b$. The signal is located on the hyper-spheres. The sequence of orthogonal matrices rotating a vector \mathbf{x}_t in Euclidean space must be ordered

$$\mathbf{R}_{A,B}[\mathbf{x}_t] = \mathbf{R}_{\dots} \left[\dots \left[\mathbf{R}_{a,b} \left[\dots \left[\mathbf{R}_{\dots}[\mathbf{x}_t] \right] \right] \right] \right], \quad (9)$$

covering all possible rotations or a subset as a permutation. Building the chaotic map with an n -D expansion/reflection \mathbf{E} then applying the rotation sequence $\mathbf{R}_{A,B}$ we have

$$\mathbf{p}_{t+\tau} = \mathbf{R}_{A,B} [\mathbf{E}[\mathbf{p}_t - \mathbf{r}]] + \mathbf{r}. \quad (10)$$

We are left to specify the generalized rotation angles $\mathcal{G}_{a,b,l}$, the matrix coefficients for a rotation $\mathbf{R}_{a,b}(\mathcal{G}_{a,b,l})$, the number of singularities per dimension $m_{a,b}$, and the temporal order of rotations. The angles $\mathcal{G}_{a,b,l}$ corresponding to $\mathbf{s}_{a,b,l}$ will have with strength $c_{a,b,l} \in \mathbb{R}$, metric distance $|\mathbf{p}_t - \mathbf{s}_{a,b,l}|$, and power exponent $d_{a,b,l} \geq 0$ a form given by

$$\mathcal{G}_{a,b,l} = 2\pi c_{a,b,l} \left(\frac{|\mathbf{v}\tau|}{|\mathbf{p}_t - \mathbf{s}_{a,b,l}|} \right)^{d_{a,b,l}}. \quad (11)$$

To systematically generate meaningful setup values in higher dimensions providing for interesting patterns for $n > 2$ with physical relevance, we recommend for simplicity to take a Gauss-type classical coupling field gradient power exponent

$$d_{a,b,l} = n - 1, \quad (12)$$

where the gradient power exponent is the Gauss' law field strength exponent plus 1 (for 3-D we have $d_{a,b,l} = 2$, see below). But of course, as Skiadas has shown there are several exponents that can lead to nice patterns. The power law coupling strength is scaling with the field gradient power exponent and coupling number k

$$c_{a,b,l} = k^{-d_{a,b,l}}. \quad (13)$$

The temporal order of rotations $\mathbf{R}_{a,b}$ part of the global sequence $\mathbf{R}_{A,B}$ as a permutation sequence must be given in order to setup the map and reproduce results. For the purposes of this paper we let run a in an outer loop from 0 to $n-1$, then b in the next inner loop from $a+1$ to $n-1$ covering the $N = n(n-1)/2$ orthogonal rotation planes $\mathbf{P}_{a,b}$ with orthogonal matrices $\mathbf{R}_{a,b}$, and finally l in the most inner loop from 0 to $n-1$ with $l \neq a, l \neq b$, since every plane has $n-2$ orthogonal axes intersecting at the singularities providing for the total number of singularities rotations $L = n(n-1)(n-2)/2$.

4. Results

4.a Four basic 2-D rotation-translation types with radial power -3

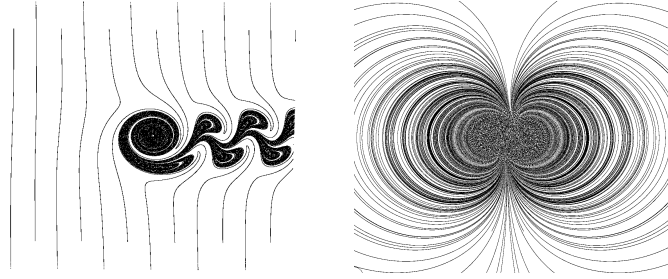


Fig. 1. Left (Skiadas [1]): $EC = (1, -1)$. Right $EC = (-1, 1)$, randomized starts.

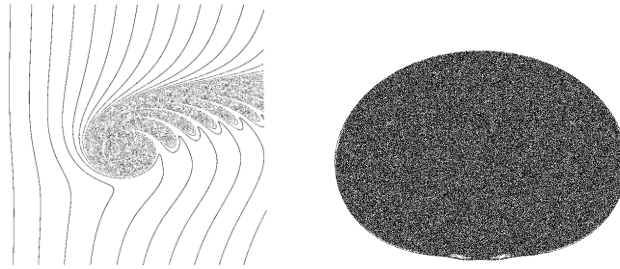


Fig. 2. Left (Skiadas [3]): $EC = (1, 1)$. Right $EC = (-1, -1)$, randomized starts.

4.b Periodic boundary (at $d_0 = 16\tau$) in 2-D at power -3

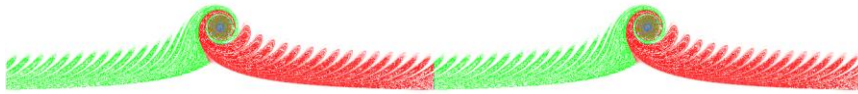


Fig. 3. $EC = (1, 1)$, if distance $x > d_0$ then $x \rightarrow x - 2 \cdot D_0$, $y \rightarrow y$, slightly random.



Fig. 4. The periodic Skiadas pattern, same parameter like fig.3 but $EC = (1, -1)$.

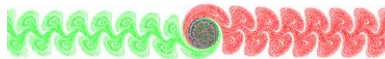


Fig. 5. Parity change for $EC = (1, -1)$: if distance $x > d_0$, then $x \rightarrow -x$ $y \rightarrow y$.

4.c Helical twist and 2-D rotation in 3-D



Fig. 6. 3-D cyclic within $d_0 = 16\tau$, power -3, with extra double-helix rotation $\psi = 5\pi x / d_0$ proportional to distance x , EC = (1, -1), randomized starts.

4.d. Multi-singularity and multi-expansion in 2-D, overlapping patterns

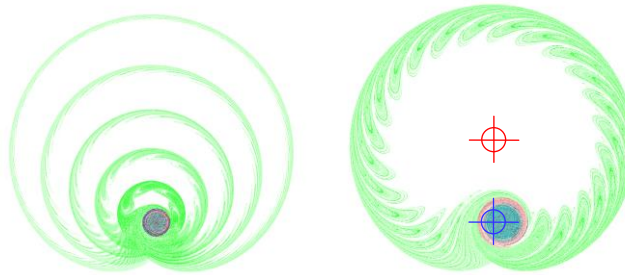


Fig. 7. Two equal singularities: positive at (0,0) and negative located at $(0, 2j)$, $j = 1, 2, 3, 4, 5$, power -3, EC = (1, 1). Right: enlarged $j = 1$ with one positive (blue) and one negative (red) singularity.

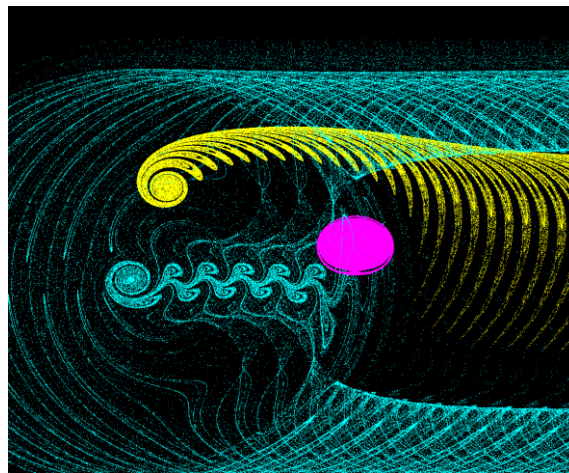


Fig. 8. Three singularities at different locations, power -3, multi expansion, 3 different EC: (1, 1) and (1, -1) and (-1, -1), randomized starts.

4.e Rotation-Rotation in 3-D, rotation centre at (0,0,0), singularity at (0,0,1)

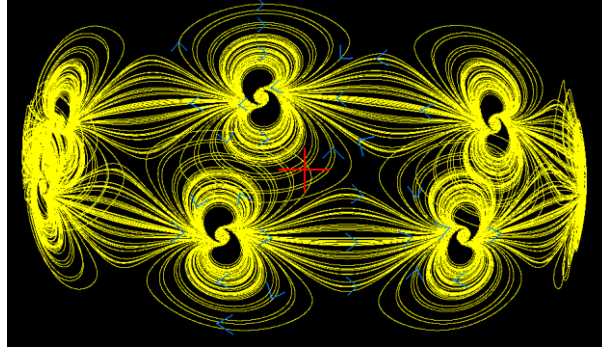


Fig. 9. Dipole ring, power -2, $M = 7$, $EC = (1, -1, 1)$, $k = 8$, slightly random. Flow directions are indicated by blue arrows.

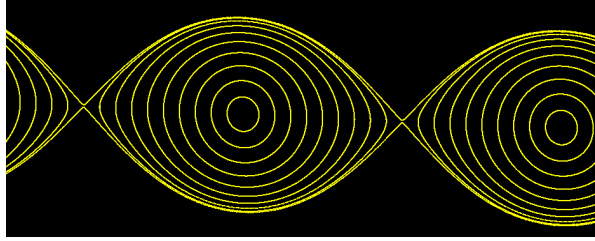


Fig. 10. Rings deformed to a wave, power -2, $M = 113$, $EC = (1, 1, 1)$, $k = 20$,
 $\vec{s}_{0,i} = (x_i, \sqrt{1-x_i^2}, 1)$, $x_i = i / M / 10$, $i = 1, 2, \dots, 10$, $j = 1$.

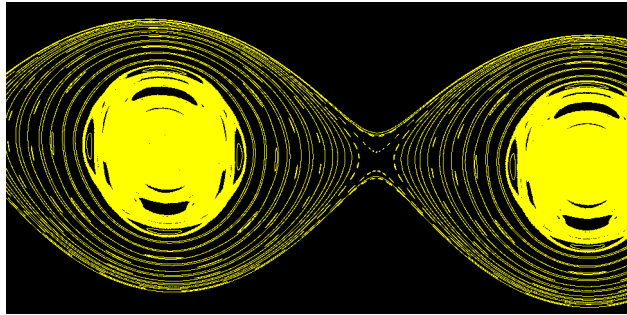


Fig. 11. Similar to fig. 10 but chaotic core with $k = 2$, power -2, $M = 13$, $EC = (1, 1, 1)$, $\vec{s}_{0,i} = (x_i, \sqrt{1-x_i^2}, 1)$, $x_i = i / M / 10$, $i = 1, 2, \dots, 10$, $j = 1$.

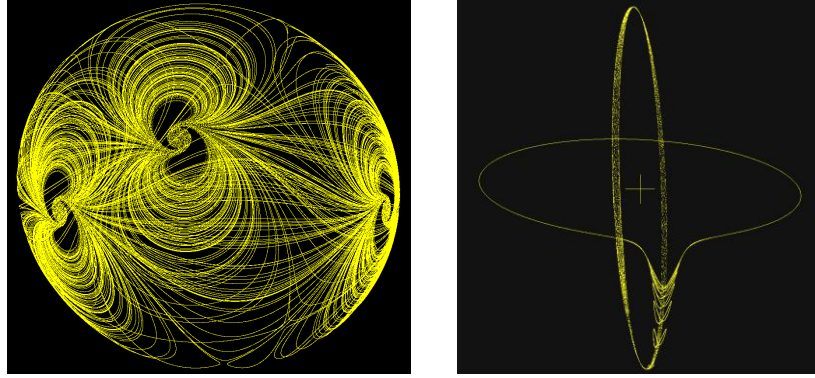


Fig. 12. Left: dipole patterns from random starts, power -2, $M = 3$, $EC = (1, -1, 1)$, $k = 4$, $j = 1$. Right: $\mathcal{O}_i(\theta_i)$ with $EC = (1, 1, 1)$, chaotic core, power -2, $M = 13$.

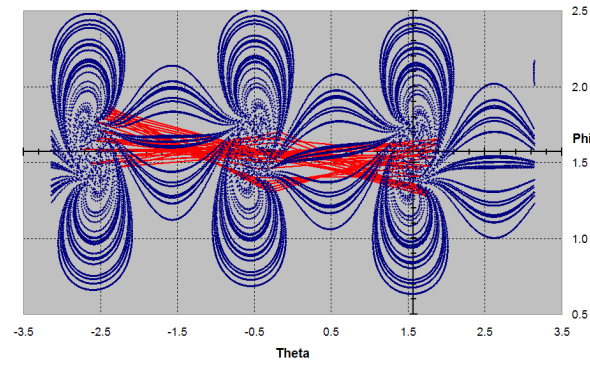


Fig. 13. Dipole pattern mapped to the rectangular phase space, power -2, $M = 3$, $EC = (1, -1, 1)$, $k = 3$, $j = 1$ after 32000 steps. Red are some jump path lines.

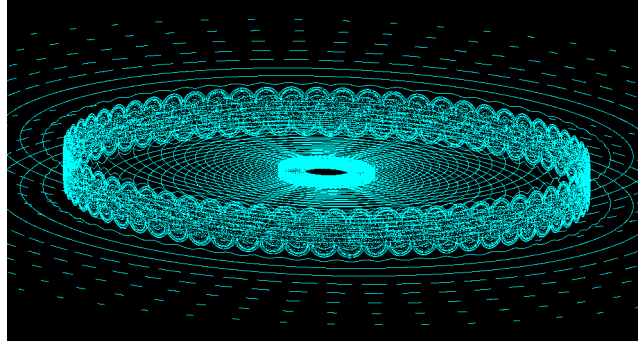


Fig. 14. $M = 128$, $k = 1$, $EC = (1, -1, 1)$, radial variation, $d = (2,0)$

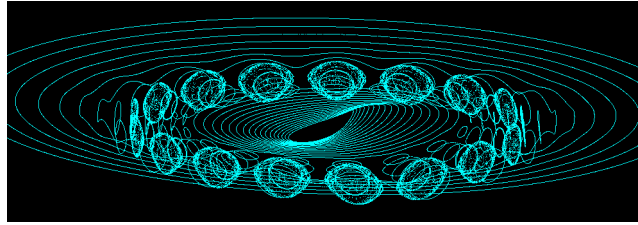


Fig. 15. $M = 20$, $k = 2.3$, $EC = (1, 1, 1)$, radial variation, $d = (2,0)$

4.f Higher-Dimensional Rotated-Rotations

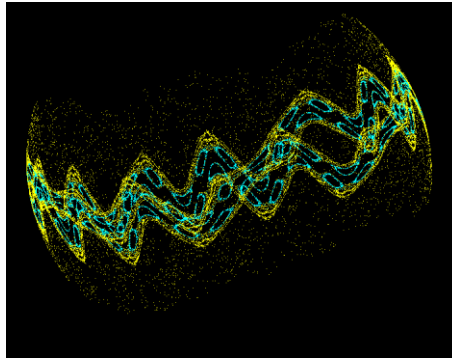


Fig. 16. $n = 3$, $k = 2$, $EC = (1, -1, 1)$, angular variation, $d = (2,2,2)$

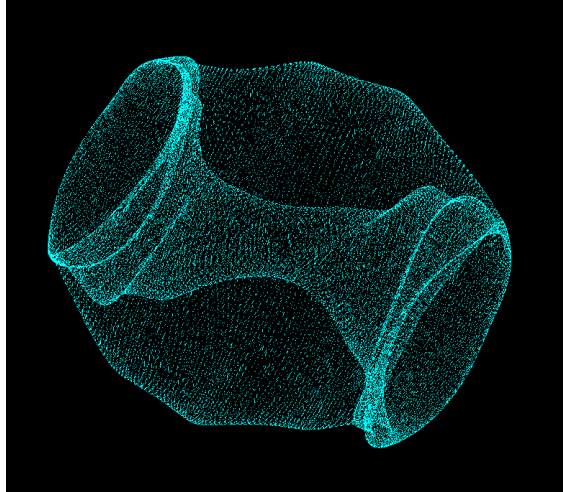


Fig. 17. $n = 4$, 3-D Projection, $k = 1$, $EC = (1, -1, 1, -1)$

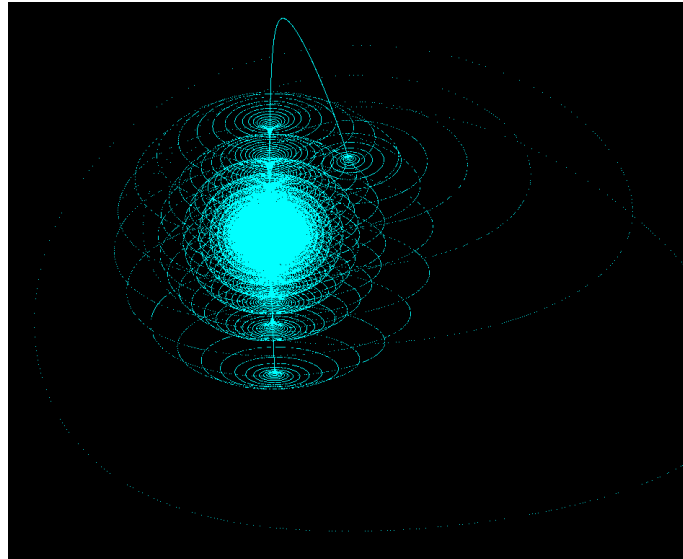


Fig. 18. $n = 4$, 3-D Projection, $k = 12$, $EC = (1, -1, 1, -1)$, $d = (3, 0, 3, 0)$

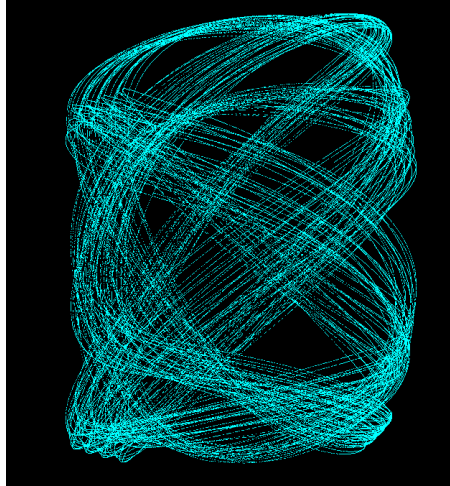


Fig. 19. $n = 5$, 3-D Projection, $k = 1$, $EC = (1, -1, 1, -1, 1)$, $d = (4, 0, 4, 0, 4)$

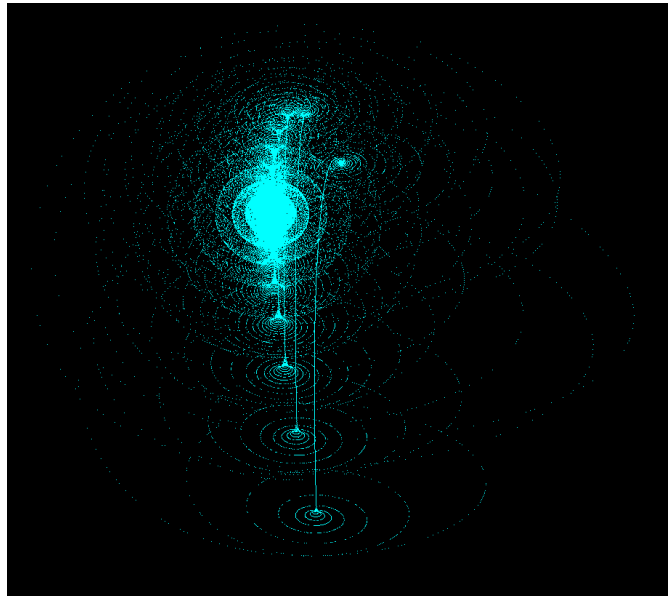


Fig. 20. $n = 6$, 3-D Projection, $k = 6$, $EC = (1, -1, 1, -1, 1, -1)$, $d = (5, 0, 5, 0, 5, 0, 5)$

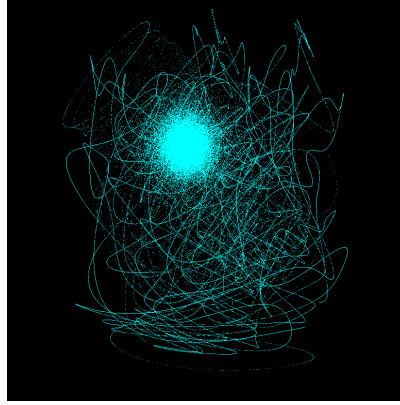


Fig. 21. $n = 10$, 3-D Projection, $k = 12$, $EC = (1,1,1,1,1,1,1,1,1,1)$,
 $d = (9,9,9,9,9,9,9,9,9,9)$

5. Measure of Chaos/Exponents

Since the map can be extended to an arbitrary number of dimensions n and singularities, we can have a higher-dimensional chaos located in or on hyperspheres with rotation axes defined by hyper-planes, so it could be called hyper-chaos [5,6] or hyper-sphere chaos. As a measure of chaos we have computed the mean space trajectory separation exponent in n -D between two nearby vectors $\mathbf{p}_{1,t}, \mathbf{p}_{2,t}$ for one complete n -D iteration step during the time τ averaging $0 < i < I$ successive steps with $t = i\tau$

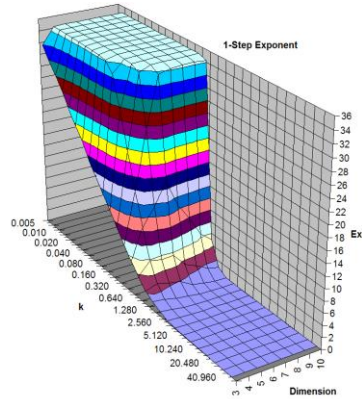


Fig. 22. The 1-step exponent E_τ for $n = 3, 4, \dots, 10$ dimensions and $I = 500$

$$E_\tau = \frac{1}{I} \sum_{i=0}^{I-1} \log \left[\frac{|\mathbf{p}_{1,t+(i+1)\tau} - \mathbf{p}_{2,t+(i+1)\tau}|}{|\mathbf{p}_{1,t+i\tau} - \mathbf{p}_{2,t+i\tau}|} \right], \quad (14)$$

which is a cheap estimate of the Lyapunov exponent. This exponent is highly stable and increases with the number of dimensions n and with the amplitude/strength factor k of rotation, see fig 24. In our simulation the 1-step exponent E_r was in our case limited to about 35 due to the double precision limit of the floating point computing unit. It starts to increase strongly near to the control parameter value $k = 0.5$, see eq.(12). There the pattern becomes "randomized" and chaotic especially at higher hyper sphere rotation dimensions. At higher exponents we find that the map is a good pseudo-random number generator in any dimension $n > 2$. Fig. 22 was obtained without expansion or compression $EC = (1,1,1, \dots)$ like all of shown patterns in all figures. With compression-reflection coefficients smaller 1 like $EC = (0.99, 0.99, 0.99, \dots)$ we get negative exponents for $k \gg 0.5$ and in-spiralling towards the centre.

6. Cryptography with Hyper-Chaos on the Hyper-Sphere

The rotations $\mathbf{R}_{a,b}$ part of the global sequence $\mathbf{R}_{A,B}$ do not commute, so the time ordering is crucial. The non-commutative permutations of the non-abelian group elements are relevant for encryption purposes. If the permutation is a sequence with a selection of K elements out of $L = N(n-2) = n(n-1)(n-2)/2$ rotations that contains each element once, the number of combinations is given by $C = L!/(L-K)!$. Knowing the rotation angles $\mathcal{G}_{a,b,l}$ and the global sequence $\mathbf{R}_{A,B}$, the rotation can only be reversed by applying the rotations and expansion/reflections part of $\mathbf{R}_{A,B}$ in reversed order. This is an encryption given by a rotation permutation from a series of linked non-commuting mathematical operations, where decryption is done by simply reversing the process applied to signal packages containing some bits of information. The key complexity defining the variations in the rotation sequence would be given by the permutation of combinations. In addition there is the freedom to choose the rotation angles, the initial condition in the signal $\mathbf{p}_0 = \mathbf{p}_i(t=0)$, and the singularity locations $\mathbf{s}_{a,b,l}$ with given precision. Secret key sharing could be done by hiding the initial conditions $\mathbf{p}_0 = \mathbf{p}_i(t=0)$, the singularity locations $\mathbf{s}_{a,b,l}$, and eventually some rotation axes \mathbf{X}_b with Blakley's scheme from the intersection of distributed planes \mathbf{P} [7], where any of the N nonparallel 2-dimensional hyperplanes intersect at a specific point or axis, and each participant is given enough information to define one of the hyper-planes \mathbf{P} . Of course, key-shifting during the sequence could also be introduced, which could be done by mobile singularities providing for extreme confusion and diffusion properties. Thus reversibility is practically limited to a small number of encryption/decryption operations due to a limited calculation precision and the high exponential divergence and pseudo-randomness, see fig. 24.

7. Mobile Singularities Exchanging Momentum Quanta

Up to now the simulated singularities had a static location. But a physical situation usually requires mobile singularities.

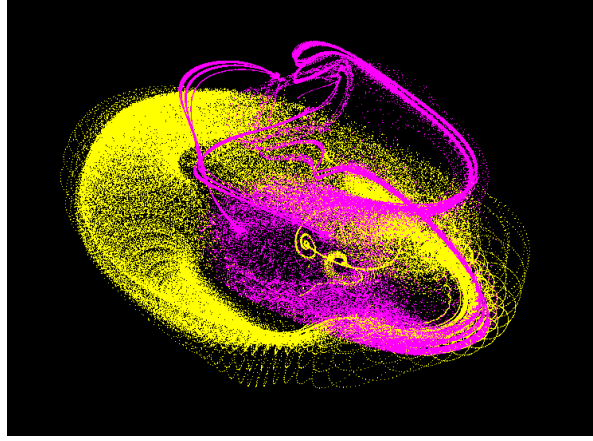


Fig. 23: Two massive mobile singularities generating and absorbing yellow and pink signals carrying momentum and providing for a vector-field.

An important extension would be given by mobile singularities $\mathbf{s}_{a,c,l} \rightarrow \mathbf{s}_{a,c,l}(t) = \mathbf{s}_{t,a,c,l}$ or mobile rotation axes carrying momentum like spinning particles with spin – orbit coupling. In the real world the emission or absorption of a rotation-translation or rotation-rotation signal would transfer a linear or angular momentum quantum to and from the singularity if it has a nonzero angular momentum. In addition to the various possibilities to introduce local rotations and accelerations from distance-dependent interactions between singularities is to provide for an extra rotational interaction dynamics between two mobile singularities $\mathbf{s}_{t,a,c,l}$ and $\mathbf{s}_{t,b,c,l}$, there could be a common rotation $\bar{\mathbf{R}}_{t,c}(\bar{\mathcal{Q}}_{t,c})$ with common axis $\bar{\mathbf{X}}_c$ (length is the rotation angle) performing the interaction of singularities. Here are two possibilities:

- (1) parallel to one of the rotation axes $\bar{\mathbf{X}}_c \parallel \mathbf{X}_a$ or $\bar{\mathbf{X}}_c \parallel \mathbf{X}_b$ or
- (2) orthogonal to the interacting singularities rotation axis $\bar{\mathbf{X}}_c \perp \mathbf{X}_a \perp \mathbf{X}_b$, $\bar{\mathbf{X}}_c = \mathbf{X}_a \times \mathbf{X}_b$ having SO(3) symmetry with new interaction singularity located on the intersection of the three axes.

To get something like a mass or providing for inertia and angular momentum a density of visited points after many jumps at time t or spatial sampling function dependent on the initial conditions $\rho_{t=0}$ could be defined by

$$\rho_{t=t_r}(\mathbf{x}) = \frac{1}{I} \sum_{i=0}^{I-1} \delta(\mathbf{x} - \mathbf{p}_{it}). \quad (15)$$

With the expanded density by $\tilde{\rho}_t = \mathbf{E}[\rho_t]$, $\mathbf{E}^{-1}[\tilde{\rho}_t] = \rho_t$ we get the difference operator equation $\mathbf{R}_{A,B}[\tilde{\rho}_t] = \mathbf{E}^{-1}[\tilde{\rho}_{t+\tau}]$. Equilibrium is approached for $\tilde{\rho}_t \approx \tilde{\rho}_{t \rightarrow \infty}$.

8. Discussion

How do patterns emerge from eq.10? At the present stage we just start to explore the very rich system of pattern formation from map parameter and initial value customization. Without systematic approach this task is hard to do. A basic pattern property at lower dimensions can be assigned to the sign of the reflection exponent, a negative sign leads to an up/down oscillatory behaviour in the jumps shaping the pattern in the altitude, see fig. 13. In the other direction the orbital loops with $\theta_{j,M} = 2\pi j / M$ around axes at coupling exponent $d = 0$ can provide at any radius M/j orbital jump position that are only slightly shifted after every loop, see figs 9-16. At higher dimensions even at high k -values (see figs 19, 21, and 23) the patterns look often more random than the nice structures and symmetries that can be easily obtained at lower dimensions, see figs 1-16. In 4, 5, and 6 dimensions we found interesting structures just by trial, see 17-20. The Skiadas singularity rotation varies with radial distance to the singularity and coupling factor or rotation strength $1/k$ as an important tuning parameter to obtain the pattern structures, see figs. 12-15 and 22. The smaller k , the higher the extra rotation providing for a more nonlinear behaviour and chaotic or even pseudo-random stochastic structure in the pattern, especially near the equatorial location of the singularity, see fig. 12 right. Subject to periodic boundaries and closed loop/orbits our chaotic jump functions show especially at higher k values in the non-chaotic regime ($k \gg 1$) a small chaotic core at the centre. At strong rotations the divergence and exponents can grow unbounded, see fig 22, leading to pseudo-random patterns. Due to the singularity on the orbit there is no perfect rotational M -gonal symmetry, the angular parts are slightly different, most different is the orbital part where the singularity is located, see fig. 13, where every dipole has a slightly different shape, especially the chaotic core is different.. Smaller shifts produce traces and linear flows with basic symmetries known from other fields. At special values of j , k , and initial conditions we get almost M -independent regular structures like rings and waves or dipole type flows, see figs 9-15.

It can be found that the path and singularity determines the shift, which is typical for geometric shifts or phases. In physics this extra shift is known as a geometric phase emerging on curved surfaces. In [8] we have presented a strange attractor involving geometric phases from three rotations on the sphere, where a linear rotation – translation coupling (rolling or helical paths) provides for simplifications with very interesting holonomic attractor singularities from iterations. We think that the geometric phase interpretation and correspondent phase shift concepts are also valid here, but near to the singularities or “monopole charges” the geometric phase extra rotation is small compared to the

singularity rotation. Since sum of the rotations given by the rotation vector field provides for a vector potential it is not surprising that the patterns at small coupling strengths and far away from singularities look like iso-potential lines for inverse power interaction laws, in fig.9 for a magnetic dipole chain and in fig.10 for a shear flow or pendulum chain. For smaller couplings $1/k$ we get the some rather linear physical properties:

- monopoles and dipoles (dipole see fig. 1b and chain in fig. 9),
- twistorial spin (vortex structures, see fig. 1 and 20, helical twist fig. 6),
- parity properties and even/odd symmetries (see figs. 3-5),
- j and M could be interpreted as spin and orbital number, respectively,
- inbuilt constant propagation velocity in the translation or rotation in eq. (2),
- Gauss flux exponent d in $n = d + 1$ dimensions,
- wave/particle duality with discrete jumps providing for density patterns,
- scalar and vector fields with standard gauge symmetries,
- angular momentum transfer, interaction and kinetic energy.
- hierarchy of patterns, see figs. 18 and 20,

Opening the loop and translating it into a helical path keeps the basic pattern units if proper periodic boundaries with reflection are introduced. Remarkably, periodic rotation-rotation dipole-dipole interaction patterns emerge on the spherical or helical loop, where the characteristic flux lines are emitted from a chaotic core, see figs. 9, 12-16. Dipole chain patterns play a very important role for living organisms since the molecular dipole interaction leads to protein folding. “Every process of protein formation, from the binding of individual amino acids to secondary structures to tertiary structures and even the formation of quaternary structures is dependent on dipole-dipole interactions [9].”

4-D patterns projected to 3-D show often torus shapes, see fig. 17, typically relevant to Hamiltonian system of spin-spin and spin-orbit coupling. $\text{Spin}(n)$ is simply connected and so coincides with the universal cover of $\text{SO}(n)$ with isomorphisms and decompositions among the classical Lie groups like $\text{Spin}(2) = \text{U}(1) = \text{SO}(2)$, $\text{Spin}(3) = \text{SU}(2)$, $\text{Spin}(4) = \text{SU}(2) \times \text{SU}(2)$, $\text{SU}(4) = \text{Spin}(6)$. So $\text{Spin}(2)$ and $\text{Spin}(3)$ structures can be embedded together in $\text{Spin}(4)$. The same can be done in arbitrary high dimensions providing in our case for interplay of low-dimensional ordered states part of a higher-dimensional chaos. This could point to a kind of “itinerancy” [10]. Figs. 18 and 20 show connected (by thin wormholes) lower-dimensional chaotic structures embedded in 4-D and 6-D higher-dimensional systems with very low LE in the projection to three dimensions. This could have relevance to the standard model high energy particle physics with separable but interconnected subgroups in the 10-D gauge field embeddings $\text{SU}(3) \times \text{SU}(2) \times \text{U}(1) \sqsubset \text{SU}(5)$ [4].

Introducing mass and momentum, mobile singularities emitting and absorbing the jumping chaotic signal quanta carrying momentum and travelling at constant

speed provide for a very rich chaotic behaviour and dynamics, see the special example in fig. 23.

9. Conclusions

We conclude that using an iterative reflection-rotation-rotation/translation difference equation modelling approach according to Skiadas we can obtain many new interesting patterns with attributes similar to those known from physics. The multiple rotation formula generating hyper-sphere chaos can be extended to an arbitrary number of dimensions, rotations, and singularities. Mobile singularities could even produce more chaos. If the singularity is located at very large distances a small rotation can approximate a translation. At special numbers with smaller coupling $1/k$ and special initial conditions regular structures like rings, spirals, and waves or the many dipole-dipole interaction flows emerge, which could be promising for molecular science and new basic level concepts. Important for a pattern generation on the orbit is a tiny but nonlinear shift in both angular variables due to a cyclic and path dependent singularity extra rotation that is small compared to the orbital angular steps and more linear at smaller coupling (higher k) values. The hyper-sphere chaos from rotation permutations could act as a pseudo-random generator of chaotic patterns relevant for crypto applications with key given by initial conditions and the special rotation permutation sequence in higher dimensions.

References

1. C. H. Skiadas and C. Skiadas, Chaos in Simple Rotation-Translation Models, <http://arxiv.org/abs/nlin/0701012>, nlin.CD, 2007.
2. C. H. Skiadas and C. Skiadas, *Chaotic Modeling and Simulation: Analysis of Chaotic Models, Attractors and Forms*, Taylor and Francis/CRC, London, 2008.
3. C. H. Skiadas, Von Karman Streets Chaotic Simulation, *Topics on Chaotic Systems*, C. H. Skiadas, I. Dimotikalis and C. Skiadas, (Eds), World Scientific, 309-313, 2009.
4. M. Kaku, *Hyperspace: A Scientific Odyssey Through Parallel Universes, Time Warps, and the Tenth Dimension*, Oxford University Press, 1994.
5. O.E. Rössler, „An equation for hyperchaos“, Phys. Lett. A 71, 155, 1979.
6. G. Qi, D. L. Owuor, A. E. Botha, Robustness and Bit Error Rate Performance of Qi Hyper Chaos Based Encryption, *CHAOS2012 Proceedings*, C. H. Skiadas, I. Dimotikalis, and C. Skiadas, (Eds), 2012.
7. G. R. Blakley, "Safeguarding cryptographic keys". Proceedings of the National Computer Conference 48, 313–317, 1979.
8. B. Binder, Magic Angle Chaotic Precession, *Topics on Chaotic Systems*, C. H. Skiadas, I. Dimotikalis, and C. Skiadas, (Eds), World Scientific, 31-42, 2009.
9. Chem Wiki for Dipole-Dipole Interaction, <http://chemwiki.ucdavis.edu>, search "Dipole-Dipole_Interactions", accessed 5.5.2012.
10. K. Kaneko, I. Tsuda, "Chaotic Itinerancy", Chaos 13(3), 926-936, 2003.

Extraction of the Dominant Features of Complex Dynamics in Experimental Air-Water Two-Phase Flows

Alberto Fichera, Arturo Pagano

University of Catania, Department of Industrial and Mechanical Engineering,
Viale Andrea Doria, 6, I-95125 Catania, Italy
E-mail: apagano@diim.unict.it

Abstract: This paper proposes an innovative approach for the characterisation of the experimental dynamics of two phase flows. These class of systems can express a great variety of different flow patterns, whose characterisation and classification strongly depends on the approach used for feature extraction. Phase space analysis in a traditional delayed embedding has allowed for the observation of the complex dynamics of the system. Nonetheless, the attractors obtained in a delayed embedding, though characterised by a regular complex structure, appear partly folded and are affected by noisy hydrodynamic high order dynamics.

The present paper proposes an application to a case study, represented by an experimental air-water two-phase flow in upward motion inside a vertical pipe, of a Singular Value Decomposition (SVD) approach with the aim of assessing a more appropriate embedding into the phase space spanned by the principal vectors. Reported results demonstrate the ability of the of the proposed methodology to separate the dominant features of the system dynamics from noise-like dynamics, leading to obtain efficaciously unfolded and noise-free versions of the system attractors.

Keywords: Feature extraction, Two-phase flows, Experimental nonlinear dynamics, SVD analysis.

1. Introduction

Several basic industrial processes, ranging from power generation, chemical and processing plants to oil pipelines, present heat and mass transfer applications of two phase flows. When two phase flows occur, very different flow patterns can be observed as well as transitions from a flow pattern to another. Indeed, the dynamical behaviours associated to the various types of flow pattern established in the system represent critical factors for the performances of such industrial systems. This explains the great efforts that have been and are still devoted to flow patterns identification, which represents a fundamental basis for appropriate characterisation of two phase flow systems.

The dynamics of two phase flows are typically of highly complex pulsating nature, under the effect of several nonlinearities deriving from the strong coupling of different mechanisms and of the dependence on various factors.

Among the others, the most important factors are the differential action of gravity on the two phases and the effect of shear and surface tension forces at their interface. As a consequence, several different flow patterns can be identified, each of which can be characterised in terms of the dynamical behaviour of the void fraction time series.

Among the other, two phase flows of air-water mixtures are often theoretical and experimental analysed with the aim of achieving a reference perspective on the general dynamical behaviours, often valid also for more complex flows, such as those arising in presence of phase changes. In particular, the present study aims at analysing the behaviour of ascending air-water two phase flows in vertical pipes. For this kind of flows heat transfer phenomena connected to phase change are not involved, so that the flow pattern established in the system mainly depends on the mass flow rates of the two phases. By varying the mass flow rate of the two phases, in fact, bubbly, slug, churn and annular flows can be identified as the main flow patterns typical of several classifications [1-3].

The bubbly flow exists for low values of the gas mass flow rate and consists in the motion of dispersed and small gas bubbles in the liquid phase. Coalescence phenomena are at the basis of the transition from bubbly to slug flow, which can be observed by increasing the gas mass flow rate. Slug flow is characterised by gas bubbles, namely Taylor bubbles, enveloped by a liquid film separating them from the pipe walls, alternated to liquid slugs. In the class of slug flow, it is possible to distinguish between: *cap flow*, with short air bubbles (with the head approximately connected to the tail) separated by long liquid slugs; *plug flow*, with gas bubbles and liquid slugs of comparable length; proper *slug flow*, characterised by elongated gas bubbles separated from relatively short liquid slugs, often aerated for the presence of small dispersed air bubbles.

For growing gas mass flow rate, bubble coalescence and increasing aeration of the liquid slug leads to a highly unstable flow pattern addressed as *churn flow*, characterised by waves propagating through the liquid film enveloping the bubbles and occasionally falling within the tube, so to form a short, unstable and highly aerated liquid slug. Finally, the annular flow consists of a thin annular liquid film at the tube wall on which small ripples, interspersed occasionally with large disturbance waves, flow in a regular manner up the tube.

It is usual practice to perform flow pattern identification on the basis of the differences of the dynamical behaviour of the time series of the local void fraction. Therefore, the reliability of the identification approach is highly dependent on the accuracy of the technique adopted to measure the void fraction. Several techniques have been proposed [4-9] and impedance measurements seem to be recognized as the most reliable [6]. At the same time, the performances of flow pattern identification approaches depend also on the techniques adopted for time series analysis and feature extraction. Statistical [1, 2, 6] or spectral [9-12] techniques indeed represent the typical approach for flow patterns identification on the basis of the analysis of the experimental void fraction time series. Nonlinear techniques have been also adopted, among the others see [10, 13-16], but a main drawback has been represented by the relatively poor spatial and temporal resolution of the experimental time series.

In order to address this problem, the experimental time series considered in the present study have been detected by means of a resistive probe characterised by high temporal and spatial resolution, which has been appositely set-up as described in [17]. The preliminary analysis in a delayed embedding of the void fraction time series detected by means of this sensor has shown the existence of strange attractors of interesting morphology for the various flow patterns [18]. Nonetheless, attractors obtained in this way are somewhat noisy as a consequence of the superposition of high order dynamics to the dominant dynamics characterizing the flow pattern. Among the others, the most important high order “noisy” dynamics are those of hydrodynamic nature associated to small diameter bubbles dispersed in the liquid slugs and to disturbances on the liquid film enveloping the Taylor bubbles.

Therefore, the present study aims at extracting the dominant features of the flow dynamics under various flow pattern conditions so to separate the dominant features of the system dynamics from noise-like dynamics. The proposed approach is analogous to that proposed in [19] and is based on the calculation of the singular vectors of a n -dimensional delayed embedding, through the application of the technique known as Singular Value Decomposition (SVD) [20], and in the analysis of the restricted portion of the dynamics that is obtained by projecting the attractor onto the phase space spanned by the singular vectors corresponding to the three highest singular values.

Reported results, show that the attractors described in the new embedding present a well defined and regular structure, indicating the existence of a low order source of the system dynamics, which will be analysed in future studies.

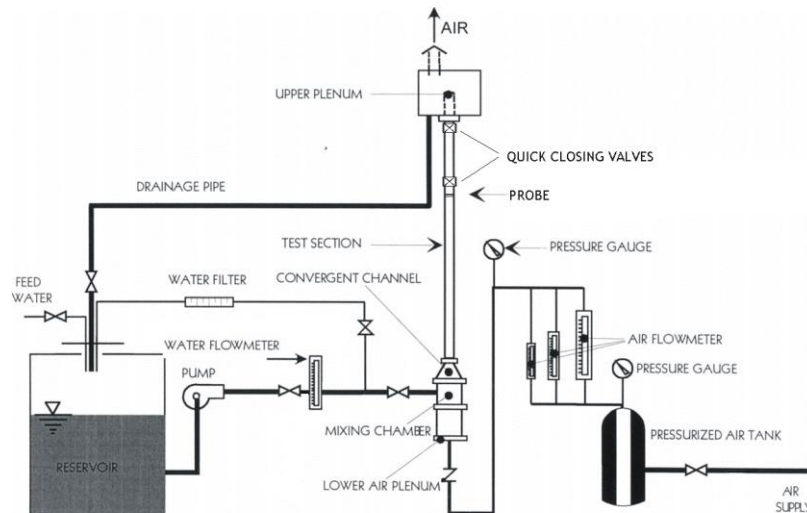


Fig.2 Experimental apparatus

2. Experimental Apparatus

The experimental apparatus reported in Fig. 1 has been built and tested in order to study the dynamics of two-phase flow in vertical pipes. The test section is a vertical pipe of diameter 0.026 m and length 3 m. The apparatus is equipped by an electromagnetic flowmeter and three air flow metres, respectively used for the measure of the water velocity and mass flow rate and for the regulation of the air flow rate in the range between 10 and 210 l/min. The air is supplied to the mixing section by a pressurised tank fed by a compressor, whereas the water flow rate can be varied in the range 0-150 l/min by means of a series of valves and bypasses placed at the pump outlet.

A resistive probe for the measure of the void fraction is placed at a distance of over 100 times the diameter of the pipe from the mixing section, i.e. over the required entry region for two phase flows, in order to ensure a well established flow regime. In particular, the void fraction probe has been designed and realised for the experimental campaign and operates in the resistive range (carrier frequency of 20 kHz). The sampling frequency was set at 1 kHz with a cut-off frequency of 200 Hz. A detailed description of the experimental probe and on the wide set of experimental tests performed is reported in [17].

3. Dynamical Feature Extraction

The results of preliminary linear analyses of the experimental time series have been shown to be unable to deal with the intrinsic complexity of two phase flows dynamics. Hence, in [18] a morphological analysis of the three-dimensional attractors has been proposed in a classical Takens' delayed embedding of the experimental void fraction time series [21]. In particular, it has been observed that the attractors obtained for some of the flow patterns are characterised by a regular fractal structure, which is indeed one of the most important evidences of deterministic chaotic behaviour.

In the present study, the aim is to improve the dynamical representation by adopting a new embedding, derived through the application of *Singular Value Decomposition* technique, *SVD* [20], to the classical delayed embedding based on Takens' theorem, similarly to the approach proposed in [19]. The new representation is characterised by a drastic reduction of noisy dynamics and, above all, a sensitive improvement of the attractor unfolding, so that the dominant morphological characteristic can be fully exploited.

As a first step, the phase space reconstruction consists in the creation of a $n \times w$ matrix, S , where n is the length of a window moving through the data and w are the independent variables defining the phase space, i.e. delayed version of the experimental void fraction time series $s(t)=(s_0, s_1, s_2, \dots, s_p, \dots)$, with each column delayed τ time steps from the previous. The condition $w > 2d+1$ for an appropriate embedding is implicitly respected if w is set much greater than the unknown fractal dimension d on the basis of a preliminary estimation.

The second step consists in the application of the *SVD* approach to matrix S . This is done through the calculation of a new diagonal matrix, equivalent to the original one, i.e. with identical singular values but in decreasing order. In particular, S is factorized into its singular values according to equation:

$$\Lambda = M^T S C \quad (1)$$

In (1) Λ is the diagonal matrix containing the w singular values λ_i of S in decreasing order and M and C are the matrices of the singular vectors associated with Λ . Details on the factorization can be found in [20]; what is interesting for the scopes of the present study is that the high level singular values in Λ are associated to the dominant singular vectors, i.e. those representing the dominant features of the system dynamics, whereas the low level ones correspond to local behaviors or noise-like components. Therefore, the system can be virtually partitioned into two subsystems: the first deriving from noise free data (i.e. the main features and the relevant details) and the second from noisy dynamical behaviours, which can be considered superimposed and then eliminated.

In order to choose how many singular vectors are needed to accurately describe the dominant dynamics of the system, it is possible to analyse, under the various possible flow patterns, the distribution of the spectrum of the normalized singular values $(\lambda_i)_n$, obtained by dividing the singular value λ_i for its maximum $(\lambda_i)_{max}$ under the given flow condition. By the analysis of the spectrum of the singular values reported in Fig. 3 for some cases representative of the typical flow patterns, it is possible to observe that only the three highest singular values are relevant in the spectrum and can therefore be chosen to describe the dominant dynamics of the system. It is worth observing that even for the flow patterns that seem to require the consideration of a higher number of singular values, it is possible to claim that only the three highest are actually relevant. The rising of higher order singular values in the *bubbly flow* and *cap flow* spectrum is due, in fact, to the comparatively lower amplitude of the void fraction oscillations under these flow conditions, which determines a greater relevance of noisy dynamics of hydrodynamic origin.

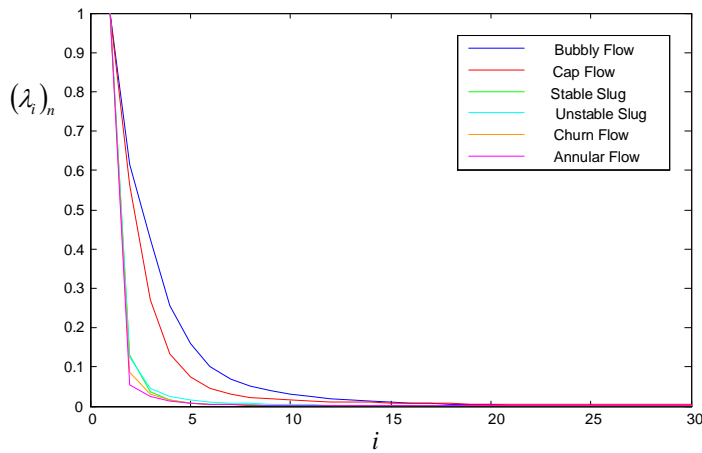


Fig.3 Spectrum of the normalised singular values under various flow patterns.

4. Results and Discussion

The described approach has been used in the present study in order to obtain a denoised and unfolded representation of the experimental dynamics. The *SVD* technique has been applied to the delayed embedding S of the experimental void fraction time series, created considering $\tau=1$ and $w=40$ in order to ensure that w is sufficiently greater than m , i.e. greater than the (unknown) system dimension. The length n of the observation window has been set at 10000 data samples in order to be wide enough to obtain a well defined attractor in phase space, i.e. an attractor whose morphology does not change if further data samples are added. The claimed advantages of the proposed methodology can be observed in the results reported in the Fig. 4 to 9, which report the attractors of the same operating condition in two different embeddings. In particular, the phase space adopted for the plots on the left hand side of each figure is the basic three dimensional Takens' delayed embedding, whereas the projections on the pseudo-phase space spanned by the three dominant principal vectors of the improved embedding obtained through application of *SVD* are those reported on the right hand side of each figure. It is worth observing that, as discussed on the basis of previous observations on the spectrum of the singular values, the three-dimensional pseudo-phase space can indeed be considered an appropriate embedding for the dominant dynamical behaviour under the various flow patterns.

By comparing the two methods of representation it is possible to observe that the attractors in the delayed phase space are in all cases sensibly affected by a higher noise level and are not sufficiently unfolded with respect to the corresponding attractors in the principal component embeddings, the last being characterised by a very low level of noise and a satisfactory unfolding. It is worth to remind that, even if the two attractors of each flow pattern appear different, they are, nonetheless, expressions of the same dynamical behaviour. In fact, they are morphologically equivalent and, therefore, characterised by the same *invariants of the dynamics*, such as fractal dimension and Lyapunov exponents [22-25].

The successful unfolding contributes to the achievement of a clear and well defined morphology of the attractors. This is a main advantage for the distinction of different flow patterns through a comparison of the representation of their dynamics in the phase space spanned by the principal components.

Moreover, in some cases the proposed embedding amplifies important characteristics of the system dynamics. For example, the right hand cap flow attractor in Fig. 5 shows a clear distribution of the trajectory in alternated bands, which is a hint of the fractal (i.e. chaotic) nature of the system dynamics.

Finally, the representation in the principal component phase space is very effective in underlining the differences between the various flow patterns.

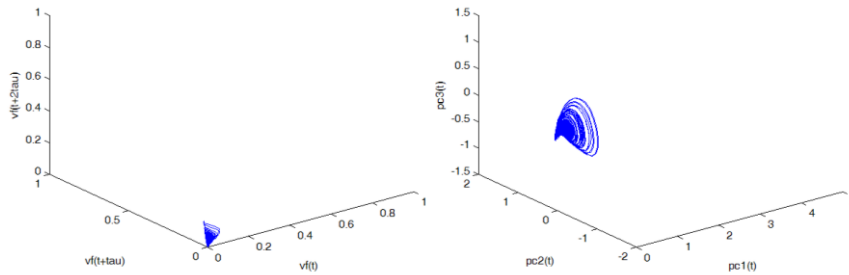


Fig.4 Attractors in the delayed and principal component embeddings for the bubbly flow; air flow rate 2 lit/min - water flow rate 32.4 lit/min.

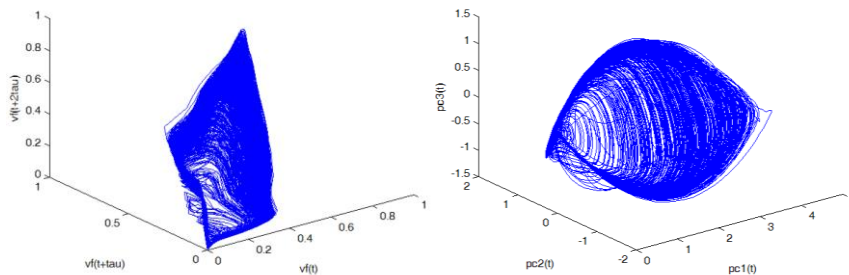


Fig.5 Attractors in the delayed and principal component embeddings for the cap flow; air flow rate 5 lit/min - water flow rate 20.28 lit/min.

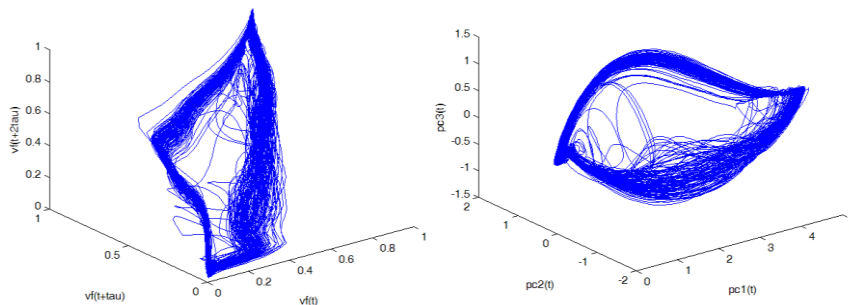


Fig.6 Attractors in the delayed and principal component embeddings for the plug flow; air flow rate 10 lit/min - water flow rate 9.06 lit/min.

Each type of flow pattern is, in fact, characterised by a specific morphology, sufficiently different from that of the other flow patterns.

In particular:

- each flow pattern attractor occupies a different phase space region;
- each attractor differently “fills” its own region of phase space; for example, the cap flow attractor (properly 3-D) has a higher filling rate than that of the plug flow (which moves around a sort of 2-D limit cycle);

- the attracting region is progressively shifted, with a continuous trend from bubbly to annular flow, with respect to the first principal component.

These differences are very important as the morphological considerations drawn insofar are related to the fractal nature and to the stretch and folding behaviour of the attractors [24], which can be considered as the topological expressions of the mentioned invariants of the dynamics, whose calculation is behind the scope of the present study and will be the object of future studies.

5. Conclusions

This study proposes a phase space approach for the description of typical complex dynamics of two-phase flow. At first the singular vectors of the classical delayed embedding are calculated and the attractors of the system dynamics are projected on the state space spanned by these eigenvectors. In this way the dominant feature of the dynamics, corresponding to a subset of the highest singular values, are separated from noisy dynamics in the time series, corresponding to the remaining lower singular values. The morphology of the attractors in the obtained unfolded and noise-free representation is analysed. Reported results demonstrate that the proposed approach represent a powerful tool for the identification of two-phase flow patterns.

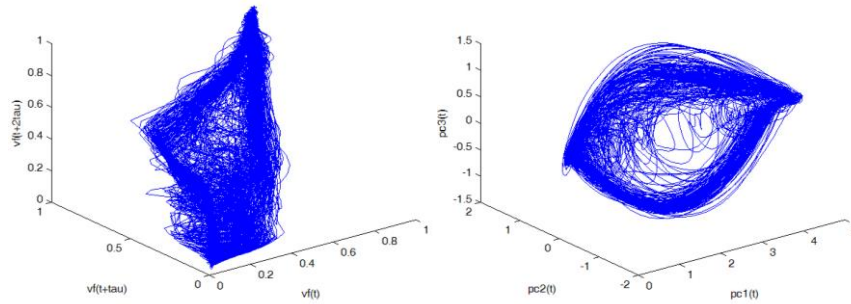


Fig.7 Attractors in the delayed and principal component embeddings for the slug flow; air flow rate 40 lit/min - water flow rate 16.80 lit/min.

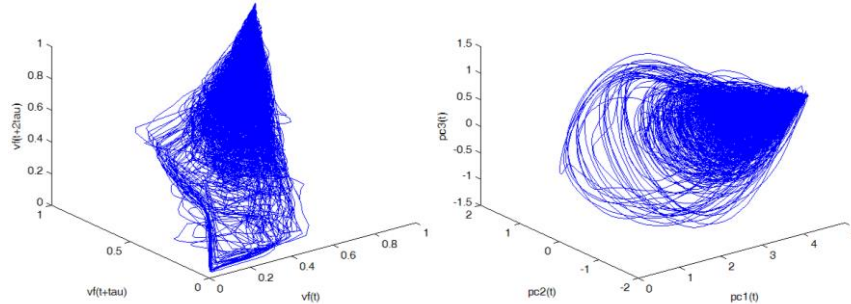


Fig.8 Attractors in the delayed and principal component embeddings for the churn flow; air flow rate 80 lit/min - water flow rate 9.01 lit/min.

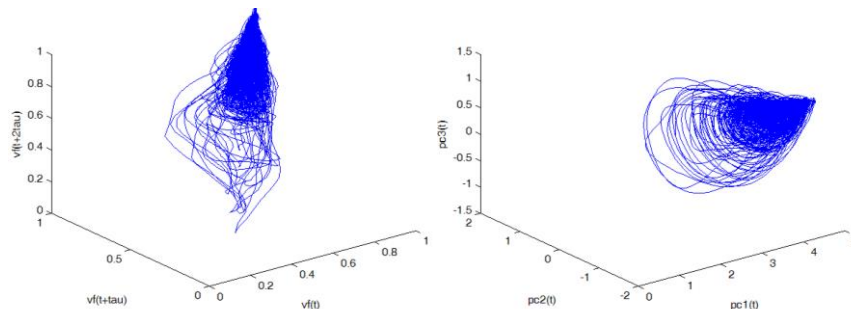


Fig.9 Attractors in the delayed and principal component embeddings for the annular flow; air flow rate 80 lit/min - water flow rate 5.58 lit/min.

References

1. G. Costigan, P. B. Whalley, Slug flow regime identification from dynamic void fraction measurement in vertical air-water flows, *International Journal of Multiphase Flow* 23, pp 263–282, 1997.
2. Y. Mi, M. Ishii, L. H. Tsoukalas, Vertical two-phase flow identification using advanced instrumentation and neural networks, *Nuclear Eng. Design* 184, pp 409–420, 1998.
3. F. S. Qi, G. H. Yeoh, S.C.P. Cheung, J. Y. Tu, E. Krepper, D. Lucas, Classification of bubbles in vertical gas–liquid flow: Part 1 – An analysis of experimental data, *International Journal of Multiphase Flow* 39, pp 121–134, 2012.
4. F. Devia, M. Fossa, Design and optimisation of impedance probes for void fraction measurements, *Flow Measurement and Instrumentation* 14, pp 139–149, 2003.
5. D. Lowe, K. S. Rezkallah, A capacitance sensor for the characterization of microgravity two-phase liquid-gas flows, *Measurement Science and Technology* 10, pp 965–975, 1999.
6. J. K. Keska, B.E. Williams, Experimental comparison of flow pattern detection techniques for air-water mixture flow, *Exp. Thermal Fluid Science* 19, pp 1–12, 1999.
7. P. Andreussi, A. Di Donfrancesco, M. Messina, An impedance method for the measurement of liquid hold-up in two phase flow, *International Journal of Multiphase Flow* 14, pp 777–785, 1988.
8. C. Vial, E. Camarasa, S. Poncin, G. Wild, N. Midoux, J. Bouillard, Study of hydrodynamic behaviour in bubble columns and external loop airlift reactors through analysis of pressure fluctuations, *Chemical Eng. Science* 55, pp 2957–2973, 2000.
9. C. H. Song, M. K. Chung, H. C. No, Measurements of void fraction by an improved multi-channel conductance void meter, *Nuclear Eng. Design* 184, pp 269–285, 1998.
10. N. D. Jin, X. B. Nie, Y. Y. Ren, X. B. Liu, Characterization of oil/water two-phase flow patterns based on nonlinear time series analysis, *Flow Measurement and Instrumentation* 14, pp 169–175, 2003.
11. G. P. Lucas, I. C. Walton, Flow rate measurement by kinematic wave detection in vertically upward, bubbly two-phase flows, *Flow Measurement and Instrumentation* 8(3–4), pp 133–143, 1997.
12. M. J. Watson, G. F. Hewitt, Pressure effects on the slug to churn transition, *International Journal of Multiphase Flow* 25, pp 1225–1241, 1999.

13. J. Drahos, J. Zahradnik, M. Puncochar, M. Fialova, K. Chen, F. Bradka, Effect of operating conditions of the characteristics of pressure fluctuations in a bubble column, *Chemical Engineering Processing* 29, pp 107-105, 1991.
14. H. Letzel, J. Schouten, R. Krishna, C. M. van den Bleek, Characterization of regimes and regime transitions in bubble columns by chaos analysis of pressure signals, *Chemical Engineering Science* 52, pp 4447-4459, 1997.
15. J. Drahos, J. Tihon, C. Serio, A. Lubbert, Deterministic chaos analysis of pressure fluctuations in a horizontal pipe at intermittent flow regime. *Chemical Engineering Journal* 64, pp 149-156, 1996.
16. J. Y. Lee, N. S. Kim, M. Ishii, Flow regime identification using chaotic characteristics of two-phase flow, *Nuclear Eng. Design* 238, pp 945-957, 2008.
17. L. Cantelli, A. Fichera, A. Pagano, A high-resolution resistive probe for nonlinear analysis of two-phase flows, *Journal of Thermodynamics* 2011, Article ID 491350, p. 10, 2011.
18. L. Cantelli, A. Fichera, I. D. Guglielmino, A. Pagano, Non-Linear Dynamics of Air-Water Mixtures in Vertical Pipes: Experimental Trends, *International Journal of Bifurcation and Chaos* 16-9, 2006.
19. G. Cammarata, A. Fichera, A. Pagano, Nonlinear analysis of a rectangular natural circulation loop, *Int. Comm. Heat Mass Transfer* 27 (8), pp 1077-1089, 2000.
20. D.S. Broomhead, G. P. King, Extracting Qualitative Dynamics from Experimental Data, *Physica D* 20, 217-236 1986.
21. F. Takens, *Lecture Notes in Mathematics, Dynamical System and Turbulence*, D. A. Rand & L.S. Young Editions, Springer, New York, 1981.
22. J. M. T. Thompson, H. B. Stewart, *Nonlinear Dynamics and Chaos*, J. Wiley & Sons, New York, 1986.
23. S. N. Rasband, *Chaotic Dynamics of Nonlinear Systems*, J. Wiley & Sons, New York, 1990.
24. S. H. Strogatz, *Nonlinear Dynamics and Chaos, with Applications to Physics, Biology, Chemistry, and Engineering*, Perseus Books, Cambridge, 1994.
25. H. Kantz, T., Schreiber, *Nonlinear time series analysis*, Cambridge University Press, 1999.

Utilisation of the Perturbation Theory without Presuppositions. A Repeating Equation for Azimuthal Velocities into Cylindrical and Magnetized Plasma

C. L. Xaplanteris^(1,2), E. D. Filippaki⁽¹⁾, I. S. Mistakidis⁽²⁾ and L. C. Xaplanteris⁽³⁾

(1) Plasma Physics Laboratory, IMS, NCSR “Demokritos”, Athens, Greece

(2) Hellenic Military Academy, Vari Attica, Greece.

(3) School of Physics, National and Kapodistrian University of Athens, Greece.

(E-mail: cxaplanteris@yahoo.com)

Abstract: As the understanding of the chaotic state increases, it becomes clearer that the definition and the theoretical elaboration of the chaos is not a simple hypothesis. In addition, it is a commonplace fact that the mathematical representation of the chaos theory on the whole is very difficult to be given. This means that there is not any mathematical equation capable of describing and solving a nonlinear and chaotic problem. So, as every case is unique, our work has to contribute to the chaotic topic both mathematically and experimentally. Magnetized argon plasma is produced into a metallic cylinder. A coaxial antenna is used for the r-f energy importation and the plasma maintenance consequently. This device has a complete cylindrical symmetry and the mathematic elaboration in the cylindrical system is carried out. An attempt to show a repeating relation for ion velocities of magnitude of every order is presented as our new work. In addition, it is well known that the perturbation theory can be used to extend the linear theory of plasma waves into the nonlinear regime and, thus, give an explanation of many nonlinear phenomena. This nonlinear perturbation theory of small amplitude plasma waves and their interactions is well developed; on the contrary, the perturbation theory of large-amplitude plasma waves is still being developed. In the present paper, a generalization of the perturbation theory is attempted with the division of the perturbed magnitude and the use of the repeating estimation. Computational results and experimental findings are in a very satisfactory accordance.

Keywords: Chaos theory, Nonlinear problem, Cylindrical system, r-f plasma production, Repeating relation, Perturbation theory, Loop on the repeating relation.

1. Introduction

The stability and instability of the plasmatic state was an old problem for researchers during the last decades. Especially, in the early 60's many plasma

instabilities have been observed taking wavy forms into the plasma [1-4]. These waves absorb the plasma energy, then the plasma temperature is consequently reduced and the removal of the thermonuclear fusion conditions is resulted. So, the wavy instabilities are considered to be a serious obstacle to the nuclear fusion process and their study has been carried out constantly and in detail during the last decades [5,6]. Many special books constitute the Plasma Physics Literacy [7-10], list and study all the waves from the low frequency region [1-6] to the high frequency one [11]. In the Plasma Laboratory of the Center “Demokritos” an adequate amount of experience has been gained, especially on the low frequency electrostatic waves [12-14] and their effect on the plasma conductivity [13]. The chaotic behavior of the plasma waves has been studied as well [15,16]. It is well known that the plasma can easily pass from a steady state into a chaotic one, which was repeatedly published in our previous papers [17,18]. In the present work an attempt takes place to compare the experimental data with the computation results, and so, our theory may be confirmed. A mathematic relation, which connects the different order velocities, was found and may be used as a repeating relation showing the chaotic behavior of the plasma. The relation is valid under the condition that the perturbed qualities are small in comparison with the unperturbed one [8-10]. In the present work a calculative trial using the relation as a repeating one may bring it into the function conditions and the perturbed theory can be therefore extended. Although the experimental results are in a satisfactory agreement with the calculation, the subject remains open as a chaotic state one and requires further study. In the next research of ours, the influence of the initial conditions on the computational results is planed to be studied.

A brief description of the experimental devices is given in Sec.2, since the experimental results are presented in the following Sec.3. In Sec. 4 a full mathematical elaboration and the computational results are curried out. The confirmation between theory and experiment and conclusions are included in Sec. 5. A more detailed mathematical elaboration is provided in the Appendix at the end of the paper.

2. Description of the Experimental Set-Up

It is well known that the predominant direction of the external magnetic field \vec{B} in the Q-machine is well matched with the cylindrical geometry of the device, when the cylinder axis and magnetic field coincide. As our experience on the magnetized argon plasma is concentrated on full cylindrical symmetry, the same geometry is used at the present study as well, since the low frequencies of plasma waves are persistent [1-4, 12-14]. A cylindrical cavity made of steady

steel is located with its' axis along the external magnetic field B . The cavity is 60cm long with 6cm internal diameter and, in the center of the first disk-like base, the 25cm rf power antenna is mounted; in the other disk-like base a 25cm external driving wave antenna is mounted as well, which enables us to affect and control the plasma waves. Electrostatic Langmuir probes were fixed to move radially, azimuthally and axially with the ability to detect the plasma waves that appear and measure their physical quantities (wave frequency, wave amplitude, plasma temperature, plasma density, plasma potential e.t.c.). Furthermore, a disk-probe was fixed to move radially and around its' axis, which allows, apart from the above quantities, the measuring of the azimuthal electron drift current. In Fig.1 (a) the plasma column cut is shown, whereas an extensive drawing of the cavity's position into the magnetic field is presented in Fig.1 (b).

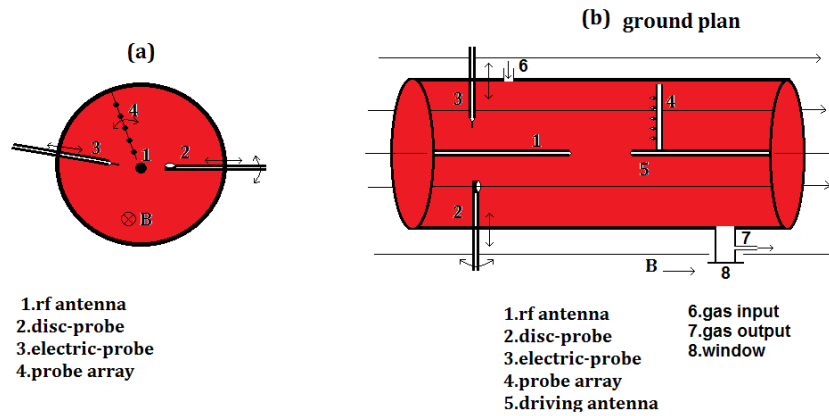


Fig.1 (a), the plasma column is shown. Fig.1 (b), the cavity's placing into the magnetic field is presented (ground plan).

The argon entrance, its' outlet to the pump and a suitable window are placed on the curved surface of the cylinder, as they are represented at the Fig.1 (b).

3. Experimental Data

The existence of the electrical waves into the argon plasma is confirmed once more. These low frequency waves are divided into three frequency regions with a quasi-same behavior in many instances. An extensive study of these waves was carried out at the Plasma Laboratory of NCSR "Demokritos" previously, and two of them were absolutely identified [12, 14]. A stable dependence of the gas pressure on the waves has been presented and measured

again. This influence consists of the simultaneous decrease of the waves' amplitude and frequency as the gas pressure increases. Figures 2 and 3 give a middle frequency region wave indicatively with its' spectrum of frequencies where the upper harmonics appear; the first with a high value of the gas pressure and the second with a low one.

The plasma is lit into an wide space of the external plasma parameters (gas pressure p , magnetic field B and rf field absorbed power P) and results in a wide region of plasma quantities as well; these quantities include the plasma temperature T , the plasma density n , the plasma potential Φ , and all the wave parameters. Table 1 shows some typical values of the plasma parameters.

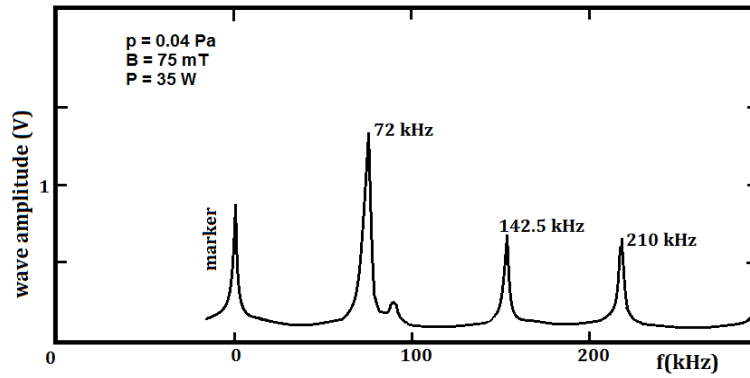


Fig. 2. A typical wave spectrum in the middle frequency region with high gas pressure.

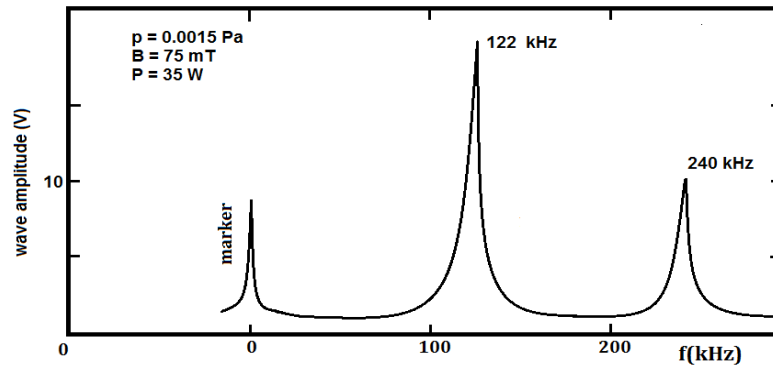


Fig. 3. A typical wave spectrum in the middle frequency region again with low gas pressure.

Table 1 The plasma parameters ranging values

Parameters	Minimum value	Maximum value
Argon pressure p	$0.001Pa$	$0.1Pa$
Argon number density, n_g	$2 \times 10^{15} m^{-3}$	$2 \times 10^{17} m^{-3}$
Magnetic field intensity, B	$10mT$	$200mT$
Microwaves' power, P	$20Watt$	$120Watt$
Frequency of the rf power (standard value)	$2.45GHz$	
Electron density, n_0	$2 \times 10^{15} m^{-3}$	$4.6 \times 10^{15} m^{-3}$
Electron temperature, T_e	$1.5eV$	$10eV$
Ion temperature, T_i	$0.025eV$	$0.048eV$
Ionization rate	0.1%	90%
Electron drift velocity, u_e	$1 \times 10^4 m/s$	$1.7 \times 10^4 m/s$
Electron-neutral collision frequency, ν_e	$1.2 \times 10^7 s^{-1}$	$3 \times 10^9 s^{-1}$

The experimental part of the present paper consists of the following steps:

- i) By using the radial moving probe, the plasma potential $\Phi(r)$ is measured along the cylinder radius and then, from the relation $\varepsilon = -\frac{\Delta\Phi}{\Delta r}$ the plasma electric field ε is calculated. Figure 4 is shows the radial potential and radial electric field along the cylinder radius.

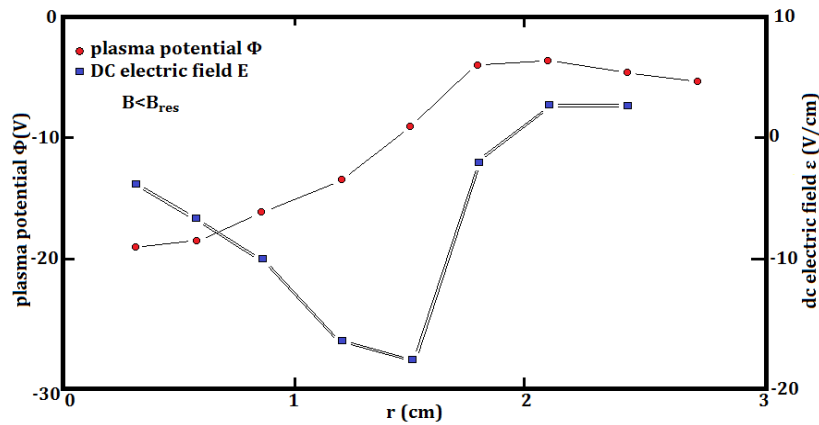


Fig.4 shows the plasma potential $\Phi(r)$ and the electric field ε along the cylinder radius.

It must be noted that the electric field ε remains nearly constant in the middle of the radius, where the wave rises and its' amplitude constantly increases [6, 12-14]. The measurement has been done by $B < B_0$.

- ii) The perturbed electric field E must be measured, consequently. This measurement may be a result of the wave amplitude as it appears along the cylinder radius. Figure 5 shows the wave amplitude (in Volts) and the perturbed field E correspondingly. The measurement was repeated for values of the magnetic field B , under and above the upper cyclotron resonance B_{res} .

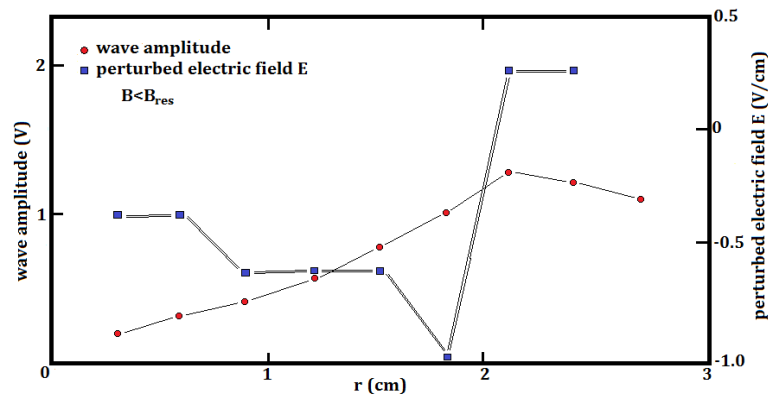


Fig. 5 shows the wave amplitude and the perturbed electric field E along the cylinder radius.

- iii) The measurement of the azimuthal electron drift velocity u_e is the next step. This is obtained by using the disk probe as it moves around its' axis. Figure 6 indicates the method of the measurement of the azimuthal electron current I_θ , which requires two simple movements: the orientation of the probe surface perpendicularly to the electron drift course, and after, in the opposite direction of the electrons' motion.

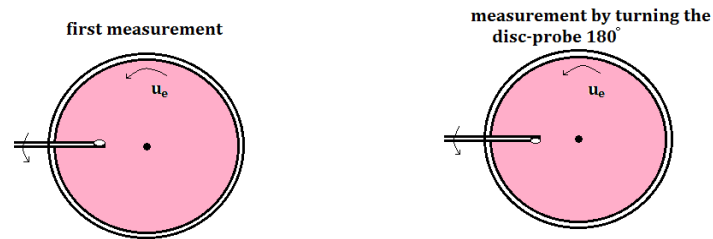


Fig. 6, the electron drift current measurement

The next relations $I_1 = I_\theta + I_{th}$ and $I_2 = -I_\theta + I_{th}$ are valid and result in the relation below,

$$I_\theta = \frac{I_1 - I_2}{2}$$

Taking into consideration that the relation $I_\theta = e n_e u_e A$ is valid (with A the probe surface area), the azimuthal electron drift can be found. Measurements and estimations are listed in Table 2, since the electron drift velocity u_e and the perturbed velocity v_θ are presented in Fig. 7, as well.

Table 2 The azimuthal electron drift current and the drift velocity along a cylinder radius

Radius r (cm)	drift current I_e (μA)	plasma density n_e ($\times 10^{15} m^{-3}$)	drift velocity u_e ($\times 10^3 m/s$)	E/ε	perturbed velocity v_θ (m/s)
0.3	20	6.0	4.43	-0.1	-443
0.6	26	6.2	5.57	-0.05	-278
0.9	30	6.5	6.17	-0.067	-413
1.2	37	7.0	7.02	0.04	281
1.5	42	6.8	8.20	0.037	303
1.8	46	6.2	9.85	0.25	2462
2.1	35	5.9	7.92	0.1	792
2.4	25	5.6	5.93	0.1	593
2.7	16	5.5	3.86		

iv) The perturbed velocity v_θ is impossible to be found directly by an experimental measuring, but it can be estimated from the relation $v_\theta = \frac{E}{\varepsilon} u_\theta$, as the quantities ε, E and u_θ have been measured above.

The results for the v_θ are given again in Table 2.

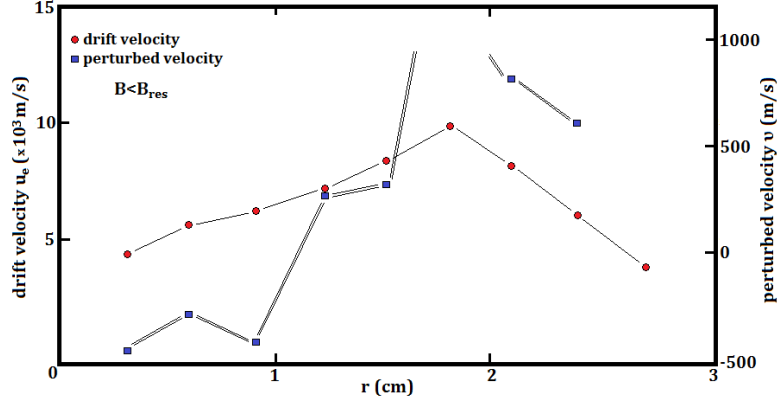


Fig.7. The drift velocity u_e and the perturbed velocity v are presented

4. Mathematical Elaboration - Computational Results

Perturbed velocities' study

In the Appendix it is proved that the drift and perturbed velocities are related to the electrical fields with the Eq. (A. 9),

$$v_r = \frac{E}{\varepsilon} u_r \quad \text{and} \quad v_\theta = \frac{E}{\varepsilon} u_\theta \quad (\text{A. 9})$$

A. When the perturbed electric field E is very small, then the relations $v_r \prec u_r$ and $v_\theta \prec u_\theta$ are valid.

B. If the relation $v \approx u$ is valid, the electric fields must have the same behavior as $E \approx \varepsilon$. This means that the wave amplitude undergoes some big changes along the cylinder radius.

With the replacement of the quantity Π , the Eqs (A. 7) are written:

$$v_\theta = \frac{E}{B} \cdot \frac{\omega_c^2}{\omega_c^2 + [j(ku - \omega) + v]^2} \quad \text{and} \quad v_r = \frac{E}{B} \cdot \frac{\omega_c [j(ku - v) + v]}{\omega_c^2 + [j(ku - \omega) + v]^2} \quad (1)$$

The azimuthal perturbed velocity v_θ is of the most interest: by taking $\Pi^2 = v^2 - (ku - \omega)^2 + j2v(ku - \omega)$ and limiting the real part only, the first of Eqs (1) is rewritten as following,

$$v = \frac{E}{B} \cdot \frac{\omega_c^2}{\omega_c^2 + v^2 - (ku - \omega)^2} \quad (2)$$

with $v_\theta = v$ for simplicity; this may be used as the repeating relation.

It must be reminded that the Eq.(A. 9) was produced with the presupposition that the relation $v \ll u$ is valid. This consists a necessary condition for the linearization of Eq. (A. 1) (perturbation theory).

Now, if we seek a solution for $v \approx u$, approximately, by separating the perturbed velocity v into small parts $v_1, v_2, v_3, \dots, v_i$ with $i = 10, 100, 1000, \dots$ and every part $v_i \ll v$, the perturbation theory condition is satisfied.

Taking $u = u_0$ and $v = v_1 \ll \frac{v}{10}$, the Eq. (2) is written,

$$v_1 = \frac{E}{B} \cdot \frac{\omega_c^2}{\omega_c^2 + v^2 - (ku_0 - \omega)^2} \quad (3)$$

With the addition $u_1 = u_0 + v_1$, the above equation gives the term v_2 ,

$$v_2 = \frac{E}{B} \cdot \frac{\omega_c^2}{\omega_c^2 + v^2 - (ku_1 - \omega)^2}$$

If it is taken $u_2 = u_1 + v_2$, the Eq. (2) gives the term v_3 ,

And so on, with $u_{i+1} = u_i + v_{i+1}$ the repeating relation,

$$v_{i+1} = \frac{E}{B} \cdot \frac{\omega_c^2}{\omega_c^2 + v^2 - (ku_i - \omega)^2} \quad (4)$$

is obtained.

Repeating equation study

It is evident that the minimum value of the term $(ku_i - \omega)^2$ is zero, and then the denominator in the Eq. (4) takes the maximum value. Then, we conclude that, at

the value $u_i = \frac{\omega}{k}$, the v_{i+1} has the minimum value, $v_{i+1} = \frac{E}{B} \frac{\omega_c^2}{\omega_c^2 + v^2}$, which is the same as if the quality $\Pi = j(ku - \omega) + v \cong v$, is taken.

Another significant result is obtained if the relations $u_1 = u_0 + v_1$, $u_2 = u_1 + v_2$, $u_3 = u_2 + v_3$, ..., $u_i = u_{i-1} + v_i$, are added by parts, when the relation $u_i = u_0 + v_1 + v_2 + v_3 + \dots + v_i$ or

$$u_i = u_0 + v \quad (5)$$

is obtained

with $v = v_1 + v_2 + v_3 + \dots + v_i$ the whole-total large perturbed velocity.

The relation $u_i = u_0 + v$ must be confirmed experimentally.

Computational results

The experiment leads to the following calculations;

$$\frac{E}{B} \cong \frac{100V.m^{-1}}{70.mT} \Rightarrow \frac{E}{B} \cong 1430 \frac{m}{s}$$

$$\omega_c^2 = \left(\frac{eB}{m_e} \right)^2 = \left(\frac{1,6.10^{-19}.7.10^{-2}}{9,1.10^{-31}} \right)^2, \quad \Rightarrow \omega_c^2 \cong 1,5.10^{20} s^{-2}$$

$$\underline{v^2 \cong 10^{19} s^{-2}}$$

When it is taken $ku_0 - \omega = 0$, then $u_0 = \frac{\omega}{k} = \frac{\omega.R}{l} \Rightarrow u_0 = \frac{\omega.R}{l}$.

Taking $\omega = 2\pi.f = 2\pi.7.10^4 s^{-1} \Rightarrow \omega = 1,4.\pi.10^5 s^{-1}$, $l = 1$ and $R = 2.10^{-2} m$ then

$$u_0 = 1,4.\pi.10^5.2.10^{-2} \frac{m}{s} \Rightarrow \underline{u_0 \cong 0,88.10^4 \frac{m}{s}}$$

In the above case the perturbed velocity v_1 is minimized at the value, (see eq. 3),

$$\nu_1 = 1430 \cdot \frac{10^{20}}{10^{20} + 10^{19}} \text{ m/s} \quad \Rightarrow \underline{\nu_1 \cong 1300 \text{ m/s}}$$

On the other hand, the relation $\nu = \frac{E}{\varepsilon} u$ gives,

$$\nu = \frac{2V \cdot \text{cm}^{-1}}{20V \cdot \text{cm}^{-1}} u \quad \Rightarrow \underline{\nu = 880 \text{ m/s}}$$

Now, with $u_1 = u_0 + \nu_1 = (8800 + 880) \text{ m/s} \Rightarrow u_1 = 9680 \text{ m/s}$, the perturbed ν_2 from the repeating equation below can be calculated,

$$\nu_2 = \frac{E}{B} \cdot \frac{\omega_c^2}{\omega_c^2 + \nu^2 - (ku_1 - \omega)^2}$$

or
$$\nu_2 = 1430 \cdot \frac{1,5 \cdot 10^{10}}{16 \cdot 10^9 - (5,0,968 - 4,4)^2}$$

or
$$\nu_2 = 1340,62499998377843750019$$

Now it is taken, $u_2 = u_1 + \nu_2$, $\Rightarrow u_2 = 9680 + 1340,62499998377843750019$
 $\Rightarrow u_2 = 11020,62499998377843750019$, and so on.

5. Explanation- Conclusions

The existence of the low frequency waves into the argon magnetized plasma was observed in our early experiments at the Plasma Laboratory of Demokritos. A satisfactory explanation about it was given as well [12,14]. In previous publication the possibility for development of the low frequency waves has been presented. Two kinds of these waves have been identified already [12, 14]. The cylindrical symmetry of the plasma column gives them azimuthal propagation, whereas the boundaries cause for standing waves formation. By using the perturbation theory on the two fluids model, the relation,

$$\nu = \frac{E}{B} \cdot \frac{\omega_c^2}{\omega_c^2 + \nu^2 - (ku - \omega)^2}$$

is obtained under the conditions $v \ll u$.

The validity of the above equation is attempted to be proved with the present experiment. So, the value of the perturbed velocity v was found at first experimentally and then by estimation from the above equation. The direct measurement of the perturbed velocity v is impossible to be carried out as it is added on the drift velocity u , resulting in the inability to be distinguished from it. For this reason, the relation $v = \frac{E}{\varepsilon} u$ was used, which requires the measurement of the quantities E , ε and u . As Figs 4 and 5 show, the electric fields E and ε are maximized in the middle of the radius, where the wave is developed, and the ratio $\frac{E}{\varepsilon}$ is very close to the perturbation theory condition. Furthermore, from Table 2 the values of the drift electron velocity are taken. Figure 7 gives the measured values of the perturbed velocity v . Afterwards, the calculated values from the repeating equation are taken. Despite the inevitable inclinations of the measurements, the two results are satisfactory close, and may have the certainty that the suggested calculation method is right. Another significant observation is that, because of the use of the equation as a repeating one, the values of the perturbed velocity are slightly affected from the drift velocity enlargement. On the contrary, the drift velocity enlargement strengthens the function condition $v \ll u$.

Appendix

The momentum equation on the two fluids theory based on a non-local slab is written as,

$$N_{\alpha} m_{\alpha} \left[\frac{\partial}{\partial t} + \vec{V}_{\alpha} \cdot \vec{\nabla} \right] \vec{V}_{\alpha} = N_{\alpha} q_{\alpha} (\vec{\varepsilon} + \vec{E}) + N_{\alpha} q_{\alpha} \frac{\vec{V}_{\alpha} \times \vec{B}}{c} - N_{\alpha} m_{\alpha} \nu \vec{V}_{\alpha} - \vec{\nabla} p$$

where the indicator α is given for both kinds of the charged particles, electrons and ions. In the following elaboration, the α is omitted for simplicity and the momentum equation for either electrons and ions becomes,

$$N m \left[\frac{\partial}{\partial t} + \vec{V} \cdot \vec{\nabla} \right] \vec{V} = N q (\vec{\varepsilon} + \vec{E}) + N q \frac{\vec{V} \times \vec{B}}{c} - N m \nu \vec{V} - \vec{\nabla} p \quad (\text{A.1})$$

where $N = n_0 + n(\vec{r}, t)$, $\vec{E}_{tot} = \vec{\varepsilon} + \vec{E}(\vec{r}, t)$, and $\vec{V} = \vec{u}_0 + \vec{v}(\vec{r}, t)$, and $n(\vec{r}, t)$, $\vec{E}(\vec{r}, t)$, and $\vec{v}(\vec{r}, t)$, the perturbed qualities with harmonic influence $\propto e^{j(\vec{k}\vec{r} - \omega t)}$.

When no perturbation exists, the drift velocity u_0 , is obtained;

$$0 = n_0 q \vec{\varepsilon} + n_0 q \frac{\vec{u}_0 x \vec{B}}{c} - n_0 m v \vec{u}_0 \quad (\text{A. 2})$$

With the separation on the \vec{r} and θ axis the drift components are given,

$$u_\theta = \frac{q\varepsilon}{m} \cdot \frac{\omega_c}{\omega_c^2 + \nu^2} \quad \text{and} \quad u_r = \frac{q\varepsilon}{m} \cdot \frac{\nu}{\omega_c^2 + \nu^2} \quad (\text{A. 3})$$

3)

(drift velocities are represented by the 0-order equation).

i) If the perturbation is taken into account, eq.(A. 1) gives,

a)

$$n_0 \frac{\partial}{\partial t} + n_0 \vec{u}_0 \cdot \vec{\nabla} \vec{v} = n_0 \frac{q\vec{E}}{m} + n \frac{q\vec{\varepsilon}}{m} + nq \frac{\vec{u}_0 x \vec{B}}{mc} + n_0 q \frac{\vec{v} x \vec{B}}{mc} - n v \vec{u}_0 - n_0 v \vec{v}$$

(A. 4)

(the 1st order equation)

$$\beta) \quad n_0 \vec{v} \cdot \vec{\nabla} \vec{v} + n \frac{\partial \vec{v}}{\partial t} + n \vec{u}_0 \cdot \vec{\nabla} \vec{v} = \frac{nq\vec{E}}{m} + nq \frac{\vec{v} x \vec{B}}{mc} - n v \vec{v} - \frac{\vec{\nabla} p}{m} \quad (\text{A. 5})$$

5)

(the 2nd order equation)

γ) And finally,

$$n \vec{v} \cdot \vec{\nabla} \vec{v} \cong 0 \quad (\text{A. 6})$$

(the 3rd order equation).

From the equilibrium state (zero order equation), the drift velocity components are easily obtained,

$$u_\theta = \frac{q\varepsilon}{m} \cdot \frac{\omega_c}{\omega_c^2 + \nu^2} = \frac{\varepsilon}{B} \cdot \frac{\omega_c^2}{\omega_c^2 + \nu^2} \quad \text{and} \quad u_r = \frac{q\varepsilon}{m} \cdot \frac{\nu}{\omega_c^2 + \nu^2} = \frac{\varepsilon}{B} \cdot \frac{\omega_c \nu}{\omega_c^2 + \nu^2}$$

From the first order equation, the perturbent velocity components may be given as,

$$v_\theta = \frac{qE}{m} \cdot \frac{\omega_c}{\omega_c^2 + \Pi^2} = \frac{E}{B} \cdot \frac{\omega_c^2}{\omega_c^2 + \Pi^2} \quad \text{and}$$

$$v_r = \frac{qE}{m} \cdot \frac{\Pi}{\omega_c^2 + \Pi^2} = \frac{E}{B} \cdot \frac{\omega_c \Pi}{\omega_c^2 + \Pi^2} \quad (\text{A. 7})$$

with , $\Pi = j(ku - \omega) + \nu$

A combination of drift and perturbed velocities components gives,

$$v_{\theta} = \frac{E}{\varepsilon} \frac{\omega_c^2 + \nu^2}{\omega_c^2 + \Pi^2} u_{\theta} \quad \text{and} \quad v_r = \frac{E}{\varepsilon} \frac{\Pi}{\nu} \frac{\omega_c^2 + \nu^2}{\omega_c^2 + \Pi^2} u_r \quad (\text{A. 8})$$

If it is considered that $ku - \omega \ll \nu$, then it is taken $\Pi \cong \nu$ and the perturbed velocity components (eq.A. 7) become,

$$v_{\theta} = \frac{E}{B} \cdot \frac{\omega_c^2}{\omega_c^2 + \nu^2} \quad \text{and} \quad v_r = \frac{E}{B} \cdot \frac{\omega_c \nu}{\omega_c^2 + \nu^2}$$

as the drift velocity components by replacing the dc electric field ε with the perturbed one E .

If $ku - \omega \ll \nu$, then $\Pi \cong \nu$ is taken likewise and from Eqs (A. 8) the below relations (A. 9) are obtained,

$$v_r = \frac{E}{\varepsilon} u_r \quad \text{and} \quad v_{\theta} = \frac{E}{\varepsilon} u_{\theta} \quad (\text{A. 9})$$

References

1. N.D'Angelo and N. Rynn. Diffusion of a Cold Cesium Plasma across a Magnetic Field, *Phys. Fluids*, vol. 4, no. 2, 275-276, 1961.
2. N.D'Angelo and N. Rynn. Low Frequency Oscillations in Cesium Thermionic Converters, *Phys. Fluids*, vol. 4, no. 8, 1054-1055, 1961.
3. N.D'Angelo and R.W. Motley. Low Frequency Oscillations in a Potassium Plasma, *Phys. Fluids*, vol. 6, no. 3, 422-425, 1963.
4. F.F. Chen. "Universal" Overstability of a Resistive, Inhomogeneous Plasma, *Phys. Fluids*, vol. 8, no.7, 1323-1333, 1965.
5. H. W. Hendel, B. Coppi, F. Perkins and P.A. Politzer. Collisional Effects in Plasmas-Drift-Wave Experiments and Interpretation, *Phys. Rev. Lett.*, vol. 18, no. 12, 439-442, 1967.
6. E.Marden-Marshall, R.F.Ellis and J.E.Walsh. Collisional Drift Instability in a Variable Radial Electric Field, *Plasma Phys.*, vol. 28, no. 9B, 1461-1482, 1986.
7. J. Wesson, *Tokamaks*, 2nd ed. Oxford: Clarendon Press, 1997.
8. L. Spitzer, *Physics of Fully Ionized Gases*, 2nd ed. New York: John Wiley & Sons, 1967.
9. N.Krall and A. Trivelpiece, *Principles of Plasma Physics*, McGraw-Hill Kogakusha, LTD, 1973.
10. M. A. Lieberman and A. J. Lichtenberg, *Principles of Plasma Discharges and Materials Processing*, New York: John Wiley & Sons, 1994.
11. Y. S. Satya and R. K.Kaw. Drift Waves in Turbulent Plasmas, *Phys. Rev. Lett.*, vol. 31, no. 24, 1453-1457, 1973.
12. A. J. Anastassiades, and C.L. Xaplanteris. Drift Wave Instability in the Presence of an RF-Field in a Magnetized Plasma, *J. Phys.Soc. of Jpn*, vol. 52, no. 2, 492-500, 1983.

13. C.L. Xaplanteris. Effect of Low-Frequency Instability on Hall Conductivity in Plasma, *Astrophys. Space Science*, vol. 139, no. 2, 233-242, 1987.
14. C.L. Xaplanteris. Collisional Instability in a Rare Magnetized Plasma: An Experimental Model for Magnetospheric and Space Plasma Study, *J. Plasma Physics*, vol. 75, no. 3, 395-406, 2009.
15. T. Klinger. *Handbook of Chaos Control*, ed. H. G. Schuster, (Wiley VCH, Weinheim, 513-562, 1998.
16. D. Block et al. Synchronization of Drift Waves, *Phys. Rev. E*, vol. 63, no. 5, 056401, 2001.
17. C. L. Xaplanteris and E. Filippaki. Drift Waves' Synchronization by Using an External Signal. The Stabilization of a Chaotic Plasma Turbulence, *Chaos Theory, Modeling Simulation and Applications*, eds. C. H. Skiadas, I. Dimotikalis, 2011.
18. C.L. Xaplanteris et al. Electron Drift Caused by rf Field Gradient Creates Many Plasma Phenomena: An Attempt to Distinguish the Cause and the Effect, *J. Plasma Physics*, vol. 78, no. 2, 165-174, 2012.

Nonlinear Analysis of the Hopfield Network Dynamical States Using Matrix Decomposition Theory

Alexander M. Krot and Ryhor A. Prakapovich

United Institute of Informatics Problems of National Academy of Sciences of Belarus,
Laboratory of Self-Organization System Modeling, Minsk, Belarus
(E-mail: alxkrot@newman.bas-net.by, rprakapovich@robotics.by)

Abstract: Nonlinear analysis of dynamical states based on matrix decomposition theory for the Hopfield's neural network is developed in this paper. A formula for determining the values of approximating vector function increments for any number of network neurons is derived. The procedure of noisy monochrome image restoration using Hopfield's network is simulated here.

Keywords: Hopfield's neural network, Nonlinear dynamical systems, State space, Attractors, Matrix decomposition theory.

1 Introduction

Hopfield's neural networks have been widely used as a simple and intuitive understanding of the associative memory model. This follows from the fact that artificial neural networks (ANNs) have some similar characteristics of the human associative memory, namely: 1) information retrieval is carried out not by means of a memory address supply but through a data measure determining the similarity with the standard pattern; 2) data distribution of the stored patterns are located throughout the memory space; 3) data access to memory space are represented by a dynamical process. Due to the stable states of Hopfield's ANN correspond to local minimum of the Hopfield's energy function, they have well been used to solve various optimization problems [2].

Despite its advantages, the Hopfield's ANNs have several drawbacks. These include a small memory capacity for the stored standard patterns and higher sensitivity to the correlation between the input patterns. For example, in [1] it has been experimentally proved that the memory tends to $0,15N$ where N is a number of neurons in the network. However, in the paper [3] it has been shown that the number of stored patterns can not exceed $N/4\log N$, besides the memory capacity is decreased sharply in case of correlation between the stored reference patterns.

It should be noted that these formulas are not very effective for practical application. For example, it is impossible to determine the input pattern affecting on the behavior of all trained network. In this connection an investigation of dynamical states of Hopfield's ANN is very important problem.



Generally speaking, methods of nonlinear dynamics including calculation of minimal attractor embedding dimension, the Lyapunov characteristic exponents etc. are basic tools for characterizing behavior of complex systems [4], [5], [6]. To quantify more exactly a dynamics of complex system quantitatively more exactly these methods have to take into account higher order nonlinearities. In the papers [7-14] higher order nonlinearities have been described by means of matrix series in state space of complex system. Entirely, decomposition methods of nonlinear operators describing the behavior of system in state space (phase space) are very important for analysis, identification and modeling of nonlinear dynamical systems, especially complex nonlinear dynamical systems [5], [6].

In this context, the purpose of this paper is to study the behavior of the Hopfield network based on the developed in [7-14] nonlinear analysis methods for attractors of complex dynamical systems. This paper investigates the stability of the convergence of retrieval binary vectors processes using the matrix series expansion theory [7-14].

2 Analysis of the Hopfield' ANN Dynamics on the Basis of the Matrix Decomposition Theory

Let us consider the Hopfield ANN as a nonlinear dynamical system consisting of three neurons u_1 , u_2 and u_3 (Figure 1). It is known [1], the dynamics of the Hopfield ANN functioning is given by the following rule:

$$u_i(t+1) = \sum_{l=1, l \neq i}^N w_{i,l} \cdot F(u_l(t)) - T_i, \quad i = \overline{1, N} \quad (1a)$$

where $w_{i,l}$ are elements of synaptic weights matrix $W_{3 \times 3}$, N is the input vector length (in particular, $N = 3$), F is an activation function, T_i is a bias value of the i -th neuron (as a rule, $T_i = 0$). As activation function $F(u_i)$ we choose the hyperbolic tangent.

Let us describe the dynamics of states of each neuron u_i :

$$\dot{u}_i = \sum_{l=1, l \neq i}^N w_{i,l} F(u_l) - u_i - T_i \quad (1b)$$

Let us investigate the dynamics of the state changing for all output neurons in the Hopfield's ANN for $N=3$ in accordance with Figure 1:

$$\begin{cases} \dot{u}_1 = f_1(u_1, u_2, u_3) = w_{12}F(u_2) + w_{13}F(u_3) - u_1; \\ \dot{u}_2 = f_2(u_1, u_2, u_3) = w_{21}F(u_1) + w_{23}F(u_3) - u_2; \\ \dot{u}_3 = f_3(u_1, u_2, u_3) = w_{31}F(u_1) + w_{32}F(u_2) - u_3. \end{cases} \quad (2)$$

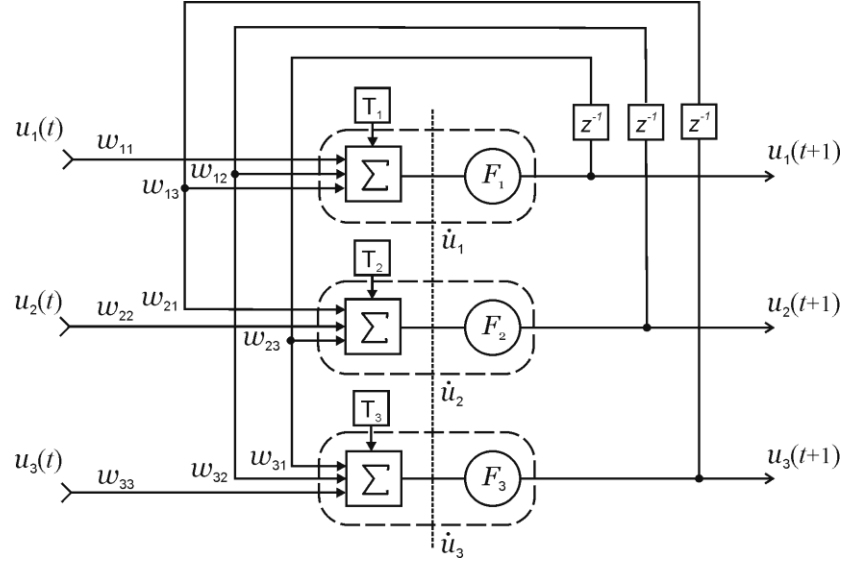


Fig. 1. The Hopfield's neural network architecture

In order to use theory of matrix decomposition [7-14] we represent the system of equations (2) by the following vector functions:

$$\dot{\vec{u}} = \begin{bmatrix} \dot{u}_1 \\ \dot{u}_2 \\ \dot{u}_3 \end{bmatrix} \quad (3a)$$

$$\vec{f}(\vec{u}) = \begin{bmatrix} w_{12}F(u_2) + w_{13}F(u_3) - u_1 \\ w_{21}F(u_1) + w_{23}F(u_3) - u_2 \\ w_{31}F(u_1) + w_{32}F(u_2) - u_3 \end{bmatrix} \quad (3b)$$

According to the nonlinear analysis based on matrix decomposition [7-14] we study the solution of equation (1b) near a specific standard state $\{u_i^*\}$, where $u_i^* = u_i^*(t)$, permanently disturbed by value $v_i = v_i(t)$ of external perturbations or internal fluctuations. In result, instead of u_i^* a new solutions becomes

$$u_i = u_i^* + v_i \quad (4)$$

Taking into account (4) we can find the increment of the vector function in the state space of the Hopfield's ANN (3b) in the form

$$\Delta \vec{f}(\vec{v}, \vec{u}^*) = \vec{f}(\vec{u}^* + \vec{v}) - \vec{f}(\vec{u}^*) =$$

$$= \begin{bmatrix} w_{12} (F(u_2^* + v_2) - F(u_2^*)) + w_{13} (F(u_3^* + v_3) - F(u_3^*)) - v_1 \\ w_{21} (F(u_1^* + v_1) - F(u_1^*)) + w_{23} (F(u_3^* + v_3) - F(u_3^*)) - v_2 \\ w_{31} (F(u_1^* + v_1) - F(u_1^*)) + w_{32} (F(u_2^* + v_2) - F(u_2^*)) - v_3 \end{bmatrix} \quad (5)$$

According to the matrix decomposition theory [7-14] let us represent the increment of the vector function in the space of states by the matrix series expansion:

$$\Delta \vec{f}(\vec{u}^*, \vec{v}) = \vec{f}(\vec{u}^* + \vec{v}) - \vec{f}(\vec{u}^*) = L_{N \times N}^{(1)} \vec{v} + \frac{1}{2!} L_{N \times N^2}^{(2)} (\vec{v} \otimes \vec{v}) + \frac{1}{3!} L_{N \times N^3}^{(3)} (\vec{v} \otimes \vec{v} \otimes \vec{v}) = \sum_{k=1}^{\infty} \frac{1}{k!} L_{N \times N^k}^{(k)} \cdot \vec{v}^{\otimes k}, \quad (6a)$$

$$L_{N \times N^k}^{(k)} = \left(\frac{\partial}{\partial \vec{v}^T} \otimes \left(\frac{\partial}{\partial \vec{v}^T} \otimes \dots \otimes \left(\frac{\partial}{\partial \vec{v}^T} \otimes \vec{f} \right) \dots \right) \right)_{\vec{u}^*}, \quad (6b)$$

where $L_{N \times N^k}^{(k)}$ are matrix kernels of homogeneous nonlinear operators of the

system into the state space; $\vec{v}^{\otimes k} = \overbrace{(\vec{v} \otimes \vec{v} \otimes \dots \otimes \vec{v})}^k$ is k -th Kronecker degree of the vector \vec{v} [7-14].

In particular, the kernels of elements of the first order in accord with (1b) and (4) can be expressed by the following formula:

$$L_{ij}^{(1)} = \left. \frac{\partial f_i}{\partial v_j} \right|_{u_j=u_j^*} = \frac{\partial}{\partial v_j} \left(\sum_{l=1, l \neq i}^3 w_{il} F(u_l) - u_i \right) = \sum_{l=1, l \neq i}^3 w_{il} \left. \frac{\partial F(u_l)}{\partial v_j} \right|_{u_j=u_j^*} - \frac{\partial u_i}{\partial v_j} = w_{il} \frac{\partial F(u_j^*)}{\partial v_j} (1 - \delta_{ij}) - \delta_{ij}, \quad (7a)$$

where δ_{ij} is the Kronecker's delta-symbol. Taking into account (7a) let us write the kernel of the first order in the matrix form:

$$L_{3 \times 3}^{(1)} = \begin{bmatrix} -1 & w_{12} F'(u_2^*) & w_{13} F'(u_3^*) \\ w_{21} F'(u_1^*) & -1 & w_{23} F'(u_3^*) \\ w_{31} F'(u_1^*) & w_{32} F'(u_2^*) & -1 \end{bmatrix}. \quad (7b)$$

Similarly, we find elements of the second order kernel by means of the formula:

$$\begin{aligned} L_{ijk}^{(2)} &= \left. \frac{\partial^2 f_i}{\partial v_j \partial v_k} \right|_{\substack{u_j=u_j^* \\ u_k=u_k^*}} = \frac{\partial^2}{\partial v_j \partial v_k} \left(\sum_{l=1, l \neq i}^3 w_{il} F(u_l) - u_i \right) \Big|_{\substack{u_j=u_j^* \\ u_k=u_k^*}} = \\ &= \frac{\partial}{\partial v_k} \left(\sum_{l=1, l \neq i}^3 w_{il} \frac{\partial F(u_l^*)}{\partial v_j} - \frac{\partial u_i}{\partial v_j} \right) \Big|_{\substack{u_j=u_j^* \\ u_k=u_k^*}} = \\ &= \sum_{l=1, l \neq i}^3 w_{il} \frac{\partial^2 F(u_l^*)}{\partial v_j \partial v_k} = w_{ij} \frac{\partial^2 F(u_j^*)}{\partial^2 v_j} (1 - \delta_{ij}) \cdot \delta_{ik}. \end{aligned} \quad (8a)$$

So, the corresponding matrix for the second order kernel takes the following form:

$$L_{3 \times 9}^{(2)} = \begin{bmatrix} 0 & 0 & 0 & 0 & w_{12}F''(u_2^*) & 0 & 0 & 0 & w_{13}F''(u_3^*) \\ w_{21}F''(u_1^*) & 0 & 0 & 0 & 0 & 0 & 0 & 0 & w_{23}F''(u_3^*) \\ w_{31}F''(u_1^*) & 0 & 0 & 0 & w_{32}F''(u_2^*) & 0 & 0 & 0 & 0 \end{bmatrix} \quad (8b)$$

By analogy with (7b), (8b) we can obtain the matrix form of kernel of the third order:

$$L_{3 \times 27}^{(3)} = \begin{bmatrix} 0 & 0 & 0 & 0 & 0 & 0 & 0 & 0 & 0 & w_{12}F'''(u_2^*) & 0 & 0 & 0 & 0 & 0 & 0 & 0 & 0 & 0 & 0 & w_{13}F'''(u_3^*) \\ w_{21}F'''(u_1^*) & 0 & 0 & 0 & 0 & 0 & 0 & 0 & 0 & 0 & 0 & 0 & 0 & 0 & 0 & 0 & 0 & 0 & 0 & 0 & w_{23}F'''(u_3^*) \\ w_{31}F'''(u_1^*) & 0 & 0 & 0 & 0 & 0 & 0 & 0 & 0 & 0 & w_{32}F'''(u_2^*) & 0 & 0 & 0 & 0 & 0 & 0 & 0 & 0 & 0 & 0 \end{bmatrix} \quad (9)$$

Restricting number of terms in the matrix series (6a) up to the 3-rd order inclusively, we approximate the increment of the vector function (5) into state space of the Hopfield's ANN:

$$\Delta \vec{f}(\vec{v}, \vec{u}^*) \approx L_{3 \times 3}^{(1)}(\vec{u}^*)\vec{v} + \frac{1}{2!}L_{3 \times 9}^{(2)}(\vec{u}^*) \cdot (\vec{v} \otimes \vec{v}) + \frac{1}{3!}L_{3 \times 27}^{(3)}(\vec{u}^*) \cdot (\vec{v} \otimes \vec{v} \otimes \vec{v}). \quad (10)$$

To estimate the accuracy of the approximation, let us we find the following three terms of the matrix series in analytical form:

$$\begin{aligned} L_{3 \times 3}^{(1)}(\vec{u}^*)\vec{v} &= \\ &= \begin{bmatrix} -1 & w_{12}F'(u_2^*) & w_{13}F'(u_3^*) \\ w_{21}F'(u_1^*) & -1 & w_{23}F'(u_3^*) \\ w_{31}F'(u_1^*) & w_{32}F'(u_2^*) & -1 \end{bmatrix} \begin{bmatrix} v_1 \\ v_2 \\ v_3 \end{bmatrix} = \\ &= \begin{bmatrix} w_{12}F'(u_2^*) \cdot v_2 + w_{13}F'(u_3^*) \cdot v_3 - v_1 \\ w_{21}F'(u_1^*) \cdot v_1 + w_{23}F'(u_3^*) \cdot v_3 - v_2 \\ w_{31}F'(u_1^*) \cdot v_1 + w_{32}F'(u_2^*) \cdot v_2 - v_3 \end{bmatrix}. \end{aligned} \quad (11a)$$

$$\begin{aligned} L_{3 \times 9}^{(2)}(\vec{u}^*) \cdot (\vec{v} \otimes \vec{v}) &= \\ &= \begin{bmatrix} 0 & 0 & 0 & 0 & w_{12}F''(u_2^*) & 0 & 0 & 0 & w_{13}F''(u_3^*) \\ w_{21}F''(u_1^*) & 0 & 0 & 0 & 0 & 0 & 0 & 0 & w_{23}F''(u_3^*) \\ w_{31}F''(u_1^*) & 0 & 0 & 0 & w_{32}F''(u_2^*) & 0 & 0 & 0 & 0 \end{bmatrix} \begin{bmatrix} v_1^2 \\ v_1v_2 \\ v_1v_3 \\ v_2v_1 \\ v_2^2 \\ v_2v_3 \\ v_3v_1 \\ v_3v_2 \\ v_3^2 \end{bmatrix} = \\ &= \begin{bmatrix} w_{12}F''(u_2^*) \cdot v_2^2 + w_{13}F''(u_3^*) \cdot v_3^2 \\ w_{21}F''(u_1^*) \cdot v_1^2 + w_{23}F''(u_3^*) \cdot v_3^2 \\ w_{31}F''(u_1^*) \cdot v_1^2 + w_{32}F''(u_2^*) \cdot v_2^2 \end{bmatrix} \end{aligned} \quad (11b)$$

$$L_{3 \times 27}^{(3)}(\vec{u}^*) \cdot (\vec{v} \otimes \vec{v} \otimes \vec{v}) =$$

$$\begin{aligned}
&= \begin{bmatrix} 0 & 00 & 000 & 000 & 000 & 0 & w_{12}F'''(u_2^*) & 0 & 000 & 000 & 000 & 00 & w_{13}F'''(u_3^*) \\ w_{21}F'''(u_1^*) & 00 & 000 & 000 & 000 & 0 & 0 & 0 & 000 & 000 & 000 & 00 & w_{23}F'''(u_3^*) \\ w_{31}F'''(u_1^*) & 00 & 000 & 000 & 000 & 0 & w_{32}F'''(u_2^*) & 0 & 000 & 000 & 000 & 00 & 0 \end{bmatrix} \begin{bmatrix} v_1^3 \\ v_1v_1v_2 \\ v_1v_1v_3 \\ v_1v_2v_1 \\ v_1v_2^2 \\ v_1v_2^2 \\ v_1v_2v_3 \\ v_1v_3v_1 \\ v_1v_3v_2 \\ v_1v_3^2 \\ v_2v_1^2 \\ v_2v_1v_2 \\ v_2v_1v_3 \\ v_2v_2v_1 \\ v_2^2 \\ v_2v_2v_3 \\ v_2v_3v_1 \\ v_2v_3v_2 \\ v_2v_3^2 \\ v_2v_1^2 \\ v_3v_1v_2 \\ v_3v_1v_3 \\ v_3v_2v_1 \\ v_3v_2^2 \\ v_3v_2v_3 \\ v_3v_3v_1 \\ v_3^2v_3v_2 \\ v_3^3 \end{bmatrix} = \\
&= \begin{bmatrix} w_{12}F'''(u_2^*) \cdot v_2^3 + w_{13}F'''(u_3^*) \cdot v_3^3 \\ w_{21}F'''(u_1^*) \cdot v_1^3 + w_{23}F'''(u_3^*) \cdot v_3^3 \\ w_{31}F'''(u_1^*) \cdot v_1^3 + w_{32}F'''(u_2^*) \cdot v_2^3 \end{bmatrix} \quad (11c)
\end{aligned}$$

Substituting (11a)–(11c) in (10) we find an approximating function $\bar{g}_M(\vec{v}, \vec{u}^*)$ for $\Delta \vec{f}(\vec{v}, \vec{u}^*)$ as a vector sum of three terms of this matrix series ($M = 3$):

$$\begin{aligned}
\Delta \vec{f}(\vec{v}, \vec{u}^*) &\approx \bar{g}_3(\vec{v}, \vec{u}^*) = \\
&= \begin{bmatrix} w_{12}F'(u_2^*)v_2 + w_{13}F'(u_3^*)v_3 - v_1 \\ w_{21}F'(u_1^*)v_1 + w_{23}F'(u_3^*)v_3 - v_2 \\ w_{31}F'(u_1^*)v_1 + w_{32}F'(u_2^*)v_2 - v_3 \end{bmatrix} + \frac{1}{2!} \begin{bmatrix} w_{12}F''(u_2^*)v_2^2 + w_{13}F''(u_3^*)v_3^2 \\ w_{21}F''(u_1^*)v_1^2 + w_{23}F''(u_3^*)v_3^2 \\ w_{31}F''(u_1^*)v_1^2 + w_{32}F''(u_2^*)v_2^2 \end{bmatrix} + \\
&\quad + \frac{1}{3!} \begin{bmatrix} w_{12}F'''(u_2^*)v_2^3 + w_{13}F'''(u_3^*)v_3^3 \\ w_{21}F'''(u_1^*)v_1^3 + w_{23}F'''(u_3^*)v_3^3 \\ w_{31}F'''(u_1^*)v_1^3 + w_{32}F'''(u_2^*)v_2^3 \end{bmatrix} = \\
&= \begin{bmatrix} -v_1 + w_{12} \left(F'(u_2^*)v_2 + \frac{1}{2}F''(u_2^*)v_2^2 + \frac{1}{6}F'''(u_2^*)v_2^3 \right) + w_{13} \left(F'(u_3^*)v_3 + \frac{1}{2}F''(u_3^*)v_3^2 + \frac{1}{6}F'''(u_3^*)v_3^3 \right) \\ -v_2 + w_{21} \left(F'(u_1^*)v_1 + \frac{1}{2}F''(u_1^*)v_1^2 + \frac{1}{6}F'''(u_1^*)v_1^3 \right) + w_{23} \left(F'(u_3^*)v_3 + \frac{1}{2}F''(u_3^*)v_3^2 + \frac{1}{6}F'''(u_3^*)v_3^3 \right) \\ -v_3 + w_{31} \left(F'(u_1^*)v_1 + \frac{1}{2}F''(u_1^*)v_1^2 + \frac{1}{6}F'''(u_1^*)v_1^3 \right) + w_{32} \left(F'(u_2^*)v_2 + \frac{1}{2}F''(u_2^*)v_2^2 + \frac{1}{6}F'''(u_2^*)v_2^3 \right) \end{bmatrix} \quad (12)
\end{aligned}$$

To determine the vector function of an approximation error $\vec{\varepsilon}_M(\vec{v}, \vec{u}^*)$, i.e. the so-called residual vector, we find the difference between the right-hand sides of equations (5) and (12) for $M = 3$:

$$\begin{aligned} \vec{\varepsilon}_M(\vec{v}, \vec{u}^*) &= \Delta \vec{f}(\vec{v}, \vec{u}^*) - \vec{g}_M(\vec{v}, \vec{u}^*) = \\ &= \begin{bmatrix} w_{12} \left(F(u_2^* + v_2) - F(u_2^*) - F'(u_2^*)v_2 - \frac{F''(u_2^*)v_2^2}{2} - \frac{F'''(u_2^*)v_2^3}{6} \right) \\ w_{21} \left(F(u_1^* + v_1) - F(u_1^*) - F'(u_1^*)v_1 - \frac{F''(u_1^*)v_1^2}{2} - \frac{F'''(u_1^*)v_1^3}{6} \right) \\ w_{31} \left(F(u_1^* + v_1) - F(u_1^*) - F'(u_1^*)v_1 - \frac{F''(u_1^*)v_1^2}{2} - \frac{F'''(u_1^*)v_1^3}{6} \right) \end{bmatrix} + \\ &+ \begin{bmatrix} w_{13} \left(F(u_3^* + v_3) - F(u_3^*) - F'(u_3^*)v_3 - \frac{F''(u_3^*)v_3^2}{2} - \frac{F'''(u_3^*)v_3^3}{6} \right) \\ w_{23} \left(F(u_3^* + v_3) - F(u_3^*) - F'(u_3^*)v_3 - \frac{F''(u_3^*)v_3^2}{2} - \frac{F'''(u_3^*)v_3^3}{6} \right) \\ w_{32} \left(F(u_2^* + v_2) - F(u_2^*) - F'(u_2^*)v_2 - \frac{F''(u_2^*)v_2^2}{2} - \frac{F'''(u_2^*)v_2^3}{6} \right) \end{bmatrix} \end{aligned} \quad (13)$$

Further we estimate the approximation error δ_M of vector function (5) in the state space of Hopfield's ANN based on a length of vector discrepancy $\vec{\varepsilon}_M(\vec{v}, \vec{u}^*)$:

$$\delta_M = \frac{\|\vec{\varepsilon}_M(\vec{v}_N, \vec{u}_N^*)\|}{\sqrt{N}} \cdot 100\% . \quad (14)$$

Then in the case of $M = 3$, the residual vector δ_3 is equal to

$$\delta_3 = \frac{1}{\sqrt{3}} \sqrt{\vec{\varepsilon}_1^2(\vec{u}_2^*, \vec{u}_3^*, \vec{v}_2, \vec{v}_3) + \vec{\varepsilon}_2^2(\vec{u}_1^*, \vec{u}_3^*, \vec{v}_1, \vec{v}_3) + \vec{\varepsilon}_3^2(\vec{u}_1^*, \vec{u}_2^*, \vec{v}_1, \vec{v}_2)} \cdot 100\% .$$

Before calculating (13) and (14) should be noted that

$$\begin{aligned} F(u_l) &= \tanh(u_l) = \frac{e^{u_l} - e^{-u_l}}{e^{u_l} + e^{-u_l}}; \\ F'(u_l) &= \frac{1}{\cosh^2(u_l)} = \frac{4}{(e^{u_l} + e^{-u_l})^2}; \\ F''(u_l) &= -\frac{2}{\cosh^2(u_l)} \tanh(u_l) = -8 \frac{(e^{u_l} - e^{-u_l})}{(e^{u_l} + e^{-u_l})^3}; \\ F'''(u_l) &= -\frac{2}{\cosh^4(u_l)} + \frac{4}{\cosh^2(u_l)} \tanh^2(u_l) = -\frac{32 + 16(e^{u_l} - e^{-u_l})^2}{(e^{u_l} + e^{-u_l})^4}, \end{aligned}$$

where the values u_l are chosen equal to -1 , 0 or $+1$. Then it follows directly that

$$\begin{aligned} F(x) &= \begin{cases} -0.7616 & \text{if } u_l = -1; \\ 0.0 & \text{if } u_l = 0; \\ 0.7616 & \text{if } u_l = 1. \end{cases} \\ F'(x) &= \begin{cases} 0.4200 & \text{if } u_l = -1; \\ 1.00 & \text{if } u_l = 0; \\ 0.4200 & \text{if } u_l = 1. \end{cases} \\ F''(x) &= \begin{cases} 0.6397 & \text{if } u_l = -1; \\ 0.00 & \text{if } u_l = 0; \\ -0.6397 & \text{if } u_l = 1. \end{cases} \\ F'''(x) &= \begin{cases} 0.0618 & \text{if } u_l = -1; \\ -2.00 & \text{if } u_l = 0; \\ -0.7673 & \text{if } u_l = 1. \end{cases} \end{aligned}$$

One can see from (12) that in general form the elements of a vector approximating functions $\vec{g}_M(\vec{v}, \vec{u}^*)$ can be described as follows:

$$g_M^i(v_j, u_j^*) = -v_i + \sum_{j=1, j \neq i}^N w_{i,j} \sum_{k=1}^M \frac{1}{k!} F^{(k)}(u_j^*) v_j^k, \quad (15)$$

where $F^{(k)}(u_j^*)$ denotes the k -th derivative of the activation function $F(u_j)$ calculated at the point \vec{u}_j^* , N is a number of neurons in the input layer and M is a number of kernels of the matrix series (6a).

Thus, owing to (12) and (15) it has become possible to calculate the increment of the vector function $\Delta \vec{f}(\vec{v}, \vec{u}^*)$ in the state space of the Hopfield's ANN under condition of input vector of arbitrary length N with accuracy to M -th kernel.

To obtain the residual vector $\vec{\varepsilon}_M(\vec{v}, \vec{u}^*)$ and the error value δ_M let us simulate the Hopfield's ANN.

3 A Computational Experiment to Determine the Approximation Error for Binary Patterns

As an example, let us consider the process of restoration of binary vector $\mathbf{a} = [1 \ 1 \ 1]^T$ using the Hopfield's ANN (Figure 1). To this end, we use the Hebb's learning rule [1] to calculate the weight matrix $\mathbf{W}_{3 \times 3}$. In general, the formation of the weight matrix is carried out by means of the Hebb's learning rule [1], [2]:

$$\mathbf{W}_{N \times N} = \frac{1}{N} \sum_{i=1}^p (\mathbf{a}'_i \otimes \mathbf{a}'_i - \mathbf{E}_{N \times N}), \quad (16)$$

where $W_{N \times N}$ is a weight matrix with size of $N \times N$, besides N is a length of the input vector, p is a number of trained pairs of vectors, $E_{N \times N}$ is a diagonal identity matrix with size of $N \times N$. The operation $\mathbf{a}'_i = (2\mathbf{a}_i - 1)$ is performed to convert the binary vectors \mathbf{a}_i in the bipolar form, i.e. to find $\mathbf{a}' = [1 \ 1 \ 1]^T$. For the considered case $N=3$ and $p=1$, we obtain that

$$W_{3 \times 3} = \frac{1}{3} \left(\begin{bmatrix} 1 \\ 1 \\ 1 \end{bmatrix} \begin{bmatrix} 1 & 1 & 1 \end{bmatrix} - \begin{bmatrix} 1 & 0 & 0 \\ 0 & 1 & 0 \\ 0 & 0 & 1 \end{bmatrix} \right) = \frac{1}{3} \begin{bmatrix} 0 & 1 & 1 \\ 1 & 0 & 1 \\ 1 & 1 & 0 \end{bmatrix}, \quad (17)$$

i.e. weight matrix element values are calculated as follows: $w_{12} = w_{13} = 1/3$, $w_{21} = w_{23} = 1/3$, $w_{31} = w_{32} = 1/3$, a $w_{11} = w_{22} = w_{33} = 0$.

Considering the obtained element values w_{ij} of the weights matrix $W_{3 \times 3}$ accord with (17), we rewrite the system (2) as follows:

$$\begin{cases} \dot{u}_1 = \frac{1}{3}(F(u_2) + F(u_3)) - u_1; \\ \dot{u}_2 = \frac{1}{3}(F(u_1) + F(u_3)) - u_2; \\ \dot{u}_3 = \frac{1}{3}(F(u_1) + F(u_2)) - u_3. \end{cases} \quad (18)$$

According to the above mentioned statements of the matrix decomposition theory (3a) – (12) with respect to a Hopfield's ANN, an external disturbance vector is interpreted as a disturbance vector \vec{v} distorting the standard vector \vec{u}^* . In other words, according to formula (4) let us assume that the vector \vec{v} is the disturbance from behind the input vector \vec{u} differs from the reference vector \vec{u}^* , i.e. $\vec{u} - \vec{u}^* = \vec{v}$.

Thus, the elements of the vector \vec{v} belong to the set «-1», «0» and «+1» that defines the following: if $v_i = 0$ then $u_i = u_i^*$, i.e. the test vector elements completely coincide with elements of the standard vector; if $v_i = \pm 1$ then $u_i \neq u_i^*$. Consequently, the vector magnitude \vec{v} can be estimated on the basis of the Hamming' distance $d(\vec{u}, \vec{u}^*)$ between vectors \vec{u} and \vec{u}^* , i.e. by the number of positions in which these vectors are different. In other words, the Hamming distance $d(\vec{u}, \vec{u}^*)$ is the norm of vector \vec{v} :

$$d(\vec{u}, \vec{u}^*) = \|\vec{v}\| = \sum_{i=1}^N |v_i|, \quad (19)$$

where $d(\vec{u}, \vec{u}^*)$ is the Hamming distance and N is a length of the vector \vec{v} .

A computational simulation of the Hopfield' ANN permits to determine the numerical values of the vector $\vec{\varepsilon}_M$ components of the approximation error. The data of computational simulation are presented in the Table 1 which displays the approximation error δ_M of vector function in the state space of the Hopfield's ANN on the basis of the theory of matrix decomposition and computer modeling.

The fifth column of this Table 1 shows the kernels number M used for function approximation. As can be seen from the Table 1, the maximum error occurs in the case of linear approximation ($M=1$) and matches to 9.3% (in the first example), and the minimum error occurs under taking into account the nonlinear terms of higher order in equation (6a), besides it is equal to 1.05% (see the second example). The first 5 kernels have been used in the simulation only. However, the values δ_M of the approximation error for the first pair of vectors \vec{u}^* and \vec{v} lead to an assumption about periodic behavior.

At the same time, a series of experiments estimating the residual vector $\vec{\varepsilon}_M$ and the approximation error δ_M have been carried with an activation function as the sigmoidal function $F(u_i) = 1/(1 + e^{-l})$. As a result, the values $\vec{\varepsilon}_M$ and δ_M are found slightly higher but the behavior error is remained the same.

Table 1. Calculation of the approximation error in computational experiments with Hopfield's ANN

No	\vec{u}	\vec{u}^*	\vec{v}	M	Theoretical estimation $\Delta\vec{f}$	Computational estimation $\Delta\vec{f}$	$\vec{\varepsilon}_M$	δ_M , %
1	2	3	4	5	6	7	8	9
1	$\begin{bmatrix} 1 \\ 0 \\ 1 \end{bmatrix}$	$\begin{bmatrix} 1 \\ 1 \\ 1 \end{bmatrix}$	$\begin{bmatrix} 0 \\ -1 \\ 0 \end{bmatrix}$	1	$\begin{bmatrix} -0.1400 \\ 1.0 \\ -0.1400 \end{bmatrix}$	$\begin{bmatrix} -0.2539 \\ 1.0 \\ -0.2539 \end{bmatrix}$	$\begin{bmatrix} -0.1139 \\ 0.0 \\ -0.1139 \end{bmatrix}$	9,30
2				2	$\begin{bmatrix} -0.2466 \\ 1.0 \\ -0.2466 \end{bmatrix}$		$\begin{bmatrix} -0.0073 \\ 0.0 \\ -0.0073 \end{bmatrix}$	0,60
3				3	$\begin{bmatrix} -0.2040 \\ 1.0 \\ -0.2040 \end{bmatrix}$		$\begin{bmatrix} -0.0499 \\ 0.0 \\ -0.0499 \end{bmatrix}$	4,07
4				4	$\begin{bmatrix} -0.1947 \\ 1.0 \\ -0.1947 \end{bmatrix}$		$\begin{bmatrix} -0.0591 \\ 0.0 \\ -0.0591 \end{bmatrix}$	4,83
5				5	$\begin{bmatrix} -0.1793 \\ 1.0 \\ -0.1793 \end{bmatrix}$		$\begin{bmatrix} -0.0746 \\ 0.0 \\ -0.0746 \end{bmatrix}$	6,09

Table 1 (continuation)

1	2	3	4	5	6	7	8	9
6				1	$\begin{bmatrix} -0.3333 \\ -0.3333 \\ -1.0 \end{bmatrix}$		$\begin{bmatrix} -0.0795 \\ -0.0795 \\ 0.0 \end{bmatrix}$	6,49
7				2	$\begin{bmatrix} -0.3333 \\ -0.3333 \\ -1.0 \end{bmatrix}$		$\begin{bmatrix} -0.0795 \\ -0.0795 \\ 0.0 \end{bmatrix}$	6,49
8	$\begin{bmatrix} 1 \\ 1 \\ 1 \end{bmatrix}$	$\begin{bmatrix} 1 \\ 1 \\ 0 \end{bmatrix}$	$\begin{bmatrix} 0 \\ 0 \\ 1 \end{bmatrix}$	3	$\begin{bmatrix} -0.2222 \\ -0.2222 \\ -1.0 \end{bmatrix}$	$\begin{bmatrix} -0.2539 \\ -0.2539 \\ -1.0 \end{bmatrix}$	$\begin{bmatrix} -0.0316 \\ -0.0316 \\ 0.0 \end{bmatrix}$	2,58
9				4	$\begin{bmatrix} -0.2222 \\ -0.2222 \\ -1.0 \end{bmatrix}$		$\begin{bmatrix} -0.0316 \\ -0.0316 \\ 0.0 \end{bmatrix}$	2,58
10				5	$\begin{bmatrix} -0.2667 \\ -0.2667 \\ -1.0 \end{bmatrix}$		$\begin{bmatrix} 0.0128 \\ 0.0128 \\ 0.0 \end{bmatrix}$	1,05

4 Computer Simulation of Stages of the Hopfield's ANN functioning

One of the main applications of ANN is the classification and pattern recognition. The task of classification is the reference of the input vector to one of the known classes. A stable functioning of the classifier depends on a measure of similarity of the input vector with the standard one storing in the memory of the classifier. This stability also depends on a level of noise imposed on the input vector when the latter can be still recognized correctly.

The process of patterns retrieving based on the Hopfield's ANN is to suppress the distortions presenting in the input vectors. Due to the known difficulties of the mathematical analysis of complex dynamical behavior of recurrent ANN, the question of the maximal possible level determining has been not enough interpretive in the scientific literature. Therefore, one of purposes of this paper is to develop a method of nonlinear analysis based on matrix decomposition allowing predicting the behavior of the Hopfield's ANN under recognizing the input vectors.

However, the above illustrated example for recording and recovery (with the help of Hopfield's ANN) of binary vector (consisting of 3 elements only) does not allow to fully estimate the benefits of the proposed method. Therefore, let us consider a typical problem of Hopfield's ANN concerning associative restoration of noisy patterns.

For example, Figure 2 shows two noisy images (2*b*) and (2*c*) represented by vectors \vec{u}_1 , \vec{u}_2 , and one distorted image (2*d*) represented by a vector \vec{u}_3 , which have been obtained by applying to the standard image (2*a*) (represented by a vector \vec{u}^*) disturbances in the form of noises (2*e*)–(2*g*) encoded by vectors \vec{v}_1 , \vec{v}_2 and \vec{v}_3 respectively. Two-dimensional vector with size of 32×32 represents different types of monochrome images of the letter "A".

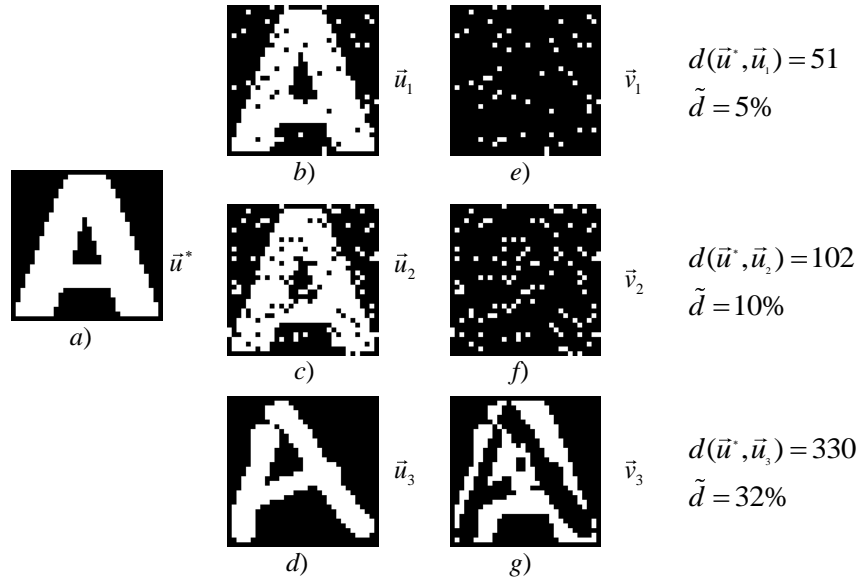


Fig. 2. The process of applying distortion and noise on the standard image

For each pair of vectors, the values of the Hamming distance $d(\vec{u}, \vec{u}_i^*)$ [15] are shown. However, as it follows from this example, the analysis of vectors consisting of a large number of elements ($32 \times 32 = 1024$) is not always convenient to use the specified value. Therefore, we introduce a new value, so-called a relative Hamming distance \tilde{d} , besides its value does not depend on the length of vectors \vec{u} and \vec{u}^* :

$$\tilde{d}(\vec{u}, \vec{u}^*) = \frac{d(\vec{u}, \vec{u}^*)}{N} \cdot 100\% . \quad (20)$$

In this regard, the vector \vec{v} is to be characterized by a variable $\tilde{d}(\vec{u}, \vec{u}^*)$ which is calculated by the ratio of the Hamming distance $d(\vec{u}, \vec{u}_i^*)$ to the value of elements of this vector \vec{v}

Even in the case of presence 32% of distortions the trained Hopfield' ANN is able to qualitatively recover the input image to the standard values. This is achieved due to the fact that one image is recorded by the ANN only. However,

the practical implementation of the Hopfield' ANN shows that an increase in the number of images recorded in the network leads to decreases of the ability of the Hopfield' ANN to restore them, i.e. an image can be restored only in the case of a slight distortion.

Due to (15) it is possible to numerically analyze the influence of the initial distortions in the process of pattern restoring. For example, Figure 3 shows the gradient of the increment of the function describing the dynamics of the Hopfield's ANN consisting of 1024 neurons in which each image represents a two-dimensional monochrome image of the letter "A". The standard vector \vec{u}^* and input vector \vec{u}_3 for these images are illustrated in Figure 2a and 2d, respectively. As one can see from these data, a new vector is characterized by the small perturbations therefore it has properly been restored.

It should be noted that in result of the restoration of pattern, the image parts are presented by black and dark gray colors in Figure 3, i.e. by the values -0.1470 and -0.1464, have been assigned to the object, whereas these shown by light gray and white, i.e. by values -0.0007 and 0.0, have been interpreted as background. Thus, knowing the threshold value, it is possible to determine in advance how the input vector can influence the process of recovery through the ANN.

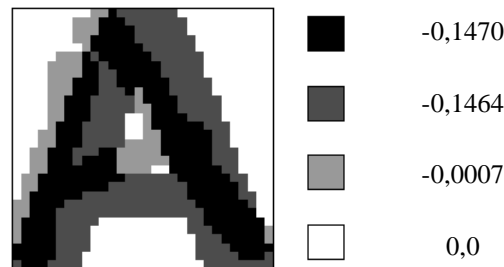


Fig. 3. The gradient values of the function increments

On the other hand, knowing the value of the standard elements of recognizable images, we can estimate based on formula (15) what percentage of the distortions for already trained network can be overcome. In other words, the Hopfield' ANN should consistently apply to the images in which the percentage of distortion increases with each time. Then, analyzing the values g_M^i we can determine the threshold value when the system would no longer be able to adequately restore the image.

4 CONCLUSIONS

In this paper we propose a new approach for the numerical determination of the perturbations of the Hopfield' ANN on the stages of the restoration of previously unknown pattern with usage of the matrix decomposition theory [7-14]. The approximating function g_M^i has been derived besides its accuracy

of restoration depends on the number M of the matrix kernels of homogeneous non-linear operators of the complex dynamical system as the Hopfield's ANN.

References

1. J. Hopfield. Neural networks and physical systems with emergent collective computational abilities, *Proceedings of National Academy of Sciences*, vol. 79, no. 8, 2554–2558, 1982.
2. I.I. Melamed. Neural networks and combinatorial optimization. *Automation and Remote control*, vol. 55, no. 11, 1553–1584, 1994.
3. R.J. McEliece, E.C. Posner, E.R. Rodemich, S.S. Venkatesh. The capacity of the Hopfield associative memory, *IEEE Transactions on Information Theory*, vol. 33, no 4, 461–482, 1987.
4. E.N. Lorenz. Deterministic nonperiodic flow, *Journal of Atmospheric Sciences*, vol. 20, 130–141, 1963.
5. G. Nicolis, I. Prigogine. Self-organization in nonequilibrium systems: From Dissipative Structures to Order through Fluctuation, John Wiley & Sons, New York etc., 1977.
6. P. Berge, Y. Pomeau and C. Vidal. L'ordre dans le chaos: vers une approach deterministe de la turbulence, Hermann, Paris, 1988.
7. A.M. Krot. The decomposition of vector functions in vector-matrix series into state-space of nonlinear dynamic system. EUSIPCO-2000 : *Proc. X European Signal Processing Conference*, Tampere, Finland, 3: 2453–2456, 2000.
8. A.M. Krot. Chaotic dynamic methods based on decomposition of vector functions in vector-matrix series into state-space. *Proc. 10th Mediterranean Electrotechnical Conference*, Lemesos, Cyprus, 2: 643–646, 2000.
9. A.M. Krot. Matrix decompositions of vector functions and shift operators on the trajectories of a nonlinear dynamical system, *Nonlinear Phenomena in Complex Systems*, vol. 4, no. 2, 106–115, 2001.
10. A.M. Krot. Application of expansion into matrix to analysis of attractors of complex nonlinear dynamical systems. *Proc. 14th IEEE International Conference on Digital Signal Processing*, Santorini, Greece, 959–962, 2002.
11. A.M. Krot, H.B. Minervina. Minimal attractor embedding dimension for discrete dynamic system using state-space method: theoretical ground, *Proc. of the 6th IEEE Int. Conf. on Electronics, Circuits and Systems*, Pafos, Cyprus, 2: 941–944, 1999.
12. A.M. Krot, H.B. Minervina. Minimal attractor embedding estimation based on matrix decomposition for analysis of dynamical systems, *Nonlinear Phenomena in Complex Systems*, vol. 5, no. 2., 161–172, 2002.
13. A.M. Krot. The development of matrix decomposition theory for nonlinear analysis of chaotic attractors of complex systems and signals. *Proc. 16th IEEE International Conference on Digital Signal Processing*, Thira, Santorini, Greece, 2009.
14. A.M. Krot. Bifurcation analysis of attractors of complex systems based on matrix decomposition theory. *Proc. of IEEE Intern. Conference on Industrial Engineering and Management*, Zhengzhou, China, 2011.
15. R.E. Blahut. Fast algorithms for digital signal processing. Addison-Wesley Publ. Co.: Reading etc., 1985.

Bifurcation Analysis of Nociceptive Neurons

Olga E. Dick and Boris V. Krylov

Pavlov Institute of Physiology of Russian Academy of Science, St. Petersburg,
Russia

E-mail: glazov.holo@mail.ioffe.ru

Abstract: As known, modification of specified slow sodium channels ($Na_{v1.8}$) in the membrane of nociceptive neurons is the basis of the pain perception by the human brain. The work is devoted to determination of parameters of the channels most sensitive to perceiving the painful signals. Using the bifurcation analysis of the model system describing the impulse activity of the membrane of mammalian nociceptive neuron we partition the parameter planes into the regions corresponding to stable and unstable periodic solutions. The left boundary of the region corresponds to subcritical Hopf bifurcation and emergence of the rough excitation in the form of large amplitude oscillations. The right boundary relates to supercritical Hopf bifurcation and appearance of the smooth excitation in the form of small large amplitude. Integrating inside the region of stable solutions we obtain the relationship between the parameter and frequency values. Bifurcation parameters such as the effective charge transfer of the activation gating system of the sodium channels and the maximal conductance of the channels play the main role in increasing the frequency and, hence, in transformation of the unpainful stimulus into the painful one. The results explain ionic mechanisms of action of analgesic drugs having high selectivity to $Na_{v1.8}$ channels independently of the primary target of action.

Keywords Hopf bifurcation, Membrane model, Sodium channels, Nociceptive neuron.

1. Introduction

It is known that in response to injury of nervous system nociceptive neurons can become hyper-excitable and generate spontaneous impulse activity of unusual frequency [1]. Perception of painful feeling is connected with activation of peripheral nociceptors recording painful signals and transmitting them by afferent nerve fibers to nociceptive neurons soma of which are in spinal ganglia. Low frequency of nerve impulses carries information about adequate tactile action and rise of the frequency for amplification of signal testifies about possible injury [2]. Slow sodium $Na_{v1.8}$ channels are considered significant in generation of painful feeling since the enhancement of synthesis and functional activity of these channels is related to hyper-excitability of nociceptive neurons and high frequency neurophatic pain [3, 4]. The failure in the synthesis of the channels causes the reduce of neurophatic pain [5]. Modulation of activity of the channels by mediators of inflammation can lead to pathological state such as hyperalgesia (an increase of painful sensitivity) [6]. Hyperalgesia is removed by agents descending impulse activity of $Na_{v1.8}$ channels [7]. That is why these



agents are believed as the analgesic highly selective drugs [2]. The aim of the work is to answer the question: what parameters of the slow sodium $\text{Na}_v1.8$ channels do maximal influence on pain signaling transduction? To answer the question it is necessary 1) to study relations between these parameters, an applied external stimulus and a type of stable solution of the model system describing the impulse activity of the nociceptive neuron; 2) to clarify what parameters do determine the possibility of the nociceptive neuron to generate spontaneously a signal of a painful range frequency?

2. The model

We have used the space-clamped Hodgkin-Huxley type model:

$$\begin{aligned}
 c_m \frac{dE}{dt} &= I - g_{Na} f m^3 h (E - E_{Na}) - g_K n^4 (E - E_K) - \\
 &\quad g_L (E - E_L) - g_{NaS} m_s^3 h_s (E - E_{Na}), \\
 \frac{dm}{dt} &= \alpha_m(E)(1-m) - \beta_m(E)m, \\
 \frac{dh}{dt} &= \alpha_h(E)(1-h) - \beta_h(E)h, \\
 \frac{dn}{dt} &= \alpha_n(E)(1-n) - \beta_n(E)n, \\
 \frac{dm_s}{dt} &= \alpha_{m_s}(E)(1-m_s) - \beta_{m_s}(E)m_s, \\
 \frac{dh_s}{dt} &= \alpha_{h_s}(E)(1-h_s) - \beta_{h_s}(E)h_s,
 \end{aligned} \tag{1}$$

where E is the membrane potential, the variables m , h , n , m_s , h_s represent the probabilities of activation and inactivation of fast sodium, potassium and slow sodium channels, respectively.

The constants $c_m = 20$ pF, $g_{Na} = 40$ nS, $g_K = 20$ nS, $g_L = 5$ nS, $E_{Na} = 55$ mV, $E_K = -85$ mV, $E_L = -70$ mV are the membrane capacitance, the maximal conductance of the fast sodium, potassium and leakage ions channels and the reversal potentials for Na^+ , K^+ and leakage ions.

The voltage-dependent expressions

$$\begin{aligned}
 \alpha_m(E) &= \frac{0.115(1 + e^{(E+70)/10})}{1 + e^{(E+40)/42}}, & \beta_m(E) &= 0.015(1 + e^{(E+25)/8}), \\
 \alpha_h(E) &= 0.012(1 + e^{-(E+43)/10}), & \beta_h(E) &= \frac{1.32}{1 + 0.2e^{(E+10)/7}}, \\
 \alpha_n(E) &= \frac{0.006(E+45)}{1 - e^{-(E+45)/12}}, & \beta_n(E) &= 0.13e^{-(E+45)/30},
 \end{aligned}$$

$$\begin{aligned}\alpha_{m_s}(E) &= e^{k_1(E+G)+d_1}, & \beta_{m_s}(E) &= e^{k_2(E+G)+d_2}, \\ \alpha_{h_s}(E) &= 0.0015e^{-(E+4)/30}, & \beta_{h_s}(E) &= \frac{0.01}{1+0.2e^{-(E+10)/7}}\end{aligned}$$

describe rates of transfer of the activation and inactivation gating structures of ionic channels between the closed and open states.

According to the Boltzmann's principle for the channel with the two-state open-closed structure the ratio of the number of open channels (N_o) to the number of closed channels (N_c) is determined by

$$\frac{N_o}{N_c} = \frac{m_s}{1-m_s} = e^{Z_{eff}\bar{e}(E-\bar{E})/kT},$$

where Z_{eff} is the effective charge of the activation gating structure (in electron units) coupled with conformational change of the gating structure during the ion transfer through the membrane, k is the Boltzmann's constant, T is the absolute temperature, \bar{e} is the electron charge, \bar{E} is the membrane potential such that $N_o=N_c$.

Then at $E=\bar{E}$ for the activation gating structure of the slow sodium channels one can write $\alpha_{m_s} = \beta_{m_s}$, whence it follows that the effective charge value of the activation gating structure can be gained as

$$Z_{eff} = \frac{kT}{\bar{e}}(k_1 + k_2).$$

3. Partition of the model parameter space into regions of qualitatively different solutions

To obtain relationship between the type of stable solution of the system, its parameters and an applied external stimulus it is sufficient to find points belonging to the boundary partitioning the parameter space of the model system into the regions of the qualitatively different types of stable solutions (steady states and stable periodic oscillations). For constructing the boundary the method of bifurcation analysis is applied.

On the I axis there are at least 3 bifurcation points ($I_0 < I_1 < I_2$) [8]. For $I < I_0$ and $I > I_1$ there is a one-to-one correspondence between the type of steady state (unstable or stable) and the presence or absence of a stable periodic solution. For $I \leq I_0$ and $I \geq I_2$ the steady state is stable and a limit cycle does not exist.

While the bifurcation parameter I increases in interval $(I_0 < I \leq I_1)$ the steady state is stable and a stable and unstable periodic solutions coexist appearing via fold limit cycle bifurcation. The unstable periodic solution shrinks down to the rest state and makes it lose stability via subcritical Andronov-Hopf bifurcation.

Therefore, for $I > I_1$ the stable periodic oscillations of large amplitude exist both with decreasing and increasing I value. But for $I_0 < I \leq I_1$ the stable limit cycle of large amplitude is exhibited only with decreasing I .

Since for the Hodgkin-Huxley type system $I_0 \approx I_1$ for all the physiologically possible parameter values [9], the value of I_1 can be used as an approximate value of I_0 . That is why the task of finding the boundary of qualitatively different types of stable solutions can be reduced to the more simple numerical task of constructing the boundary of various steady states (stable and unstable).

We write system (1) in the form

$$\frac{dx}{dt} = F(x, p, I), \quad (2)$$

where $x = (E, m, h, n, m_s, h_s)$ is a vector of the phase coordinates,

$p = (g_{NaS}, k_1, k_2)$ is a vector of parameters which can be considered as bifurcation ones.

The method for determining the boundary points of the region of stable periodic solutions is reduced to the sequence of operations:

1) finding the equilibrium state of system (2) as a unique solution $x_0(p, I)$ of the equation

$$F(x, p, I) = 0,$$

2) calculating the eigenvalues $\{\lambda_i(p, I)\}_1^6$ of the Jacobian matrix

$$J(p, I) = \left(\left. \frac{\partial F_i}{\partial x_j} \right|_{x=x_0(p, I)} \right), \quad i, j = 1, \dots, 6,$$

3) finding the parameter values satisfying the Hopf bifurcation, namely, arising of a pair of purely imaginary eigenvalues

$$\lambda_1 = i\omega, \quad \lambda_2 = -i\omega, \quad \lambda_3 < 0, \quad \lambda_4 < 0, \quad \lambda_5 < 0, \quad \lambda_6 < 0.$$

To determine values $I_1(p)$ and $I_2(p)$ at which maximal real part ($\lambda_m(p, I)$) becomes equal to zero the following algorithm is used.

1) The interval $[I_0, I_K]$ of possible values is discretized with k consecutive subintervals of length Δ .

In the case of existence even though one solution $I_1(p)$ of equation

$$\lambda_m(p, I) = 0,$$

the i - subinterval involving the solution, is determined by the consecutive search beginning from the left side of the interval. The value of this solution is determined by linear interpolation.

2) The value of $I_2(p)$ is calculated in the interval $[i^*\Delta, I_K]$ by the method of bisection followed by linear interpolation.

The numerical solution of system (1) inside the obtained region of stable periodic solutions is found by a fourth-order Runge-Kutta method with a modified variable step size and Gear algorithm. The frequency of the periodic solution is calculated by the time values corresponding to local maxima.

4. Results and discussion

To elucidate the role of slow sodium channels in generation of the painful stimulus the maximal conductance of the slow sodium channels (g_{NaS}), the effective charge transfer of the activation gating system of the channels (Z_{eff}) and the shift (G) of the activation curve along the membrane potential axis have been used as variable parameters.

The family of the plane sections of the boundary partitioning the parameter space (g_{NaS} , Z_{eff} , I) into the regions of stable and unstable steady states are given in Fig.1 a, b.

Inside the each found region the steady state is unstable and there is a stable limit cycle corresponding to stable periodic solution.

Stair-stepping effect of the left boundary of the region is related to features of arising limit cycles on the left and right sides of the boundary. The left boundary of the region corresponds to subcritical Hopf bifurcation and emergence of the rough excitation in the form of large amplitude oscillations. The right boundary relates to supercritical Hopf bifurcation and appearance of the smooth excitation in the form of small large amplitude.

As is seen, if $g_{NaS} = 0$, periodic oscillations are absent at any stimulus value.

The minimal value of g_{NaS} such that the oscillations emerge is equal to 14,9 nS at the stimulus – 142,5 pA and the value grows when Z_{eff} increases.

When the effective charge is less than $5\bar{e}$ the periodic oscillations arise only by hyperpolarizing stimulus ($I < 0$ pA).

With increasing Z_{eff} the steady periodic solutions region extends significantly and shifts in direction of depolarizing stimulus ($I > 0$ pA).

Integrating inside the constructed regions we obtain the relationship between the model parameter and frequency values. The examples of steady periodic solutions are represented in Fig.2 and Fig.3.

The periodic oscillations emerging on the left boundary of the region have large amplitude and small frequency. When moving inside the region from left to right an amplification of the external stimulus tends to change in amplitude and frequency of the nociceptive neuron. In other words, for the constant maximal conductance of the slow sodium channels and effective charge transfer of the activation gating system an enhancement of the external stimulus leads to the increase of the frequency of periodic oscillations and then their disruption.

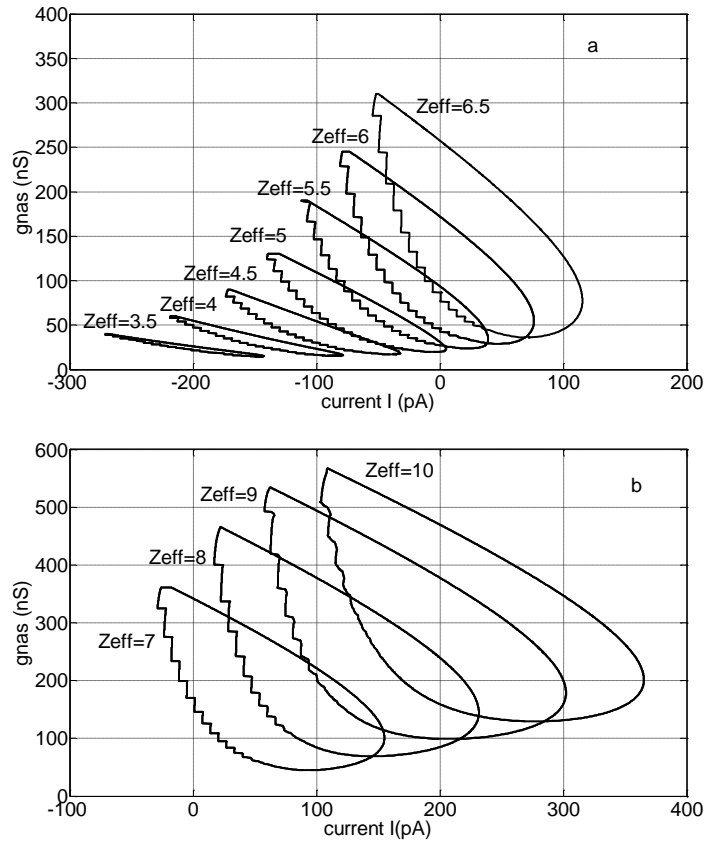


Fig. 1. The examples of the plane sections of the boundary partitioning the parameter space (g_{NaS} , Z_{eff} , I) into the regions of stable and unstable steady states. Each section is constructed with 800 points on the (g_{NaS} , I) plane corresponding to 700 net values of the parameter g_{NaS} . Values $G=10$ mV, $\{Z_{eff}\}_1^{11} = \{3.5\bar{e}, 4\bar{e}, 4.5\bar{e}, 5\bar{e}, 5.5\bar{e}, 6\bar{e}, 6.5\bar{e}, 7\bar{e}, 8\bar{e}, 9\bar{e}, 10\bar{e}\}$.

The periodic oscillations emerging on the left boundary of the region have large amplitude and small frequency. When moving inside the region from left to right an amplification of the external stimulus tends to change in amplitude and frequency of the nociceptive neuron. In other words, for the constant maximal conductance of the slow sodium channels and effective charge transfer of the activation gating system an enhancement of the external stimulus leads to the increase of the frequency of periodic oscillations and then their disruption.

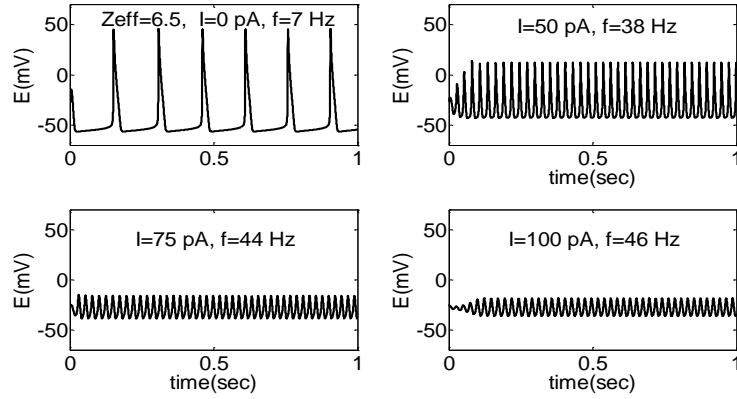


Fig. 2. The examples of steady solutions for $Z_{eff} = 6.5\bar{e}$, $g_{NaS} = 100nS$ and various values of stimulus.

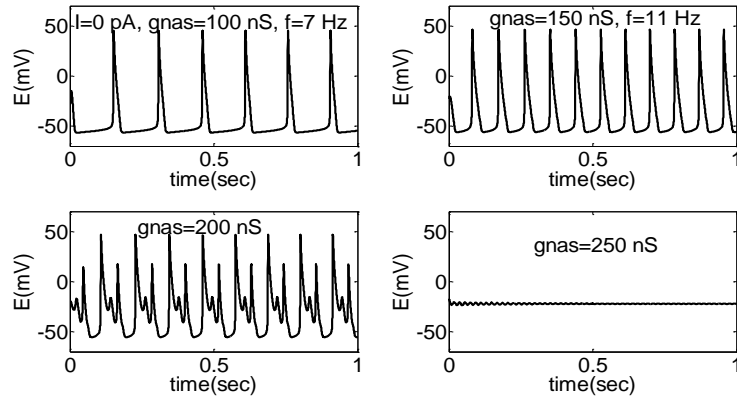


Fig.3. The examples of steady solutions $Z_{eff} = 6.5\bar{e}$, $I = 0$ and different values of g_{NaS} .

The periodic oscillations emerging on the left boundary of the region have large amplitude and small frequency. When moving inside the region from left to right an amplification of the external stimulus tends to change in amplitude and frequency of the nociceptive neuron. In other words, for the constant maximal conductance of the slow sodium channels and effective charge transfer of the activation gating system an enhancement of the external stimulus leads to the increase of the frequency of periodic oscillations and then their disruption. When moving inside the region from bottom to top a growth of the maximal conductance of the slow sodium channels for the constant stimulus value results in increase of the frequency, period doubling and also failure of periodic oscillations (Fig.3).

Thus, both factors, namely, decrease of effective charge transfer of the activation gating system of the slow sodium channels for the constant maximal conductance of the channels and decrease of the maximal conductance of the slow sodium channels for the constant stimulus decline the frequency of impulse activity. Since an increase in the frequency of impulse activity of nociceptive neurons is related to the emergence of neuropathic pain, our findings indicate the direction of looking for chemical agents possessing analgesic properties.

3. Conclusion

The form of the constructed regions demonstrates that ability of each parameter to be bifurcation one significantly depends on the other parameter values. Thus, the conclusions about bifurcation properties of the system parameters are determined by the investigated point in the parameter space.

The character of changes in the system solutions and in the frequency of periodic solutions can be used in searching of chemical agents aimed for selective removal of neuropathic pain.

References

1. J.K. Diss, S. P. Fraser, M. B. Diamoz Voltage-gated Na channels: multiplicity of expression, plasticity, functional implications and pathophysiological aspects. *Eur. Biophys. J.* 33: 180-193, 2004.
2. E.A. Karymova, I. E. Katina, V. B. Plakhova, et. al. Possible coding mechanism of nociceptive signals: role of slow sodium channels. *Sensory systems*, 22: 257-270, 2008.
3. A.E. Goldin Evolution of voltage-gated Na channels. *J. Exper. Biol.* 205: 575-584, 2001.
4. J. Lai, F. Porreca, J.C. Hunter, et al. Voltage-gated sodium channels and hyperalgesia. *Ann. Rev. Pharmacol. Toxicol.* 44: 371-397, 2004.
5. S.G. Waxman The molecular pathophysiology of pain: abnormal expression of sodium channel genes and its contributions to hyperexcitability of primary sensory neurons. *Pain Aug. Suppl.* 6: 133-140, 1999.
6. S.G. Waxman, T.R. Cummins, S. D. Dib-Hajj, et.al. Voltage-gated sodium channels and the molecular pathogenesis of pain. *J. Rehabil. Res. Dev.* 37: 517-528, 2000.
7. N. Ogata, Y. Ohishi The molecular diversity of structure and function of the voltage-gated Na channels. *Jpn. J. Pharmacol.* 88: 365-377, 2002.
8. B.Hassard Bifurcation of periodic solutions of the Hodgkin-Huxley model for the squid giant axon. *J. Theor. Biol.* 71: 401-420, 1978.
9. Y.A. Bedrov, G. N. Akoev, O.E. Dick. Partition of the Hodgkin-Huxley type model parameter space into the regions of qualitatively different solutions. *Biol. Cybern.* 66: 413-418, 1992.

Acknowledgements We thank E.A. Karymova for her help with experimental recordings of ionic channels.

Monte Carlo Modelling of Soliton Pulse Timing Jitter in Silicon Nanowire Waveguides

Matthew Marko^{1,2,*}, Xiujian Li^{2,3}, Jiangjun Zheng², Chee Wei Wong²

(1) Navy Air Warfare Center Aircraft Division (NAWCAD), Joint Base McGuire-Dix-Lakehurst, Lakehurst NJ 08733, USA

(2) Optical Nanostructures Laboratory, Columbia University in the City of New York, New York NY 10027, USA

(3) Tech-Physical Research Center, Science College, National University of Defense Technology, Changsha, Hunan 410073, China

E-mail: matthew.marko@navy.mil

Abstract: The purpose of this effort is to study changes in the amplitude noise and timing jitter of an optical pulse chain from a mode-locked laser, as it undergoes soliton propagation through a nonlinear silicon nanowire waveguide. A numerical model was developed using the Non-Linear Schrödinger Equation to model the soliton formation with two-photon absorption. The amplitude noise was modeled as a separate noise envelope, and the phase noise and timing jitter was modeled using Monte-Carlo simulations of jitter-induced phase-shifts. It was observed that while increased pulse energy will result in increased amplitude and phase noise, the presence of two-photon absorption, which attenuates optical nonlinearities in the waveguide, results in a reduction in phase noise at the output of the silicon waveguides.

Keywords: Noise, Phase Noise, Timing Jitter, Monte-Carlo, Non-Linear Schrödinger Equation, Silicon, Photonics, Soliton, Dispersion, Waveguides, Self-Phase Modulation, Kerr, Nonlinear Optics,

1. Introduction

One of the challenges that must be overcome for the practical implementation of optical data transfer is the issue of noise, particularly phase noise, amplitude noise, and timing jitter. Practical optical data communication often requires pulse repetition rates of tens of gigahertz (GHz), and therefore timing jitter on the order of femtoseconds (fs) is often necessary to ensure a low bit-rate error in the data. This paper investigates numerically the effects of soliton pulse propagation within silicon nanowire waveguides, and the effects of these nonlinearities on noise and jitter, for the purpose of applied optical data communications.

Much research has previously been conducted on the effects of optical propagation through a dispersive waveguide on the phase noise, timing jitter, and amplitude noise [1-2]. This research to date has predominantly focused on



optical fibers [3], photonic crystal fibers [4], and mode-locked lasers [5]. The purpose of this paper is to investigate optical soliton propagation [6-8] through silicon nano-waveguides. Silicon waveguides are of interest to the scientific community for their high-nonlinearity and tight optical confinement. Compared to optical fibers, silicon nano-waveguides have much smaller length scales, and offers many applications at the chip-scale level for all-optical data transfer, information manipulation, and computing.

2. Simulations

It has been previously observed that the noise can often be attributed as a separate envelope [2,9] of much weaker intensities than the undisturbed pulse input:

$$A(z,t) = (P_0^{1/2} + a(z,t)) \exp(-j\varphi(z)) \quad a(z,\omega) = \int_{-\infty}^{\infty} a(z,t) \exp(-i\omega t) dt$$

With this assumption, the NLSE can be linearly separated, and a separate NLSE for the noise can be derived:

$$(j/2)\beta_2\omega^2 a + (j/6)\beta_3\omega^3 a + j\gamma P_0 \{a + a^*\} \exp(-\alpha z) = -\partial a / \partial z$$

The noise can be assumed to be an independent envelope propagating through the waveguide, and analyzed as a separate NLSE problem, propagating concurrently with the pulse.

In the time domain, $a(z,t) = a_r(z,t) + j a_i(z,t)$, where $a_r(z,t)$ and $a_i(z,t)$ are real functions. By substituting these terms into the noise-NLS equation, one gets a simple relationship for the real and imaginary components of the noise function in the spectral domain:

$$\begin{aligned} \partial a_r(z,\omega) / \partial z &= \rho * a_i(z,\omega) \\ \partial a_i(z,\omega) / \partial z &= -\{\rho + (2j\gamma P_0 \exp(-\alpha z))\} * a_r(z,\omega) \\ \rho &= (\beta_2\omega^2/2) + (\beta_3\omega^3/6) \end{aligned}$$

Using these assumptions, with a given noise input, one can estimate the change in the power spectral density after optical soliton propagation through a given distance increment of a waveguide [9] by using the following equations:

$$\begin{aligned} \Phi(L,\omega) &= 1/2 \Phi(0,\omega) \exp(-\alpha z) (2|M_{11}(\omega)|^2 + |M_{12}(\omega)|^2 + |M_{21}(\omega)|^2) \\ M_{11}(\omega) &= \cos(\delta(\omega)L) \\ M_{12}(\omega) &= (\rho/\delta) \sin(\delta(\omega)L) \\ M_{21}(\omega) &= -(\delta/\rho) \sin(\delta(\omega)L) \\ \delta &= [\rho^2 + 2\rho\gamma P_0]^{1/2} \end{aligned}$$

Using these terms and incorporating them into the NLSE numerical simulation, an accurate prediction of the changes in the frequency noise after propagation through a silicon waveguide could be obtained.

Many NLSE simulations were conducted in order to complement the experimental silicon waveguide used in this experiment. The silicon waveguide parameters include a length of 4.1 mm, an effective area of 250 nm by 450 nm, a Kerr coefficient of $4.4 \times 10^{-18} \text{ m}^2/\text{W}$, an effective index of 2.5, a group index of 4.5, and a 2nd and 3rd order GVD of 4.5 ps²/m and 0.01 ps³/m, respectively. The model took into account both two-photon absorption (TPA), free-carrier absorption (FCA), and linear loss of the pulse envelope. Because the noise is assumed to be substantially weaker compared to the pulse envelope, only linear loss is applied to the noise envelope.

For the initial simulations, the wavelength was set at 2543 nm, so that there would be no effects of TPA or FCA. Simulations were run repeatedly for various input pulse energies ranging from 1 pJ to 500 pJ; these energies are far in excess of the fundamental soliton energy for the 2.3 ps hyperbolic secant pulse. As the lasers timing jitter was in excess of the pulse duration, the simulation assumed a constant noise envelope for the temporal window analyzed. It was observed that at lower input pulse powers, the noise would decrease after propagation through the waveguide, but this loss would decrease with increasing powers. After an input pulse energy of 250 pJ, it was found that the energy would in fact increase exponentially with increasing energy. This is expected, as previous work in glass photonic crystal fibers [4] has also noticed an increase in jitter from solitons not subjected to TPA.

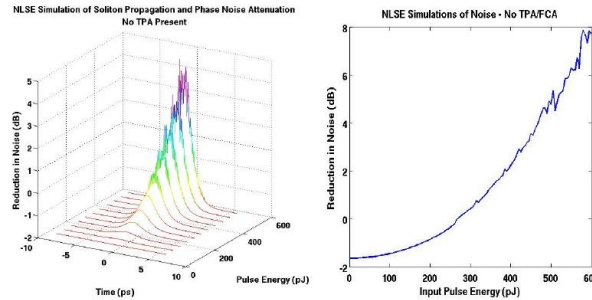


Figure 1 – Results of NLSE simulations of noise after propagation in the silicon waveguide, with a wavelength of 2543 nm that is not subjected to the nonlinear effects of two-photon and free-carrier absorption.

The simulation was then conducted for optical pulses at 1543 nm, which are now subjected to a considerable amount of TPA at this wavelength [10,11]. It was observed numerically that for optical soliton propagation in a silicon waveguide, the noise would consistently be reduced from 1.6 to 1.4 dB; this reduction would decrease with increasing input pulse energies within the waveguide. After 1 nJ of energy, which is far more than will be practically realized experimentally, the noise decrease will plateau, and there will be little change with increasing power.

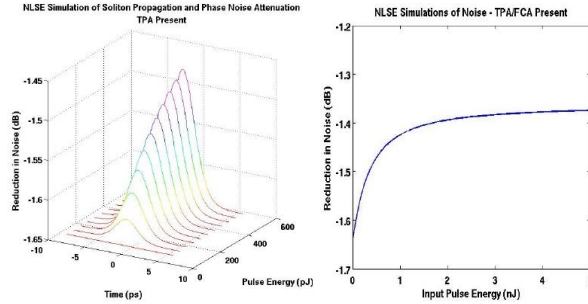


Figure 2 – Results of NLSE simulations of noise after propagation in the silicon waveguide, with a wavelength of 1543 nm that is subjected to the nonlinear effects of two-photon and free-carrier absorption.

3. Monte-Carlo Analysis of Soliton Timing Jitter

One of the challenges of performing a numerical analysis on the effects of optical soliton propagation on phase noise and timing jitter is the fact that such noise can reasonably be assumed to be random jitter. Even though most of this jitter is deterministic and repeatable, the variation of each pulse can still have a significant amount of randomness involved. Therefore, in an effort to numerically model the changes in phase noise after soliton propagation, Monte-Carlo simulations of pulse phase-shifts will be used in conjunction with the Non-Linear Schrödinger Equation (NLSE) solver.

The goal of this solver is to determine the change in timing jitter after propagation through a silicon waveguide for various energies and wavelengths. Input pulse energies from 5 pJ to 5 nJ were studied, and the wavelengths of 1550 nm and 2300 nm were analyzed. At each pulse-energy being studied, the program first solves the NLSE for a transform-limited hyperbolic secant squared pulse with no chirp; the output pulse shape and phase of the NLSE simulation will be used for comparison against a number of random trial simulations of jitter-shifted pulses. Before propagating these pulses, the same hyperbolic secant-squared input pulses are phase-shifted to represent the timing jitter. The phase shift is as follows:

$$\text{Phase Shift} = \exp[i \cdot (2 \cdot f \cdot \text{Jitter}) \cdot ((2 \cdot \text{rand}) - 1)]$$

where f is the frequency of the mode-locked laser (39.11 MHz), Jitter is the RMS of the input timing jitter (this study used 20 ps), and rand is a random number from zero to 1. The code is written so that the phase shift varies up to twice the specified average jitter, and can be either positive or negative.

After applying the random phase shift, the pulse was analyzed with the NLSE solver. The new output pulse phase was compared to the original non-shifted phase, the difference in phase was converted to timing jitter, and the RMS of the jitter was calculated. As Monte-Carlo simulations require many repeated random terms to be statistically significant, the simulation was repeated 1,000 times at each energy level, for a total of over 400,000 separate NLSE simulations. The raw data of the results can be seen in Figure 3, which shows the output timing jitters as a function of input pulse-energy.

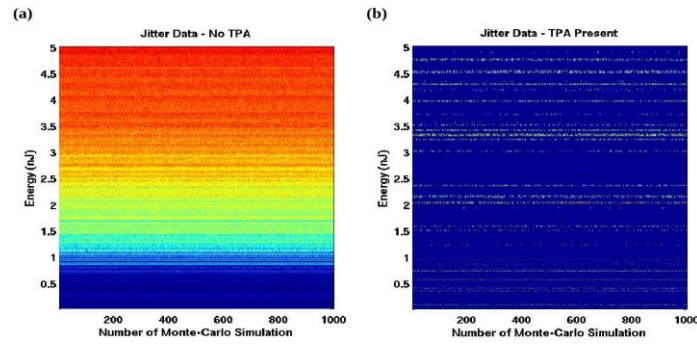


Figure 3 – Raw Data of simulations, (a) $\lambda = 2300$ nm and (b) $\lambda = 1550$ nm.

After all of the simulations were completed, in order to remove any statistical outliers, the code went through and factored out all simulations greater than 2 standard deviations away from the mean jitter. The RMS of this noise was then collected, and a final output timing jitter was given for each energy level. The data of the timing jitter as a function of energy was cleaned up of statistical outliers, and averaged out to obtain the trend of output timing jitter as a function of energy.

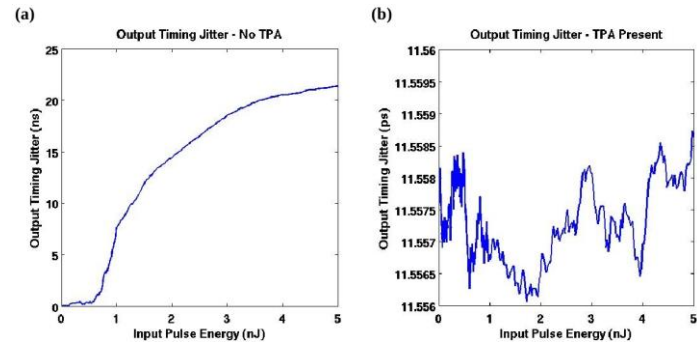


Figure 4 – Output timing jitter as a function of pulse energy, for (a) $\lambda = 2300$ nm and (b) $\lambda = 1550$ nm.

In the study of the 2300 nm pulse without TPA, the simulation clearly demonstrated the timing jitter growing exponentially with increasing pulse energy, just as the NLSE simulation of the separate noise envelope has demonstrated. In the case of the 1550 nm pulse subjected to TPA, the Monte-Carlo simulations showed the output timing jitter to consistently decrease from 20 ps RMS to 11.6 ps of RMS timing jitter. Just as observed with the study of the NLSE of the phase-noise envelope, the presence of TPA has attenuated the jitter, rather than allowed it to develop with increasing energies. It is therefore concluded, based on these two separate simulations, that, soliton propagation in the presence of TPA will result in a decrease in phase noise and timing jitter.

4. Conclusion

The numerical simulations have demonstrated that an optical pulse propagating in the optical C-band within a silicon waveguide will see an attenuation of the amplitude noise and timing jitter due to the presence of the two-photon absorption. The two-photon absorption has the property of attenuating the pulse proportionally to the intensity, which acts to inhibit the self-phase modulation and thus soliton compression. If this attenuation were not present, an increase in intensity will result in an increase in nonlinear effects and thus an increase sensitivity to jitter-induced phase-shifts; for this reason high optical intensities have shown to increase the timing-jitter in the simulations of longer wavelengths not subjected to two-photon absorption. In the presence of two-photon absorption, however, less variation in the pulse phase-shifts can be expected as a result the reduction in two-photon absorption. For this reason, it is concluded that optical soliton propagation in the presence of two-photon absorption has the ability to attenuated the phase noise and timing jitter of a mode-locked optical pulse.

7. Acknowledgements

Sources of funding for this effort include Navy Air Systems Command (NAVAIR)-4.0T Chief Technology Officer Organization as an Independent Laboratory In-House Research (ILIR) Basic Research Project (Nonlinear Analysis of Ultrafast Pulses with Modeling and Simulation and Experimentation); a National Science Foundation (NSF) grant (Ultrafast nonlinearities in chip-scale photonic crystals, Award #1102257), and the Science Mathematics And Research for Transformation (SMART) fellowship. The author's thank James McMillan, Tingyi Gu, Kishore Padmaraju, Noam Ofir, and the laboratory of Keren Bergman for fruitful discussions.

References

1. "Analysis of Timing Jitter for Ultrashort Soliton Communication Systems Using Perturbation Methods." Margardia Facao and Mario Ferreira, Journal of Nonlinear Mathematical Physics, 2001.
2. "Electromagnetic Noise and Quantum Optical Measurements." Hermann Haus. Springer-Verlag Berlin Heidelberg 2000.
3. "Soliton Transmission Control," A Mecozzi, Hermann Haus, et al. Optics Letters, 1 December 1991, Volume 16, Number 3
4. "Supercontinuum generation and soliton timing jitter in SF6 soft glass photonic crystal fibers." Anatoly Efimov and Antoinette Taylor, Optics Express, Volume 16, Number 8. 14 April 2008.
5. "Noise and Stability of Actively Mode-locked Fiber Lasers," PhD thesis by Matthew Edward Grein, Massachusetts Institute of Technology, June 2002.
6. "Nonlinear Fiber Optics," 4th Edition, Govind Agrawal.
7. "Temporal solitons and pulse compression in photonic crystal waveguides," P. Colman, C Husko. Nature Photonics, 21 November 2010. DOI: 10.1038/NPHOTON.2010.261
8. "Fundamentals of Photonics." 2nd Edition. Saleh, Teich.
9. Husko, De Rossi, and Wong, Effect of multi-photon absorption and free carriers on self-phase modulation in slow-light photonic crystals. Optics Letters, Vol. 36, No. 12. June 15, 2011
10. "Modeling nonlinear phase noise in differentially phase-modulated optical communication systems." Leonardo Coelho. Optics Express 3226, 2 March 2009, Volume 17, Number 5.
11. "Introduction to Solid State Physics, 8th Edition." Kittel, Charles. Wiley, 2004.
12. "Characterization of the Noise in Continuously Operating Mode-Locked Lasers," Dietrich Von der Linde. Applied Physics B 39, 201-216 (1986).
13. JitterTime Consulting LLC: <http://www.jittertime.com/articles/pnsheet.shtml>

Shadow Prices and Lyapunov Exponents

Ilknur Kusbeyzi Aybar

Yeditepe University, Istanbul, Turkey
Department of Computer Education and Instructional Technology
E-mail: ikusbeyzi@yeditepe.edu.tr

Abstract: A relation between the optimal solution of the optimization problem and the stability and bifurcation properties of the corresponding dynamical system is suggested in this work. There exists a relation between the optimal solution of an optimization problem and an equilibrium point of a dynamical system. In this sense stability properties, Lyapunov exponents and bifurcations of the resulting dynamical systems can be studied.

Keywords: Dynamical systems, Optimization, Lyapunov exponents.

1. Introduction:

Shadow price is the unit change in the objective function of the optimal solution of an optimization problem. The shadow price is equivalent to the Lagrange multiplier at the optimal solution in the nonlinear scenario. It is also referred to as the dual variable considering the Lagrangian is the dual problem of the original optimization problem. The gradient of the objective function is a linear combination of the constraint function gradients with the weights equal to the Lagrange multipliers. Investigations on various linear optimization problems can be formulated as dynamical systems [4]. Stability analysis, Lyapunov exponents and bifurcation patterns of the resulting dynamical systems can be studied in a localized manner [2]. There is a relation between the global optimum value of the optimization problem to the local stability analysis of the corresponding dynamical system. The bifurcation properties and Lyapunov exponents of the corresponding dynamical system can be studied. The aim is to compare these invariant parameters of the dynamical systems to the shadow prices of the optimization problem. The motivation for this is the fact that to calculate a Lyapunov exponent, each dynamical variable is given a small variation and the corresponding hypercube is allowed to evolve in time [1]. Let us start by defining an optimization problem as

$$\max\{f(x, y): ax + by = c\}$$

Then the Lagrangian function is given by (in the two variable case)

$$L(x, y, \lambda) = f(x, y) + \lambda(c - ax - by)$$

(with obvious generalization to higher dimensions) and by solving this function for its saddle point we obtain the shadow prices and the maximal utility, x^*, y^*, λ^* , given by the following formula:

$$\lambda^* = \frac{\frac{\partial f(x^*, y^*)}{\partial x}}{a} = \frac{\frac{\partial f(x^*, y^*)}{\partial y}}{b}$$

On the other hand, shadow prices are found by observing the change in the optimal solution under a similar variation on the constraint of the direct problem by relaxing the constraint or alternatively, varying the corresponding parameter of the objective function in the dual problem. The definitions for the Lyapunov exponents and shadow prices are thus related to a change due to a variation. The former is a familiar element of the theory of dynamical systems. The route to chaos leads to Lyapunov exponents and this work introduces a new point of view for shadow prices as chaos search in dynamical systems [3]. Under the assumption that f be differentiable and $y_0 \neq 0$ the variational equation is:

$$y_{t+1} = \frac{df(x_t)}{dx} y_t$$

Then the Lyapunov exponent is defined to be

$$\lambda(x_0, y_0) = \lim_{n \rightarrow \infty} \frac{\ln \left| \frac{y_n}{y_0} \right|}{n}$$

A negative Lyapunov exponent indicates a stable equilibrium point and a positive Lyapunov exponent indicates chaos. So Lyapunov exponents are studied numerically to see if the given system shows chaos for certain parameter values. It has been proven that discrete-time dynamical systems are used in optimization algorithms. We also know that a discrete-time dynamical system can be transformed into a continuous dynamical system, i.e. system of differential equations by Euler's method. Both proofs depend on Lyapunov stability theory.

2. Optimization problem and corresponding dynamical system

Theorem 2.1: For the optimization problem

$$\begin{aligned} \max f(x, y) &= x^k + y^k \\ \text{with respect to } g(x, y) &= 1 - x - y \end{aligned}$$

the extremum values are $(x^*, y^*) = (\frac{1}{2}, \frac{1}{2})$ and the general term of each Lagrange multiplier is $\lambda^* = -\frac{k}{2^{k-1}}$.

Proof:

$$\nabla f = \{kx^{k-1}, ky^{k-1}\}$$

$$\nabla g = \{-1, -1\}$$

$$k \begin{bmatrix} x^{k-1} \\ y^{k-1} \end{bmatrix} = \lambda^* \begin{bmatrix} -1 \\ -1 \end{bmatrix}$$

$$\lambda^* = -k \begin{bmatrix} x^{k-1} \\ y^{k-1} \end{bmatrix}$$

$$x^{k-1} = \frac{1}{2^{k-1}}$$

$$\lambda^* = -\frac{k}{2^{k-1}}$$

3. Bifurcation analysis:

The optimization problem discussed in the previous section can be considered as the corresponding dynamical system according to the Euler scheme:

$$\dot{x} = x^k + y^k - x$$

$$\dot{y} = 1 - ax - by - y$$

Investigating the bifurcation analysis of this system around the trivial equilibrium point, two different bifurcation patterns are achieved according to the value of k being odd or even. The first case where k is even ($k=2,4,\dots$) and a is chosen as the bifurcation indicates a limit point (LP) and a Bogdanov-Takens (BT) bifurcation point as given in Figure 2.1. When b is varied another case where a subcritical Hopf bifurcation point and a transcritical bifurcation point are observed as given in Figure 2.2. The second case where k is odd ($k=1,3,\dots$) and a is chosen as the bifurcation indicates two limit point (LP), a Bogdanov-Takens (BT) and a cusp (CP) bifurcation points as given in Figure 2.3. When b is varied another case where a subcritical Hopf bifurcation point and a transcritical bifurcation point are observed as given in Figure 2.4.

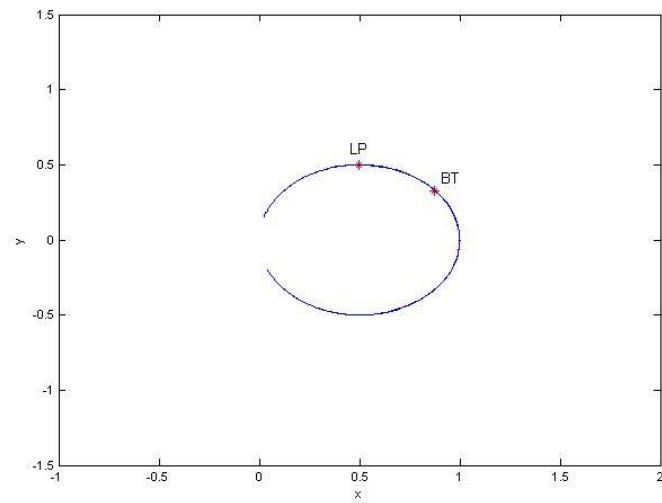


Figure 2.1. For even k ($k=2,4,\dots$) and arbitrary a

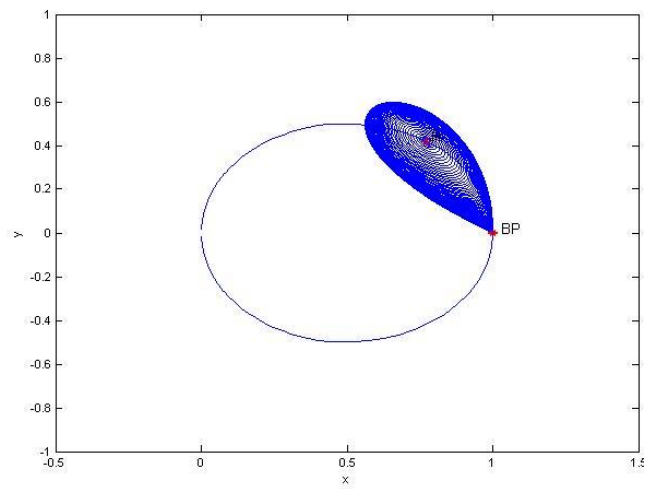


Figure 2.2. For even k ($k=2,4,\dots$) and arbitrary b

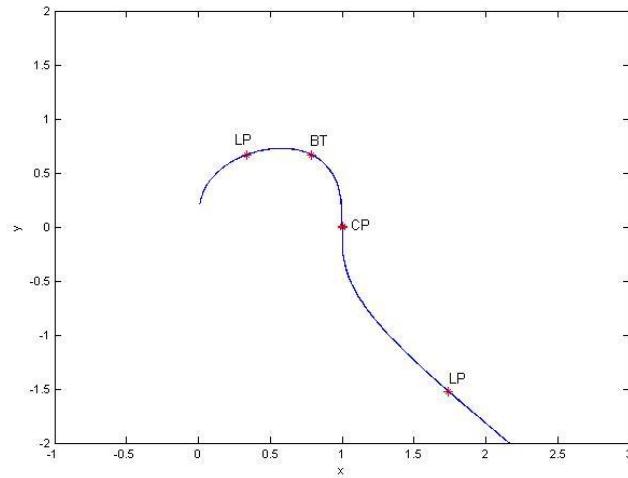


Figure 2.3. For odd k ($k=3,5,\dots$) and arbitrary a

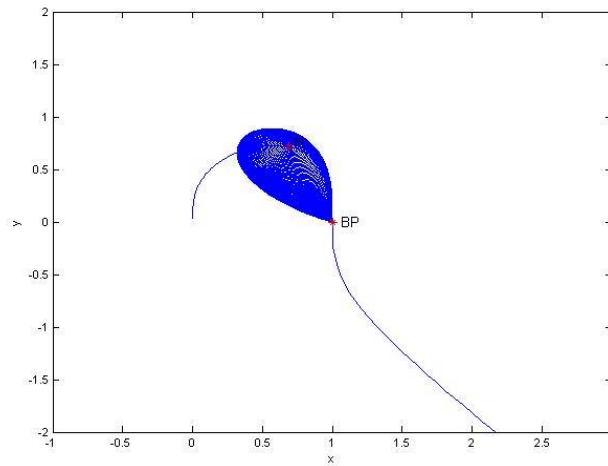


Figure 2.4. For odd k ($k=3,5,\dots$) and arbitrary b

4. Conclusion

The parameter b in our model indicates subcritical Hopf bifurcation for both even and odd cases of k . Bogdanov-Takens bifurcation is observed in all of the cases. Cusp bifurcation is observed for odd values of k . The higher nonlinearity for x and y does not affect the bifurcation phenomena. There are two different bifurcation patterns for odd and even values of k . Real values are taken into consideration in order to study real world situations.

References

1. A. Wolf, J.B. Swift, H.L. Swinney, J.A. Vastano. Determining Lyapunov exponents from a time series, *Physica D*, 16, 285–317, 1985.
2. F. Verhulst. *Nonlinear Differential Equations and Dynamical Systems*. Second Edition Springer, 1939.
3. M. Sano and Y. Sawada. Measurement of the Lyapunov Spectrum from a Chaotic Time Series. *Physical Review Letters*, 55, 1082-1085, 1985.
4. U. Helmke. Balanced realizations for linear systems: a variational approach. *SIAM J. Control Optim.*, 31, 1–15, 1993.

Cryptography with Chaos

George Makris , Ioannis Antoniou

Mathematics Department, Aristotle University, 54124, Thessaloniki, Greece

E-mail: geormak@hotmail.com

Mathematics Department, Aristotle University, 54124, Thessaloniki, Greece

E-mail: iantonio@math.auth.gr

Abstract: We implement Cryptography with Chaos following and extending the original program of Shannon with 3 selected Torus Automorphisms, namely the Baker Map, the Horseshoe Map and the Cat Map. The corresponding algorithms and the software (chaos_cryptography) were developed and applied to the encryption of picture as well as text in real time. The maps and algorithms may be combined as desired, creating keys as complicated as desired. Decryption requires the reverse application of the algorithms.

Keywords: Cryptography, Chaos, image encryption, text encryption, Cryptography with Chaos.

1. Chaotic Maps in Cryptography

Chaotic maps are simple unstable dynamical systems with high sensitivity to initial conditions [Devaney 1992]. Small deviations in the initial conditions (due to approximations or numerical calculations) lead to large deviations of the corresponding orbits, rendering the long-term forecast for the chaotic systems intractable [Lighthill 1986]. This deterministic in principle, but not determinable in practice dynamical behavior is a local mechanism for entropy production. In fact Chaotic systems are distinguished as Entropy producing deterministic systems. In practice the required information for predictions after a (small) number of steps, called horizon of predictability, exceeds the available memory and the computation time grows superexponentially. [Prigogine 1980, Strogatz 1994, Katok, ea 1995, Lasota, ea 1994, Meyers 2009].

Shannon in his classic 1949 first mathematical paper on Cryptography proposed chaotic maps as models - mechanisms for symmetric key encryption, before the development of Chaos Theory. This remarkable intuition was based on the use of the Baker's map by Hopf in 1934 as a simple deterministic mixing model with statistical regularity. The Baker's Map is defined below and the mixing character is presented in figure 1:

$$B : [0,1) \times [0,1) \rightarrow [0,1) \times [0,1) : \begin{pmatrix} x \\ y \end{pmatrix} \rightarrow \begin{cases} \begin{pmatrix} 2x \\ \frac{y}{2} \end{pmatrix} & x \in \left[0, \frac{1}{2}\right) \\ \begin{pmatrix} 2x-1 \\ \frac{y+1}{2} \end{pmatrix} & x \in \left[\frac{1}{2}, 1\right) \end{cases}$$



The reverse transformation:

$$B^{-1}: [0,1) \times [0,1) \rightarrow [0,1) \times [0,1): \begin{pmatrix} x \\ y \end{pmatrix} \rightarrow \begin{pmatrix} \frac{1}{2} & 0 \\ 0 & 2 \end{pmatrix} \begin{pmatrix} x \\ y \end{pmatrix} \bmod 1 = \begin{cases} \begin{pmatrix} \frac{x}{2} \\ 2y \end{pmatrix} & y \in \left[0, \frac{1}{2}\right) \\ \begin{pmatrix} \frac{x+1}{2} \\ 2y-1 \end{pmatrix} & y \in \left[\frac{1}{2}, 1\right) \end{cases}$$

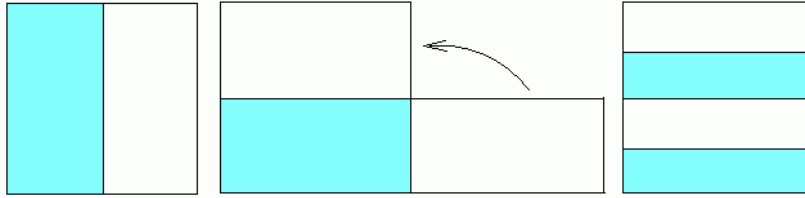


Fig. 1: Baker Map

The Entropy production theory of Chaotic maps was developed later by Kolmogorov and his group [Arnold, Avez 1968, Katok, et al 1995, Lasota, et al 1994]. Baker's map is the simplest example of chaotic automorphisms with constant Entropy production equal to one bit at every step and has served as toy model for understanding the problem of Irreversibility in Statistical Mechanics [Prigogine 1980]. Shannon observed that using chaotic maps, encryption is achieved via successive mixing of the initial information which is "spread" all over the available state space. In this way it is becoming exponentially hard to recover the initial message without knowing the reverse transformation.

A variation of the transformation of Baker Map is the Horseshoe Map [Smale 1967, Smale 1998], with the same Entropy production defined below and the mixing character presented in figure 2:

$H: [0,1) \times [0,1) \rightarrow [0,1) \times [0,1):$

$$H(x, y) = \begin{cases} \begin{pmatrix} 2x, \frac{y}{2} \end{pmatrix} & x \in \left[0, \frac{1}{2}\right) \\ \begin{pmatrix} 2-2x, \frac{2-y}{2} \end{pmatrix} & x \in \left[\frac{1}{2}, 1\right) \end{cases}$$

The reverse transformation:

$$H^{-1}(x, y) = \begin{cases} \begin{pmatrix} \frac{x}{2}, 2y \end{pmatrix} & y \in \left[0, \frac{1}{2}\right) \\ \begin{pmatrix} \frac{2-x}{2}, 2(1-y) \end{pmatrix} & y \in \left[\frac{1}{2}, 1\right) \end{cases}$$

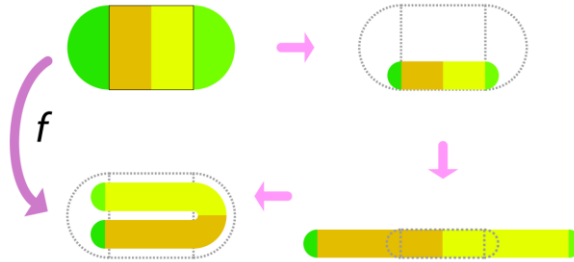


Fig. 2: HorseShoe Map (http://en.wikipedia.org/wiki/Horseshoe_map)

Both Baker's Map and the Horseshoe Map belong to the general class of torus automorphisms. The well known Cat Map introduced by Arnold in 1968 which is a torus automorphism a much stronger mix than two previous ones. The Cat Map is defined below and the mixing character is presented in figure 3:

$$\begin{bmatrix} x' \\ y' \end{bmatrix} = A \begin{bmatrix} x \\ y \end{bmatrix} \pmod{N} = \begin{bmatrix} 1 & p \\ q & pq+1 \end{bmatrix} \begin{bmatrix} x \\ y \end{bmatrix} \pmod{N}$$

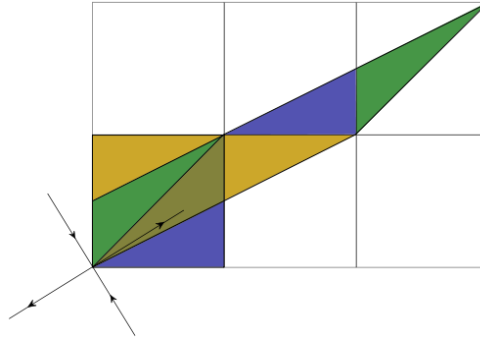


Fig. 3: Cat Map (http://en.wikipedia.org/wiki/Arnold's_cat_map)

The numerical analysis of the Cat Map shows interesting periodicity in the state space discretization [Vivaldi 1989]. Although the Cat Map and the torus automorphisms admit analytical solution, computability does not increase significantly. [Akritas, ea 2001]. Statistical estimates for the transformation of Baker Map and the Cat Map are possible through the spectral analysis [Antoniou and Tasaki 1992, Antoniou, ea 1997, Antoniou and Tasaki 1993].

From Pesin's 1977 Formula, the entropy of the Cat Map

is: $\log_2 \frac{3+\sqrt{5}}{2} \approx 1,39$, ie. larger than the entropy of the Baker's map.

Following Shannon's idea, encryption is achieved by entropy producing (chaotic) maps like the torus automorphisms, via successive mixing of the initial information which is "spread" all over the available state space. In this way it is becoming exponentially hard to recover the initial message without knowing the

reverse transformation. Most applications of Chaos cryptography with 2-dimensional maps deal with image encryption [Guan D. et al., 2005, Xiao G. et al., 2009]. We also found results on text encryption [Kocarev, et al., 2003, Kocarev, et al., 2004, Kocarev and Lian, 2011, Li, 2003]. We shall show how encryption of texts can also be achieved with chaotic maps.

2. Text Encryption and Decryption by Torus Automorphisms

The text Cryptography by Torus Automorphisms involves 3 steps:

Step 1: Place the text in a 2-dimensional table so that each array element is a character.

Step 2: Apply the selected transformations on the table for a number of steps specified by the key.

Step 3: convert the modified table from step 2 in the text.

The decryption process is equally simple for anyone who holds the key. Simply follow the steps backwards and use inverse transformations to the same number of steps.

We propose 2 algorithms for the implementation of the text cryptography:

Algorithm 1:

Step 1: Count all characters of text including line breaks ($=N_1$)

Step 2: If N_1 is not a perfect square of an integer, then find the smallest integer $M > N_1$ so that M is a perfect square. If the N_1 is a perfect square integer number then set $M=N_1$.

Step 3: Set $N = \sqrt{M}$

Step 4: Create a character table ($N \times N$) and place the characters of the text inside the table, putting also the special characters newline (enter) in a position in the table.

Step 5: If there are empty cells at the end of the table place the spaces in these (cells).

So we create a $N \times N$ table of characters with the properties:

- 1) The number of rows and columns of the table depends on the length of the text only.
- 2) The number of lines of characters changes during the encryption because all the special characters like “enter” are involved in encryption.

Example:

Cryptography with chaos
George Makris, Ioannis Antoniou
Thessaloniki 54124
Greece.

The above text has 82 characters. We need a 10x10 table to fit the text in table (100 is the minimal encoding length)

[illegible]

Algorithm 2:

Step 1: Count the number of lines (NL) of the text.

Step 2: Count the number of letters of each line.

Step 3: Find the $M1 = \max \{ \text{the number of letters of each line} \}$.

Step 4: Set $N = \max \{NL, M1\}$

Step 5: Create a character table (N x N)

Step 6: Place each character in text in the table so that it corresponds to each line of text in the corresponding row of the table. Put the special character space (' ') in all the blank cells.

So we create a NxN table of characters with the properties:

- 1) The number of rows and columns of the table defined by the structure and the length of the text.
- 2) The number of lines of characters does not change in encryption because gaps were placed on each line so that all lines have the same number of characters.

For the same example we have:

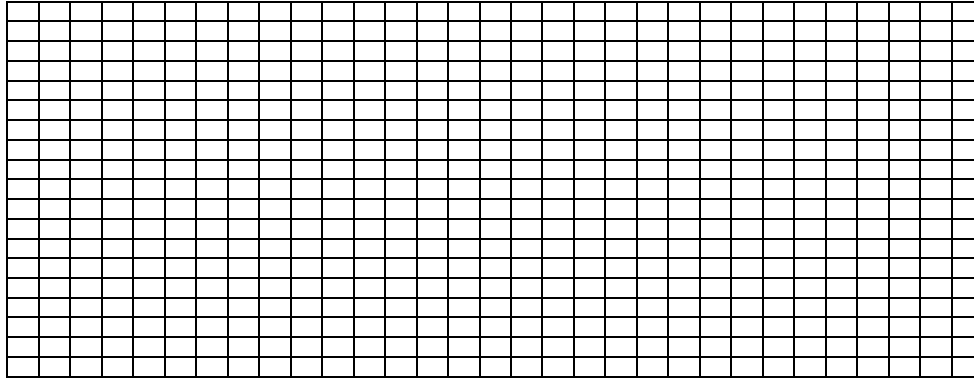
Cryptography with chaos → 23 characters

George Makris, Ioannis Antoniou → 31 characters

Thessaloniki 54124 → 18 characters

Greece. → 07 characters

Lines NL = 4
$$M1 = \max\{23, 31, 18, 07\} = 31$$
$$N = \max\{4, 31\} = 31$$
[illegible]



Examples of text and image encryption are presented in the appendices

3. Software Development for the implementation of "Cryptography with Chaos"

The software for the algorithms was developed with Java, as this language is independent of the operating system and platform. Moreover the Java programs run on Windows, Linux, Unix and Macintosh, mobile phones, Ipads, Playstations and other game consoles without any modification like compilation or changing the source code for each different operating system.

The software developed (chaos_cryptography) has a graphical user interface and is very simple and user friendly (figure 4).

The user may encrypt / decrypt images and texts. The user may use any of the above chaotic maps with one or the other algorithm or any combination for more difficult deciphering.

Window dialogs alert the user in case of any errors in the procedure.

The developed libraries (classes) can be used by any other software and application



Fig. 4: chaos_cryptography application (main window)

4. Concluding Remarks

Shannon Cryptography indices for chaos cryptography are summarized in the table below.

Shannon Cryptography indices	Cryptography with Chaos
Required degree of cryptographic security	High
Key Length	Small The key is the selected transformations and the number of iterations that apply each transformation.
Practical implementation of the encryption / decryption	Depends on the size of the text. Generally, permutation is a faster method than the replacement.
Growth of the encrypted text	No growth in the case of images. Small growth in the case of texts, due to “spaces” only
Error Propagation	In case of images, pixel errors propagate, are preserved in the reconstructed images without influencing the decryption. In case of text, errors may rendering text decryption practically impossible.

The key length includes the map definition, the number of iterations and the parameters of the specific map. The proposed encryption algorithms are “MonoBlock” ciphers based on permutations, however they are neither streams nor block ciphers. The Key is very small and does not depend on the size of text to be encrypted (block).

For example, the specific key for encryption algorithm (Baker, Cat, Horseshoe) has a size 4 (Table 2x2). In classical permutation algorithms to encrypt a text with N characters (MonoBlock, size of the block = N) a key size N is required which is the size of the Block.

The innovations of this work are summarized as follows:

- The application of Cryptography with Chaos to content with texts and images.
- The construction of examples of a new class on ciphers, namely the Mono-Block Ciphers as a third class beyond the Block Ciphers and the Stream Ciphers.
- The key is completely independent from the length of the block that is encrypted and it is very small compared to the key of the classic permutation algorithms which is equal to the length of the block.
- In the developed algorithms the key cannot operate if some small part of the document is lost.

Chaos Cryptography has only the disadvantage of all systems of symmetric cryptography, namely the safe transport of the key.

In this paper three of the most famous chaotic maps were investigated. The proposed algorithms can be adapted to other chaotic maps.

References







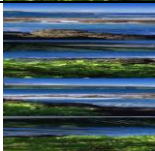
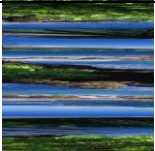
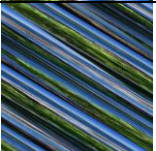
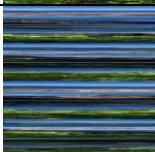
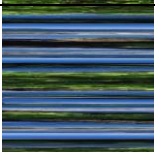
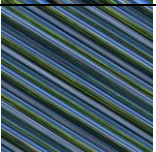

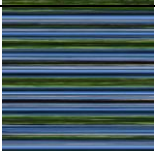
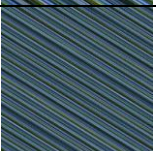
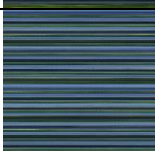
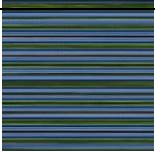
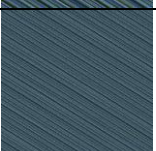
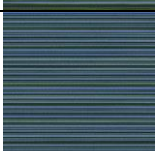
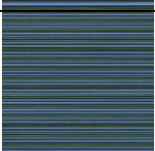
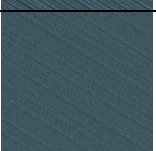
1. Akritas P., Antoniou I., Pronko G. 2001, "On the Torus Automorphisms: Analytic Solution, Computability and Quantization", *Chaos, Solitons and Fractals* 12, 2805-2814
2. Antoniou I., Tasaki S. 1992, Generalized spectral decomposition of the β -adic baker's transformation and intrinsic irreversibility, *Physica A* 190, 303-329.
3. Antoniou I., Bi Qiao, Suchanecki Z. 1997, "Generalized Spectral Decomposition and Intrinsic Irreversibility of the Arnold Cat Map", *Chaos Solitons and Fractals* 8, 77 – 90
4. Antoniou I., Tasaki S. 1993, Generalized spectral decomposition of mixing dynamical systems, *Int. J. Quantum Chemistry* 46, 425-474.
5. Arnold, V. I. and Avez, A. 1968, *Ergodic Problems of Classical Mechanics* Benjamin, New York
6. R. Devaney 1992, *A First Course in Chaotic Dynamical Systems*, Perseus Books.
7. Guan Z. H., Huang F., and Guan W. 2005. Chaos-based image encryption algorithm. *Physics Letters A*, Vol. 346, Issues 1-3, pp 153-157.
8. Hopf E. (1934), On Causality, Statistics and Probability, *J. Math. and Phys.* 13, 51-102.
9. Katok A., Hasselblatt B. 1995, *Introduction to the Modern Theory of Dynamical Systems*, Cambridge University Press, Cambridge, UK
10. Kocarev L., Sterjev M., Amato P., RSA ENCRYPTION ALGORITHM BASED ON TORUS AUTOMORPHISMS, *IEEE, ISCAS (2004)*, IV 577-580.
11. Kocarev L., Tasev Z., and Makraduli J., "Public-Key Encryption and Digital-Signature Schemes Using Chaotic Maps", 16th European Conference on Circuits Theory and Design, September 1 – September 4, 2003, Krakow, Poland, ECCTD 2003.
12. Kocarev, L., Lian, S., *Chaos-Based Cryptography. Theory, Algorithms and Applications*, *Studies in Computational Intelligence*, Vol. 354, (2011), ISBN 978-3-642-20542-2, Berlin.
13. Lasota A. and Mackey M. 1994, *Chaos, Fractals, and Noise*, Springer-Verlag New York.
14. Li, S., *Analyses and New Designs of Digital Chaotic Ciphers*. Ph.D. thesis, School of Electronic and Information Engineering, Xi'an Jiaotong University, Xi'an, China, 2003
15. Lighthill J. 1986, The recently recognized failure of predictability in Newtonian dynamics, *Proc. Roy. Soc. London A* 407, 35-50
16. Meyers R. A., ed. 2009 *Encyclopedia of Complexity and Systems Science*, Springer, New York.
17. Pesin Ya. B. 1977, Characteristic Lyapunov exponents and smooth ergodic theory, *Russ. Math. Surv.* 32:4, 55-112
18. Prigogine I. 1980, *From Being to Becoming*, Freeman, New York.
19. Shannon C., Weaver W. 1949, *The Mathematical Theory of Communication*, University of Illinois Press, Urbana, Ill.
20. Shannon, C. 1949, *Communication Theory of Secrecy Systems*. *Bell System Technical Journal*, Vol. 28, Issue 4, pp 656–715.
21. Smale S. 1967, "Differentiable dynamical systems". *Bulletin of the American Mathematical Society* 73: 747–817.
22. Smale S. 1998, Finding a horseshoe on the beaches of Rio, *Mathematical Intelligencer* 20, 39-44
23. Strogatz S. 1994, *Non-Linear Dynamics and Chaos*, Perseus, Massachusetts

24. Vivaldi F. 1987, The arithmetic of Chaos, in Chaos, Noise and Fractals, volume 3 of Malvern Phys. Ser., pages 187–199. Hilger, Bristol.
25. Xiao, D., Liao, X., Wei, P. 2009. Analysis and improvement of a chaos-based image encryption algorithm. Chaos, Solitons & Fractals, Vol. 40, Issue 5, pp 2191-2199.

Appendix A : Text encryption

Iterations	Baker Map	Horseshoe Map	Cat Map
t=0	Cryptography with chaos George Makris, Ioannis Antoniou Thessaloniki 54124 Greece.	Cryptography with chaos George Makris, Ioannis Antoniou Thessaloniki 54124 Greece.	Cryptography with chaos George Makris, Ioannis Antoniou Thessaloniki 54124 Greece.
t=1	otghr acpheiotsr,g eIs TAhnetsiGkrie e5c Chryy pwtia oMsa kGrooanninoi us4a1l2o4n e .	c5e eirkGistenhA T sle g,rsioiehpca rhgtoChryy pwtia oMsa kGrooanninoi us4a1l2o4n e .	C 4n ,ghehr iTA nIayy Gkhiet o p r e soMswt o e5oaa iGtg csnnknrehr 4ailoio a e1.2oussrcp
t=2	,agc pehlhen eet5sc p w t iai nkoGiru2 o 4 n oetigohsrrsi G kTrAi C h r y yao ooaMnsnse4 a.1 l	n 4 o 2uriGokn iaiottwgph resi o sTrAi G k r i c 5 e esltee ngh,hCphcray yao ooaMnsnse4 a.1 l	C2ih os k he oircau trnh uo san ilr4s a4ni ea ns r akoety y ceiG so i,pInt geo Tg lroe 5MpGAh.
t=3	epte5hsIcwo Gti riu onh s r rkrT ryA iya.M1n sln h,eang ce a i pn k2o eot i4gs iC Gh asoe 4o oa	nls n1M.ay, hyganr e i re Arr Thsp ga2i on k4 u r inG oieostit woi cG 5k shlCtpehecas oe 4o oa	Ceoieoass ah2 ,ie n tei5 pGt ysnr hMT1gn a no poG t 4 hi rsAl yrniiIuc hrs a roak.goe cke4 w o

Appendix B : Image Encryption

Iterations	Baker Map	Horseshoe Map	Cat Map
t=0			
t=1			
t=2			
t=3			
t=4			
t=5			
t=6			

Chaos in Modified CFOA-Based Inductorless Sinusoidal Oscillators Using a Diode

Buncha Munmuangsaen and Banlue Srisuchinwong

Sirindhorn International Institute of Technology, Thammasat University
Pathum-Thani 12000, Thailand
E-mail: banlue@siit.tu.ac.th

Abstract: Two modified inductorless sinusoidal oscillators are presented as two chaotic oscillators. The active component employs a current-feedback operational amplifier (CFOA) whereas the nonlinear component employs a simple diode. Numerical and PSpice simulations are demonstrated in terms of chaotic attractors. A bifurcation diagram is also included.

Keywords: Chaos, Nonlinear circuit and system, RC oscillator.

1. Introduction

The design and development of autonomous chaotic oscillators over the past three decades have been increasing due to a variety of applications in, for example, spacecraft trajectory control, stabilization of the intensity of a laser beam, noise radars and sonar [1], synchronization [2, 3] and secure communications [4, 5, 6]. One of the best known chaotic circuits is Chua's circuit [7] as well as its variants [8, 9], using a Chua's diode. However, an active nonlinear resistor such as the Chua's diode is not recommended by [10] because it does not follow the design rules of [10]. Instead, a passive nonlinear component for chaos has been suggested using either a diode or a junction field effect transistor (JFET) [10].

A current-feedback operational amplifier (CFOA) is currently recognized as a versatile alternative to the traditional op amp for its excellent performance in high-speed and high slew-rates analog signal processing, and therefore does not suffer from the finite gain bandwidth product typically encountered in the conventional voltage op amps [11]. A chaotic oscillator has been designed using a modified CFOA-based sinusoidal oscillator with two capacitors and an inductor for a third-order chaotic system [11]. Such a chaotic oscillator has subsequently been further investigated by [12] using three capacitors. The nonlinear device of both chaotic oscillators has exploited a two-terminal nonlinear resistor formed by a JFET (J2N4338). However, chaos has not successfully found in [12] using a single diode as a nonlinear component.

In this paper, chaos in two modified CFOA-based inductorless sinusoidal oscillators is presented. The active element employs the CFOA whereas the

nonlinear component employs a single diode. Chaos can be found by replacing a JFET resistor of [12] with a sub-circuit consisting of a diode and a resistor.

2. Circuit Implementation

Figures 1(a) and 1(b) show two proposed chaotic oscillators using a single diode as a nonlinear device. Both circuits are modified CFOA-based inductorless sinusoidal oscillators which almost resemble the existing circuits reported in [12], except that the JFET nonlinearity of [12] is replaced with a new sub-circuit consisting of a diode D_1 and a resistor R_3 . The latter is connected to a negative DC supply.

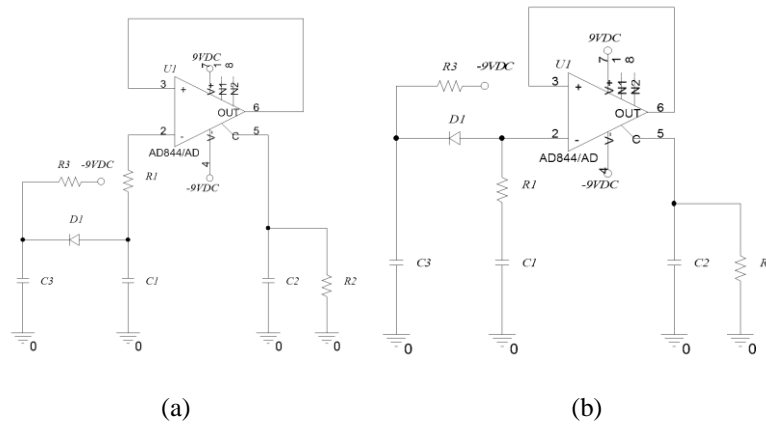


Fig. 1 Modified CFOA-based inductorless sinusoidal oscillators using a diode for : (a) the first chaotic oscillator, (b) the second chaotic oscillator.

The proposed chaotic oscillator shown in Figure 1(a) is described by a set of differential equations as follows :

$$\begin{aligned} C_1 \dot{V}_{C1} &= \left(\frac{V_{C2} - V_{C1}}{R_1} \right) - I_D \\ C_2 \dot{V}_{C2} &= \left(\frac{V_{C2} - V_{C1}}{R_1} \right) - \frac{V_{C2}}{R_2} \\ C_3 \dot{V}_{C3} &= I_D - \left(\frac{V_{C3} + 9}{R_3} \right) \end{aligned} \quad (1)$$

where the overdot denotes a time (t) derivative. The voltages across capacitors C_1 , C_2 , and C_3 are V_{C1} , V_{C2} , and V_{C3} , respectively. A diode current $I_D = I_S \{ \exp[(V_{C1} - V_{C3})/nV_T] - 1 \}$ where I_S is the reverse saturation current, n is the nonideality factor, and V_T is the thermal voltage of 25.85 mV at room temperature (300K). The proposed chaotic oscillator shown in Figure 1(b) is described by another set of differential equations as follows:

$$\begin{aligned}
 C_1 \dot{V}_{C1} &= \frac{V_{C2} - V_{C1}}{R_1} \\
 C_2 \dot{V}_{C2} &= \left(\frac{V_{C2} - V_{C1}}{R_1} \right) - \left(\frac{V_{C2}}{R_2} \right) + I_D \\
 C_3 \dot{V}_{C3} &= I_D - \left(\frac{V_{C3} + 9}{R_3} \right)
 \end{aligned} \tag{2}$$

where the diode current $I_D = I_S \{ \exp[(V_{C2} - V_{C3})/nV_T] - 1 \}$

3. Simulation Results

The CFOA can be implemented using the commercially available AD844. The diode D_1 is 1N4001 using PSpice parameters $I_S = 14.11 \times 10^{-9}$ A and $n = 1.984$. The junction capacitance of 1N4001 is typically 15 pF and, for simplicity, may be neglected compared to the much larger values of C_1 , C_2 and C_3 . For a PSpice simulation, Figure 2(a) shows a circuit diagram of (i) a diode circuit (D_4 , R_2), (ii) a nonlinear JFET resistor (J_1 , R_4), and (iii) a sub-circuit consisting of a diode and resistors (D_3 , R_1 , R_3). Figure 2(b) shows a comparison of the three simulation results of current-voltage characteristics in (i), (ii) and (iii) where the currents on the vertical axis are through R_2 , R_4 and R_1 , respectively, and the voltage on the horizontal axis is V_S , which is swept linearly from -2V to +1V with an increment of 0.01 V. It should be noted that the current in (i) is always positive whereas the current in (ii) can be either positive or negative. This may probably be the reason why the authors in [12] could not find chaos in their proposed oscillators using only a diode in (i). With a new sub-circuit in (iii), the current in (iii) can be either positive or negative, as shown in Figure 2, and chaos can be quickly found without changing the connections of other components.

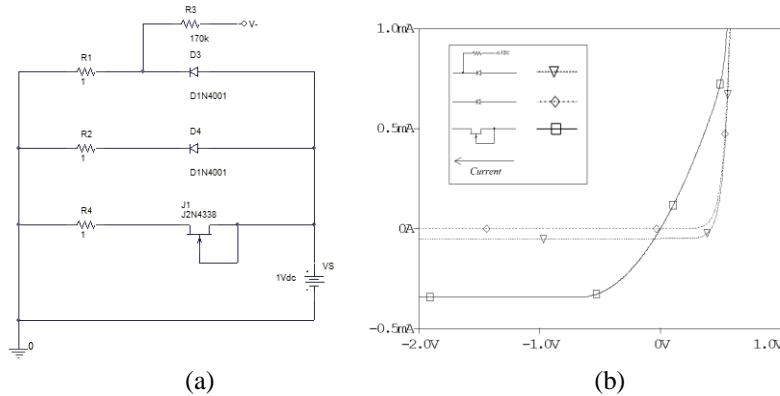


Fig. 2 (a) A circuit diagram of three circuits using (i) a diode circuit (D_4 , R_2), (ii) a nonlinear JFET resistor (J_1 , R_4), and (iii) a sub-circuit consisting of a diode and resistors (D_3 , R_1 , R_3), (b) A comparison of three simulation results.

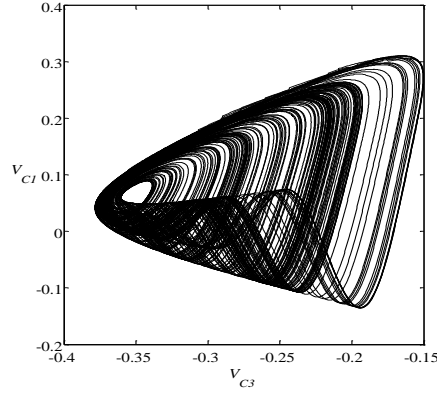


Fig. 3. A numerical result of a chaotic attractor projected onto V_{C3} – V_{C1} plane of equation (1).

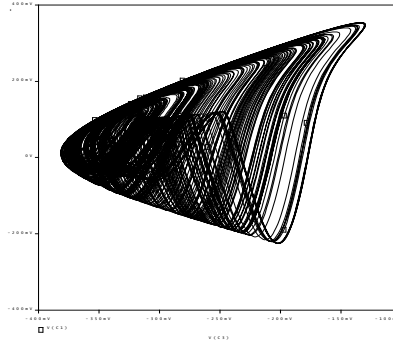


Fig. 4. A PSpice simulation of a chaotic attractor projected onto V_{C3} – V_{C1} plane of the oscillator shown in Figure 1(a).

Figure 3 shows a numerical result of a chaotic attractor projected onto a V_{C3} – V_{C1} plane of equation (1) using a fourth-order Runge-Kutta integrator with a fixed step size of $0.1\mu\text{s}$. The same values of components reported in [12] are used except R_3 , i.e. $C_1 = C_2 = 10\text{ nF}$, $C_3 = 18\text{ nF}$, $R_1 = 220\ \Omega$, $R_2 = 1.5\text{ k}\Omega$, and $R_3 = 170\text{ k}\Omega$. Figure 4 shows a PSpice simulation of a chaotic attractor projected onto V_{C3} – V_{C1} plane of the oscillator shown in Figure 1(a) with the same values of components reported in [12] except $R_3 = 180\text{ k}\Omega$. As shown in Figure 4, the PSpice simulation runs up to 30 ms with a fixed step size of $0.5\ \mu\text{s}$. The results in the first 20 % are discarded to ensure that the solution is on the attractor. Initial conditions are $(V_{C1}, V_{C2}, V_{C3})_{t=0} = (0, 0, 0)$. The numerical and PSpice results are in a similar manner.

It can be seen from Figures 1(a) and 1(b) that R_3 is connected in series with the diode D_1 . This enables R_3 to control the current of D_1 in DC operation (by opening C_1 , C_2 , and C_3). Therefore R_3 can be exploited as a tunable bifurcation parameter. As an example, Figure 5 depicts a bifurcation diagram of the peak of V_{C3} (V_{C3-max}) of Figure 1(a) versus R_3 varied from 140 to 220 k Ω . A period-doubling route to chaos is evident. There are various periodic windows immersed in chaos.

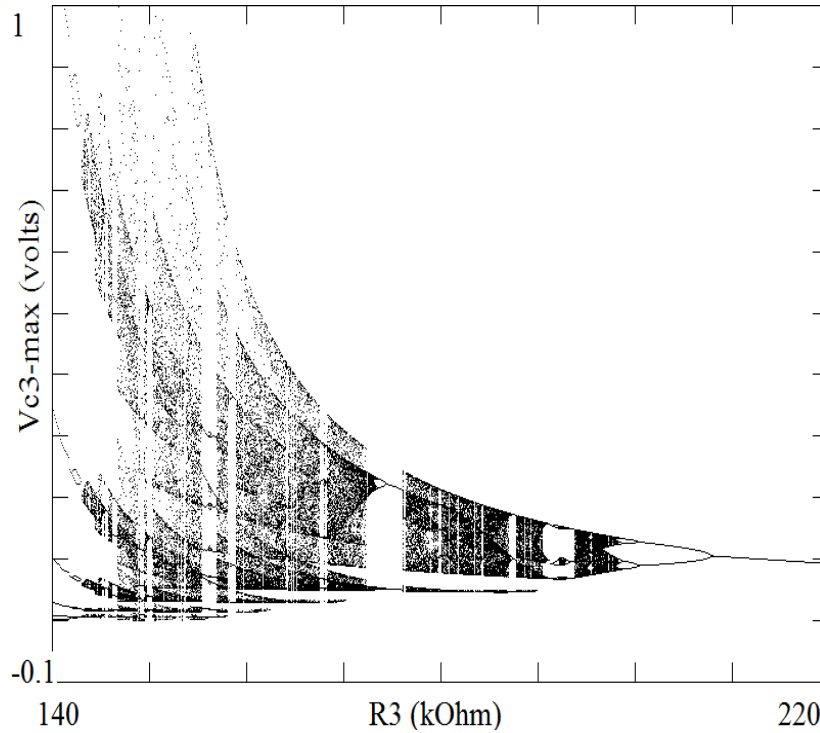


Fig. 5. A bifurcation diagram of the peak of V_{C3} of Figure 1(a).

Figure 6 shows a numerical result of a chaotic attractor projected onto a $V_{C3}-V_{C2}$ plane of equation (2) using a fourth-order Runge-Kutta integrator with a fixed step size of 0.1 μ s, $C_1 = 10$ nF, $C_2 = 11$ nF, $C_3 = 5$ nF, $R_1 = 220$ Ω , $R_2 = 2.7$ k Ω , and $R_3 = 220$ k Ω . Figure 7 illustrates a PSpice simulation of a chaotic attractor projected onto $V_{C3}-V_{C2}$ plane of the oscillator shown in Figure 1(b) with the same values of components used in Figure 6. The PSpice simulation runs up to 20 ms with a fixed step size of 0.1 μ s. The results in the first 20 % are discarded to ensure that the solution is on the attractor. Initial conditions are $(V_{C1}, V_{C2}, V_{C3})_{t=0} = (0, 0, 0)$.

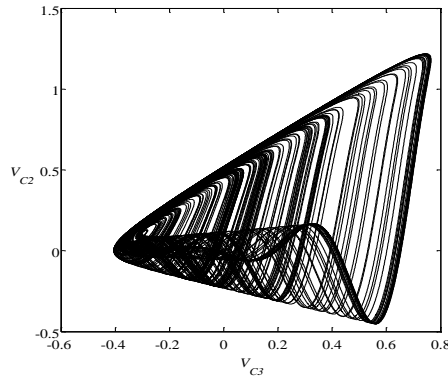


Fig. 6. A numerical result of a chaotic attractor projected onto V_{C3} – V_{C2} plane of equation (2).

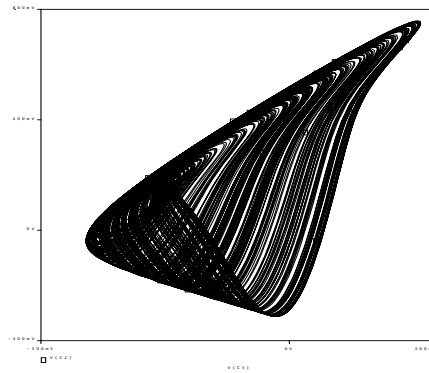


Fig. 7. A PSpice simulation of a chaotic attractor projected onto V_{C3} – V_{C2} plane of the oscillator shown in Figure 1(b).

4. Conclusions

Two chaotic oscillators have been presented through the use of two modified CFOA-based inductorless sinusoidal oscillators. A CFOA has been exploited as the active component whereas a single diode has been exploited as the nonlinear component. Numerical and PSpice simulations have been demonstrated with chaotic attractors. A bifurcation diagram has been studied.

Acknowledgments: This work was supported by telecommunications research and industrial development institute (TRIDI), NBTC, Thailand (grant TARG 2553/002), and the national research university project of Thailand, office of higher education commission.

References

1. T. Kiliyas, K. Kelber, A. Mogel, and W. Schwarz. Electronic chaos generators—design and applications. *Int J Electron* 79: 737-753, 1995.
2. T. L. Carroll and L. M. Pecora. Synchronizing chaotic circuits. *IEEE Trans Circuits Syst* 38: 453-456, 1991.
3. B. Munmuangsaen and B. Srisuchinwong. A new Lorenz-like chaotic attractor and its synchronization. *CCDC2009*: 1508-1512, 2009.
4. K. M. Cuomo, A. V. Oppenheim and S. H. Strogatz. Synchronization of Lorenz-based chaotic circuits with applications to communications. *IEEE Trans Circuit Syst* 40: 626-633, 1993.
5. L. Kocarev, K. S. Halle, K. Eckert and L. O. Chua. Experimental demonstration of secure communications via chaotic synchronization. *Int J Bifurcat Chaos* 2: 709-713, 1992.
6. B. Srisuchinwong, B. Munmuangsaen. A highly chaotic attractor for a dual-channel single-attractor, private communication system. In: C. H. Skiadas, I. Dimotikalis and C. Skiadas, Eds, *Chaos Theory: Modeling, Simulation and Applications: Selected Papers from the CHAOS2010 International Conference*. World Scientific, Singapore, pp. 399-405, 2011.
7. L. Fortuna, M. Frasca, and M. G. Xibilia. Chua's *Circuit Implementations: Yesterday, Today and Tomorrow*, World Scientific, Singapore, 2009.
8. E. Bilotta and P. Pantano. *A Gallery of Chua Attractors*, World Scientific, Singapore, 2008.
9. L. O. Chua and G. Lin. Canonical realization of Chua's circuit family. *IEEE Trans Circuits Syst* 37: 885-902, 1990.
10. A. S. Elwakil and M. P. Kennedy. A semi-systematic procedure for producing chaos from sinusoidal oscillators using diode-inductor and FET-Capacitor composites. *IEEE Trans Circuits Syst* 47: 582-590, 2000.
11. A. S. Elwakil and M. P. Kennedy. Chaotic oscillator derived from sinusoidal oscillator based on the current feedback op amp. *Analog Integ Circuits Signal Proc* 24: 239-251, 2000.
12. P. Bernát and I. Baláž. RC autonomous circuit with chaotic behaviour. *Radioengineering* 11: 1-5, 2002.

